ISSN: 2224-2007
E-ISSN: 2707-7365

MIJST

MIST International Journal of Science and Technology

A Peer Reviewed Online Open Access Journal

Volume 10
December 2022

Military Institute of Science and Technology (MIST)
https://mijst.mist.ac.bd/mijst
Previously known as:
MIST Journal of Science and Technology

MIJST

MIST International Journal of Science and Technology

Volume 10

December 2022

EDITORIAL BOARD

CHIEF PATRON

Major General Md Wahid-Uz-Zaman, BSP (BAR), ndc, aowc, psc, te
Commandant
Military Institute of Science and Technology (MIST)
Dhaka, Bangladesh

PUBLICATION ADVISOR

Brigadier General Mohammad Pavel Akram, afwc, psc
Director, R&D Wing
Military Institute of Science and Technology (MIST)
Dhaka, Bangladesh

EDITOR-IN-CHIEF

Dr. Firoz Alam
Professor
School of Engineering, RMIT University
Melbourne, Australia

EXECUTIVE EDITOR

Dr. A.K.M. Nurul Amin
Professor, Industrial and Production Engineering
Military Institute of Science and Technology (MIST)
Dhaka, Bangladesh

ASSOCIATE EDITOR

Lt Col Md Altab Hossain, PhD, EME
Assoc. Professor, Nuclear Science and Engineering
Military Institute of Science and Technology (MIST)
Dhaka, Bangladesh

ASSOCIATE EDITOR

Lt Col Muhammad Nazrul Islam, PhD, Sigs
Assoc. Professor, Computer Science and Engineering
Military Institute of Science and Technology (MIST)
Dhaka, Bangladesh

EDITORIAL BOARD MEMBERS

Prof. G. M. Jahid Hasan
MIST, Bangladesh

Prof. Yuying Yan
Nottingham University, UK

Prof. Grzegorz Krolczyk
Opole University of Technology, Poland

Prof. Drazan Kozak
University of Slavonski Brod, Croatia

Assoc. Prof. Lt Col Khondaker Sakil Ahmed, PhD, PEng, CEng
MIST, Bangladesh

Prof. Sergej Hloch
Technical University of Košice, Slovakia

Prof. Mohamed H. M. Hassan
Alexandria University, Egypt

Prof. Xiaolin Wang
University of Tasmania, Australia

Prof. Md. Mahbubur Rahman
MIST, Bangladesh

Prof. Muhammad Mustafizur Rahman
Wichita State University, USA

Prof. Santanu Bandyopadhyay
Indian Institute of Technology (IIT) Bombay, India

Prof. Yan-Hui Feng
University of Science and Technology Beijing, China

Brig Gen A K M Nazrul Islam, PhD
MIST, Bangladesh

Prof. Stanislaw Legutko
Poznan University of Technology, Poland

Prof. Nakorn Tippayawong
Chiangmai University, Thailand

Prof. Katarina Monkova
Technical University of Košice, Slovakia & Tomas Bata University in Zlín, Czech Republic

Asst. Prof. Tariq Mahbub
MIST, Bangladesh

Prof. Elsadig Mahdi Ahmad Saad
Qatar University, Qatar

Prof. Himadri Chattopadhyay
Jadavpur University, India

Prof. Yingai Jin
Jilin University, China

Prof. M A Taher Ali
MIST, Bangladesh

Prof. Changheui Jang
Korea Advanced Institute of Science and Technology (KAIST), South Korea

Prof. Tanvir Farouk
University of South Carolina, USA

Prof. Abdul Hasib Chowdhury
BUET, Bangladesh

Assoc. Prof. Lt Col Osman Md Amin, PhD, Engrs
MIST, Bangladesh

Prof. Simon Watkins
RMIT University, Australia

Prof. Ataur Rahman
International Islamic University Malaysia, Malaysia

Prof. Somnath Chattopadhyaya
Indian Institute of Technology (IIT) Dhanbad, India

Assoc. Prof. Major Kazi Shamima Akter, PhD, Engrs
MIST, Bangladesh

Prof. Kaori Nagai
Nihon University, Japan

Prof. Alessandro Ruggiero
University of Salerno, Italy

Prof. Azam Ali
University of Otago, New Zealand

Assoc. Prof. Md. Sazzad Hossain
MIST, Bangladesh

Prof. Mohammed Quddus
Imperial College, UK

Prof. Anupam Basu
Indian Institute of Technology (IIT) Kharagpur, India

Prof. Muhammad H. Rashid
Florida Polytechnic University, USA

Prof. Md Enamul Hoque
MIST, Bangladesh

Prof. Naoya Umeda
Osaka University, Japan

Prof. Md Abdul Jabbar
University of Dhaka, Bangladesh

Prof. Soumyen Bandyopadhyay
Liverpool University, UK

Asst. Prof. Muammer Din Arif
MIST, Bangladesh

Prof. A.B.M. Harun-ur Rashid
BUET, Bangladesh

Prof. Shahjada Tarafder
BUET, Bangladesh

Prof. Mohammed Abdul Basith
BUET, Bangladesh

Prof. AKM Badrul Alam
MIST, Bangladesh

Prof. Stephen Butt
Memorial University of Newfoundland, Canada

Prof. Cheol-Gi Kim
Daegu Gyeongbuk Institute of Science & Technology, South Korea

Prof. Kawamura Yasumi
Yokohama National University, Japan

Assoc. Prof. Lt Col Brajalal Sinha, PhD, AEC
MIST, Bangladesh

Assoc. Prof. Lt Col Palash Kumar Sarker, PhD, Sigs
MIST, Bangladesh

Dr. Debasish Sarker
Bangladesh Army University of Science and Technology, Bangladesh

Prof. Nahrizul Adib Bin Kadri
University of Malaya, Malaysia

Lt Col Mirza Md Lutful Habib, SUP, psc, Engrs
General Staff Officer First Grade, R&D Wing, MIST, Bangladesh

Assoc. Prof. Maj Md. Manwarul Haq
MIST, Bangladesh

Md Moslem Uddin
Chief Librarian, MIST, Bangladesh

ADVISORY BOARD MEMBERS

Prof. Chanchal Roy
University of Saskatchewan, Canada

Prof. Mahmud Ashraf
Deakin University, Australia

Prof. Daili Feng
University of Science and Technology Beijing, China

Assoc. Prof. A. K. M. Najmul Islam
LUT University, Finland

Prof. Arnab Roy
Indian Institute of Technology (IIT) Kharagpur, India

Prof. Ahmad Faris Ismail
International Islamic University Malaysia (IIUM), Malaysia

Dr. Bhuiyan Shameem Mahmood Ebna Hai
Helmut Schmidt University, Germany

Prof. Md Shahidul Islam
Khulna University of Engineering & Technology, Bangladesh

Prof. Reza Nakahie Jazar
RMIT University, Australia

Prof. Md Azizur Rahman
Texas A&M University, Qatar

Prof. Bashir Ahmmad Arima
Yamagata University, Japan

Prof. Kobayashi Kensei
Yokohama National University, Japan

Prof. Mohammad Kaykobad
BUET, Bangladesh

Prof. Sunil S. Chirayath
Texas A&M University, USA

Prof. Md Hadiuzzaman
BUET, Bangladesh

Prof. Rezaul Karim Begg
Victoria University, Australia

DISCLAIMER

The analysis, opinions, and conclusions expressed or implied in this Journal are those of the authors and do not necessarily represent the views of the MIST, Bangladesh Armed Forces, or any other agencies of Bangladesh Government. Statements of fact or opinion appearing in MIJST Journal are solely those of the authors and do not imply endorsement by the editors or publisher.

ISSN: 2224-2007
E-ISSN: 2707-7365

QUERIES ON SUBMISSION

For any query on submission the author(s) should contact: MIST, Mirpur Cantonment, Dhaka-1216, Bangladesh; Tel: 88 02 8034194, FAX: 88 02 9011311, email: *mijst@mist.ac.bd*. For detailed information on submission of articles, the author(s) should refer to the Call for Papers and About MIJST at the back cover of the MIJST Journal. Authors must browse MIJST website through the journal link (*https://mijst.mist.ac.bd/mijst*) for electronic submission of their manuscripts.

PUBLISHER

Military Institute of Science and Technology (MIST), Dhaka, Bangladesh

DESIGN AND PRINTING

Research and Development Wing
Military Institute of Science and Technology (MIST)
Dhaka, Bangladesh

FOREWORD

Bismillahir Rahmanir Rahim

I am pleased to note that MIJST is going to publish the 6th issue after its rebranding as an international online journal strictly maintaining the publication schedule and quality. The journal is already indexed by many indexing bodies and I firmly believe that soon it will find its place in Scopus and WoS.

It is a pleasure to congratulate the Editorial Team for their hard work in the timely publication of the current issue. My sincere appreciations to all the reviewers for their invaluable suggestions and comments. My heartfelt thanks to all the National and International Advisory Board Members of MIJST for their constant suggestions and guidance aiming at improving the quality of MIJST.

I wish continued success of MIJST!

Major General Md Wahid-Uz-Zaman, BSP (BAR), ndc, aowc, psc, te
Commandant, MIST, Bangladesh
Chief Patron, MIJST, Bangladesh

EDITORIAL

The December 2022 issue like other previous issues of MIJST Journal has been published on schedule. It is indeed a great combined effort by all stakeholders (authors, reviewers, editors, and the production team). I am very pleased to inform that the 1st Special Issue focussing on large infrastructures development has recently been published. The Special Issues on other important topics/areas are also planned.

The preparatory work for the Journal's indexation in Scopus and the Web of Science (WoS), is going with the full swing as per the roadmap. Currently, the MIJST is indexed through Google Scholar, DOI Crossref., Microsoft Academic Search, Semantic Scholar, Publons, Creative Common, BanglaJOL, and Open Journal system.

The current issue included six original research articles focusing on the cavitation in hydrofoil, hybrid renewable energy systems, non-uniform soiling effect on photovoltaic panels and its impact on revenue, new detection approach of cardiac arrhythmia, performance optimisation of multiple input multiple output (MIMO) free space optical (FSO) communication system, and impulse radio (IR) based ultra wide band (UWB). All six articles deal with real-world engineering and technological challenges.

The MIJST Journal invites you to submit your scholarly unpublished, original, and innovative contributions from any branch of science, engineering, technology, and related fields. All submitted contributions go through a double-blind peer-review process with effective feedback to authors for quality and originality enhancement. All authors, reviewers and patrons are requested to disseminate and promote the Journal and its articles among colleagues, research scholars and library liaison officers.

Finally, I express my wholehearted gratitude to the Chief Patron, Executive Editor, Associate Editors, Section Editors, Reviewers, Editorial and Advisory Board Members, Proof-readers, and web production consultant for their all-out support.

Once and again, I gratefully seek your feedback, suggestion, and advice for the Journal's advancement. Please feel free to contact me via telephone +61 3 99256103 and/or email: firoz.alam@rmit.edu.au or mijst@mist.ac.bd.

Sincerely,

Prof. Dr. Firoz Alam
Editor in Chief

INDEX

MIJST
MIST International Journal of Science and Technology

Design and Analysis of Impulse Radio (IR) Based UWB Transmitter with Antenna

Shanjida Shantona[1*], Pran Kanai Saha[2], and Md. Tawfiq Amin[3]

Department of Electrical Electronic and Communication Engineering (EECE), Military Institute of Science and Technology (MIST), Dhaka, Bangladesh

emails: *[*1]shanjidaeece07@gmail.com; [2]sahapk@eee.buet.ac.bd; and [3]tawfiqamin@gmail.com*

ARTICLE INFO

Article History:

Received: 16th March 2022
Revised: 25th July 2022
Accepted: 16th August 2022
Published: 29th December 2022

Keywords:

Ultra wide band
Wireless
Transmitter
Layout
Antenna

ABSTRACT

The use of ultra-wideband (UWB) in target detection, radar and wireless connectivity, specifically in the medical world, has attracted a lot of attention. The concept that the IR-UWB system does not necessarily require carrier signals is one of its most appealing features. IR-UWB can transmit information using short Gaussian monocycle pulses. In light of these advantages, this paper proposes a novel UWB transmitter system which consists of UWB signal generating circuits and UWB antenna, which work together to create entire UWB transmitter. It is based on impulses and has a simple architecture with low power consumption. The proposed transmitter is realized in Cadence tools with 90nm CMOS technology and proposed UWB antenna is simulated using Advanced Design System (ADS) simulator software. In addition, the transmitter circuit and the antenna are co-simulated using ADS software. The illustrated UWB transmitter uses a low-power supply and generates $\mathbf{359.44}\boldsymbol{mV}$ pulse amplitude with pulse duration of $\mathbf{100}\ \boldsymbol{ps}$ for the Gaussian monocycle pulse. Due to its increased output voltage swing and reduced power consumption when comparing to other circuits, the proposed architecture is functional and suitable for use in short-range wireless networks and medical applications.

1. INTRODUCTION

Ultra-wideband (UWB) radio technology is highly applied in radar, detection and defense related applications throughout the previous few decades. Since February 2002, when the FCC approved the use of UWB for information transmission and the medical sector (Huo *et al.*, 2017a), much research has been conducted. Subsequently, this communication technology has advanced rapidly in applications demanding high speed wireless communication. UWB radio technology in imaging systems is ideal for medical devices since it allows a doctor to observe the inside status of human anatomy where no surgical process is mandatory. Whereas X-ray and ultrasound require direct touch, UWB devices can operate from a distance (Neto *et al.*, 2015). Basic logic gates are used to develop IR-based UWB transmitters. Additional circuits, like phase locked and delay-locked loops for clock and data synchronization can be included in medical devices and wireless communication design. In medical applications, short pulses generated by UWB technology is sent inside the human body and scattered signals from different organ parts are accumulated and analyzed based on the received signals. This technology reduces the need for clock synchronization and simplifies the circuitry. Numerous studies have been carried out to comprehend many features of UWB transmitter, hence facilitating newer circuit with enhanced performance parameters. However, there were more scopes to improve the performance of UWB transmitter. Some recent research (Lo *et al.*, 2013; Radic *et al.*, 2020; Bahrami *et al.*, 2015; Notch *et al.*, 2013) have designed UWB transmitter. The mentioned works has reduced the power consumption but there is huge scope of reducing the power by using different components as power consumption is one of the most important parameters for wireless medical devices. Moreover, there is also area of improvement in pulse duration and pulse amplitude since this parameter will improve the transmitter performance in terms of precision ranging, data rate and proper diagnosis. With this improvement, circuit complexity needs to be reduced so that it will be more feasible for fabrication. The above researches also not suggested UWB antenna compatible to the proposed transmission system which is also very important part of UWB transmitter. Taking all these

research gaps into considerations, a new transmitter is proposed in this work.

2. PROPOSED ULTRA-WIDEBAND TRANSMITTER

The design of UWB transmitters for communication networks has been the subject of numerous studies. These architectures considered power requirements and compactness, which are significant design concerns in communication and medical applications(Rezaei *et al.*, 2016). This research work proposes a new structure for UWB transmitter based on impulses that has most of the desired properties. UWB transmitters might employ the Gaussian monocycle pulse (GMP) generating approach to make the circuitry simple and minimize size of the circuit. The designed transmitter consumes very less power which is suitable for medical applications(Krasnov *et al.*, 2020), and moreover it does not require frequency retrieval at the output. Block diagram of the proposed transmitter with antenna is illustrated in Figure 1 where all the functional blocks are shown.

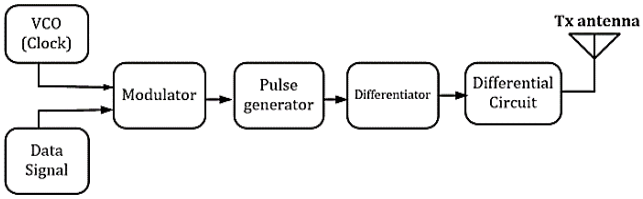

Figure 1: Block diagram of proposed IR-UWB transmitter with antenna

A. Voltage Controlled Oscillator (VCO)

The frequency of the generated signal by current starved voltage-controlled oscillator (CSVCO) is controlled by the input controlling voltage. The generated output voltage frequency can be adjusted over a wide range (Hz to GHz) by changing the regulating input(Aristov *et al.*, 2021). Another significant benefit of CSVCO is that the amplitude is maintained. Because of these benefits, a Current Starved VCO is employed in the proposed transmitter architecture, which consumes less power, has a wide range of oscillation frequencies and is simple to manufacture. The voltage-controlled oscillator included in this investigation contains three phases, as presented in Figure 2. Each delay inverter is formed by two MOSFETs (one N-channel and one P-channel), and other two function as current sources, limiting the amount of current flow through the inverter. For fluctuation of the regulating voltage from $300mV$ to $800mV$, the oscillating frequency varies from $1GHz$ to $10GHz$. The linearity of the circuit is affected by temperature.

B. OOK Modulator

When the signal is low, no carrier is sent in case of on-off keying (OOK) modulation scheme which is a basic modulation scheme for representing binary data (Hamza, 2016). For a given data rate, the signal bandwidth of a BPSK (Binary Phase Shift Keying) modulation and the signal bandwidth of an OOK modulation are the same. Furthermore, the modulator portion's digital logic circuit requires extremely little power. One of the inputs of the modulator is the clock signal generated from CSVCO and in another input binary data signal is given. If the information bit is one, this scheme delivers pulses; otherwise, no pulse is sent. The pulse frequency is determined by the clock input, and the total number of pulses is determined by the binary data signal.

C. Gaussian Pulse generator, Differentiator and Differential Circuit

Because they are affordable and simple to create, Gaussian pulses are used in short to medium communications networks. Despite the ease of the generating method, attaining pulse durations of a hundred picoseconds is tough. To generate a Gaussian pulse train either sine wave or square wave can be used (He & Zhang, 2010). In this work, a NOR gate is utilized to form a Gaussian pulse generator. OOK modulated clock signal is one of the two inputs of the NOR gates while the other is the inverted and lagged modulated clock signal(Belattar, 2018). To generate a negative Gaussian pulse, the positive Gaussian pulse is passed through an inverter(Fukuda *et al.*, 2015). These positive and negative Gaussian pulses are then differentiated using a differentiator circuit. In dual input balanced output differential amplifier circuit one input is the output of the differentiator and other input is grounded. Because of the differential form of output, the transmitter circuit is ideal for use with UWB antennas(Huo *et al.*, 2017b).The schematic diagram of transmitter circuit except antenna is shown in Figure 2.

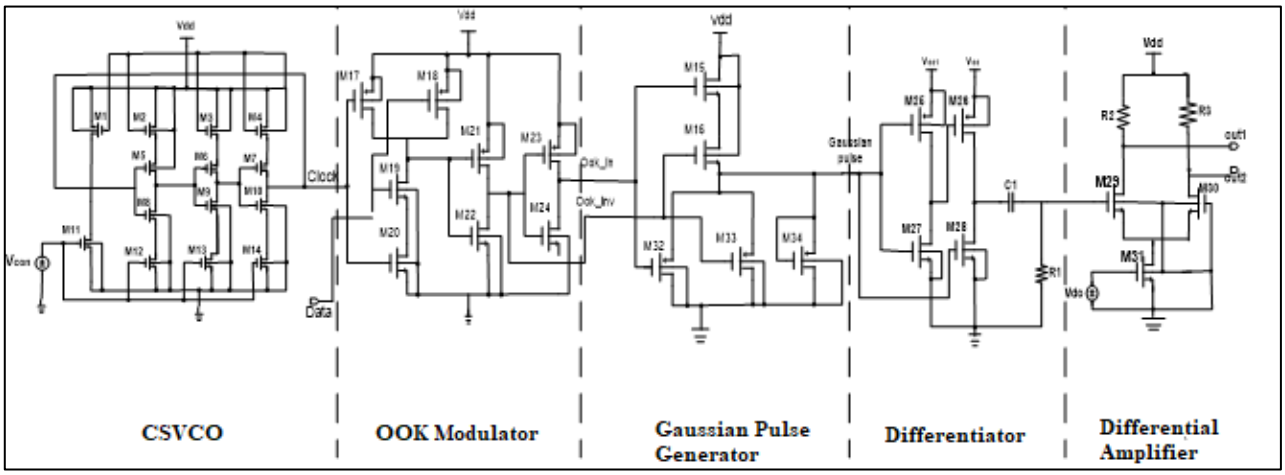

Figure 2: Architecture of proposed transmitter circuit

D. UWB Antenna Design

A simple coplanar wave guide (CPW) fed aperture antenna with UWB characteristics is designed and integrated with the proposed transmitter circuit. In (Li *et al.*, 2008), umbrella shaped antenna was proposed with bigger size. Using that concept, modifying ground plane and slotted radiation patch umbrella shaped antenna is introduced in this work. As a result, the overall size of the antenna reduced and radiation pattern and gain are also improved. Figure 3 depicts the suggested UWB antenna layout. The dimension of the antenna including ground plane corners is 32mmx28.5mm. A rectangular aperture cut out of the ground plane of a PCB and a CPW-fed umbrella-shaped radiation patch forms the antenna. The antenna is made on a moderate FR4 substrate with a dielectric constant of 4.3 and a thickness of 1.5 *mm*. The optimal dimensions of the various parts of the antenna are presented in Table 1. The end of the CPW feed line is attached to the semicircle endpoint of radius r1. The extrusion depth is 2*mm* of the umbrella-shaped patch and a semicircle slot is introduced onto the radiation patch to improve the bandwidth and gain of the designed antenna.

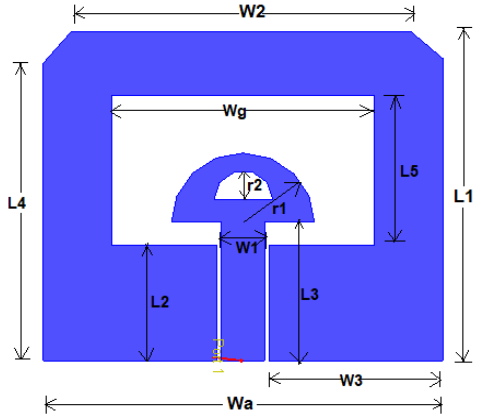

Figure 3: Geometry of the designed UWB antenna

Table 1
Antenna Dimensions, mm

L1	L2	L3	L4	L5	W1	d
28.5	10	12	26	13	3.6	1.9
W2	**W3**	**Wa**	**Wg**	**r 1**	**r 2**	**-**
28	14	32	22	6	2.3	-

A 50 Ω CPW transmission line powers the tiny rectangular aperture antenna (Gopi *et al.*, 2021).The umbrella-shaped patch is used in the designed antenna to improve the connectivity between the slot and the feed line, allowing the antenna to reach ultra-wideband performance(Li *et al.*, 2008). The upper two corner of the ground plane is modified (angular) which also improves antenna performance and reduces the size also (Bian & Che, 2008). The antenna returns loss bandwidth, radiation patterns, gain, group delay, and transmitted pulses waveform distortion were all calculated using Advanced Design System (ADS) software. The suggested antenna employs a CPW supplied technique to produce 50 *ohms* input impedance.

E. Integrating Proposed Transmitter Circuit and Antenna

At first the transmitter circuit was implemented using Cadence virtuoso software and also the layout of the different parts of the circuit were generated by using the same software. Now to integrate the circuit of the transmitter with designed UWB antenna and to do EM/circuit co-simulation of transmitter circuit and UWB antenna, Advanced Design System (ADS) software is used(Hamza, 2016). The whole circuit having CSVCO, OOK modulator, Gaussian pulse generator, differentiator and differential amplifier was co-simulated with UWB antenna using ADS software but the last two functional blocks with antenna is shown in figure 4.

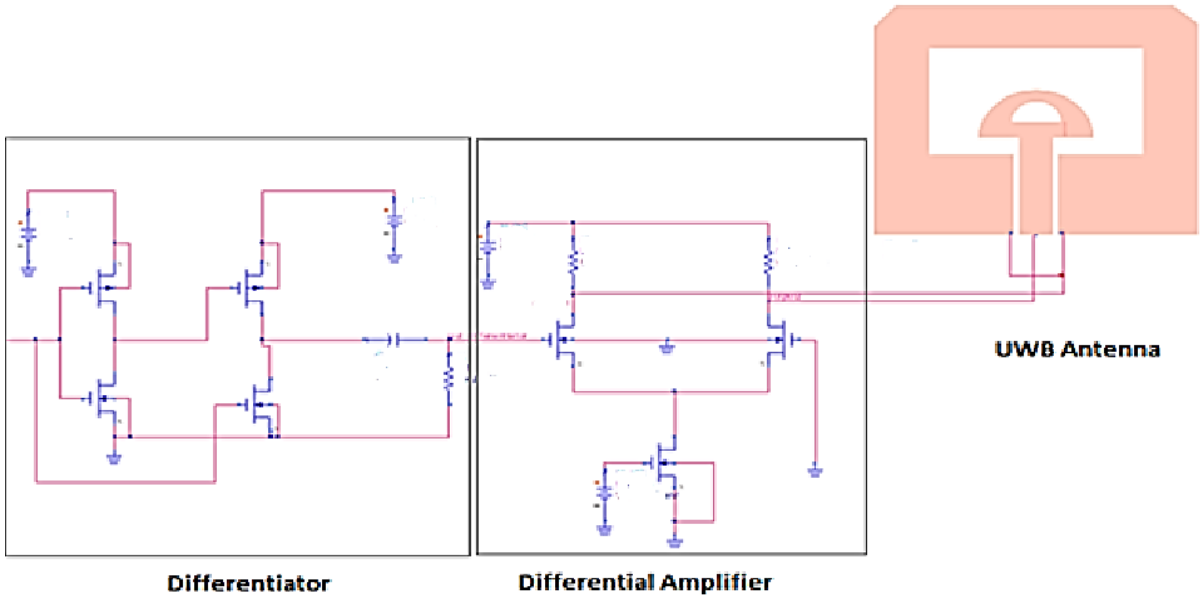

Figure 4: Schematic diagram representing integration of transmitter circuit with Antenna
(Last 2 blocks of transmitter circuit are shown with antenna)

3. RESULTS AND DISCUSSION

A. Simulated Results from Transmitter Schematic

The proposed transmitter circuitry, which was constructed using 90 nm CMOS process technology, was simulated using Cadence simulator tools. The proposed transmitter output waveforms are shown in Figure 5 at various stages. The pulse duration and pulse swing of the generated Gaussian mono pulse output are also determined from single GMP and bandwidth is determined from FFT of one GMP (Figures 6 and 7 respectively) (Ping, 2017).

From Figure 7 it is seen that the duration of pulse is $100ps$ and amplitude is $359.44mV$. Figure 6 shows the power spectral density of a single GMP, which gives a 10.6 GHz bandwidth at $-3dB$ point. Total calculated power consumption of the proposed architecture is 0.831 mW. The architecture of the pulse train also allows for higher maximum data rate while maintaining a narrow pulse width.

B. Simulated Result from Layout of Transmitter

Figures 8 to 12 show the layout of several blocks of the planned transmitter, which is implemented using Cadence tools and uses 90nm CMOS technology. The dimension of the CSVCO's is $12.64\mu m \times 16.73\mu m$, dimension of the modulator is $15.3\mu m \times 13.53\mu m$, the dimension of the Gaussian pulse generator is $10\mu m \times 15.61\mu m$, the dimension of the differentiator is $15.03\mu m \times 15.64\mu m$, and the differential amplifier measurement is $12.22\ \mu m \times 11.63\ \mu m$. The five blocks combined have a total dimension of $65.19\ \mu m \times 73.14\ \mu m$. Using a perfect sinusoidal input signal, the output characteristic curve of the schematic and layout are being examined. Only in differentiator circuit, a square wave was given as an input signal. Due to parasitic components, there is a slight discrepancy in the outputs between the schematic and the layout (Figures 13 to 17). With no errors, the layout passed the $90nm$ CMOS design rule check (DRC), as well as the LVS and RC checks, ensuring a successful design following fabrication.

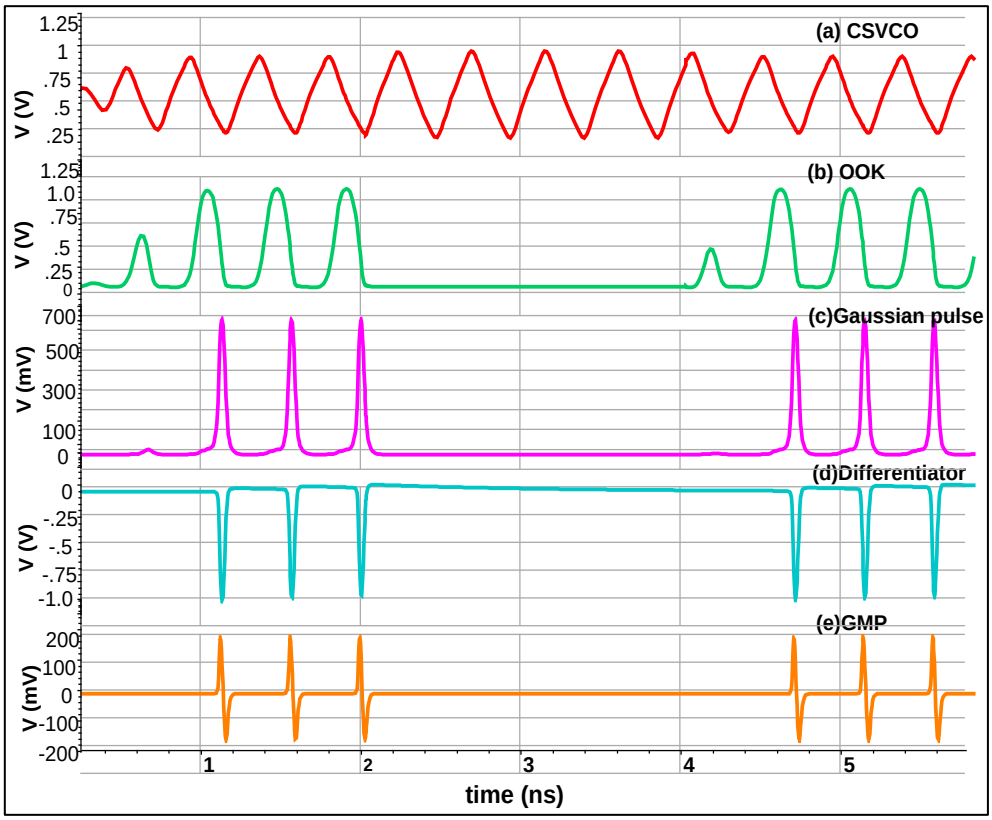

Figure 5: Output at different stages of proposed transmitter

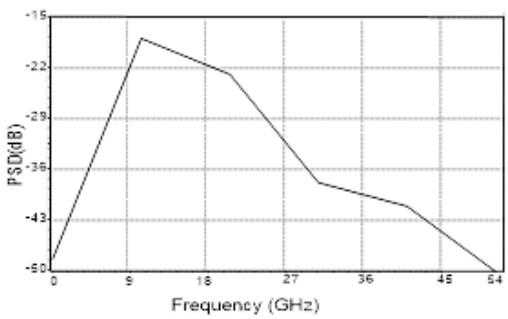

Figure 6: Power spectral density of single GMP

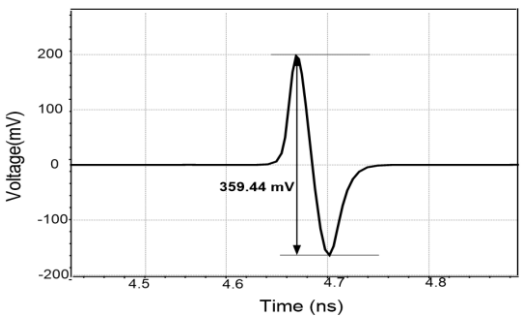

Figure 7: Gaussian monocycle pulse (single)

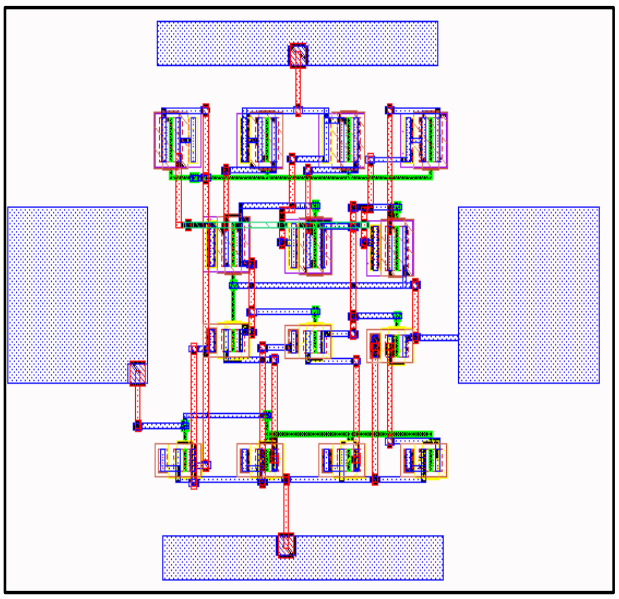

Figure 8: CSVCO layout

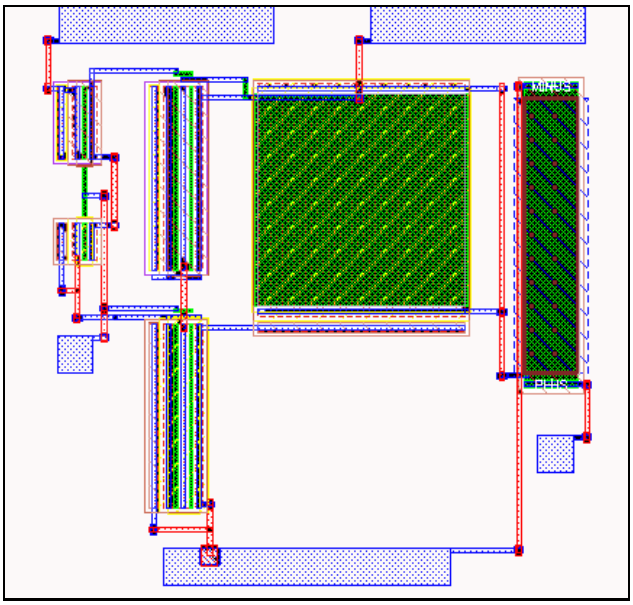

Figure 11: Differentiator circuit layout

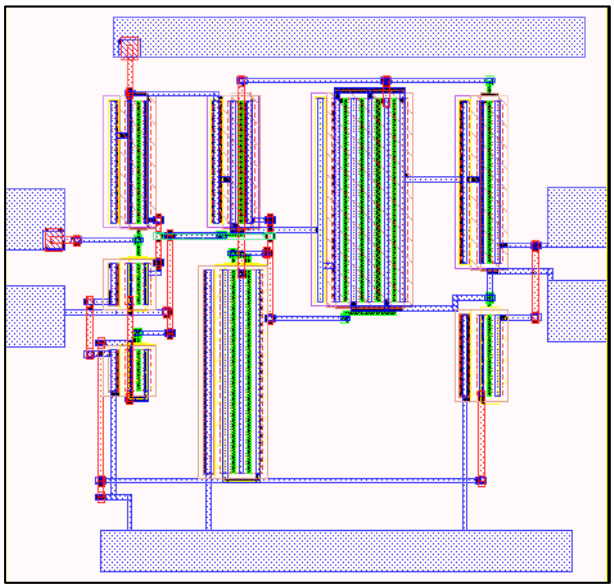

Figure 9: OOK modulator layout

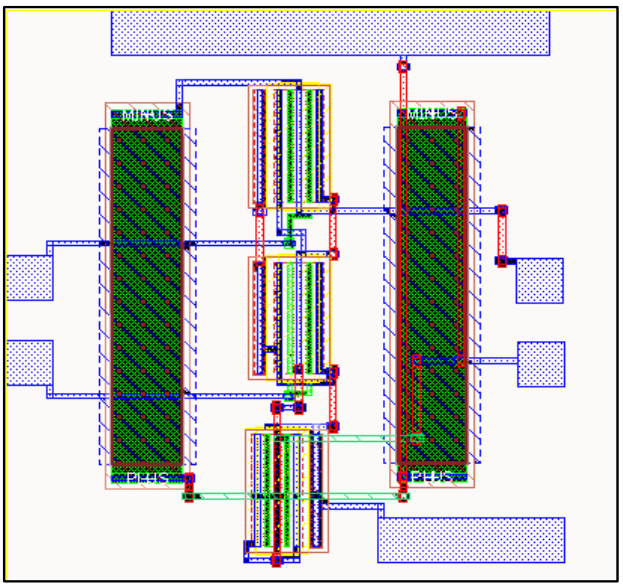

Figure 12: Differential circuit layout

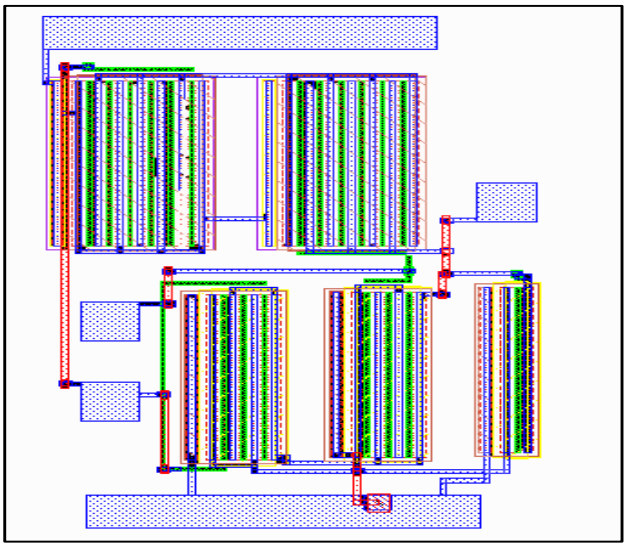

Figure 10: GP generator layout

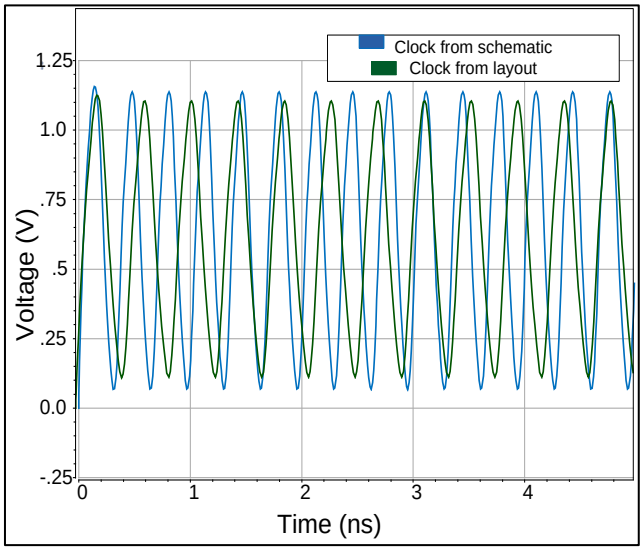

Figure 13: Layout and schematic output of CSVCO

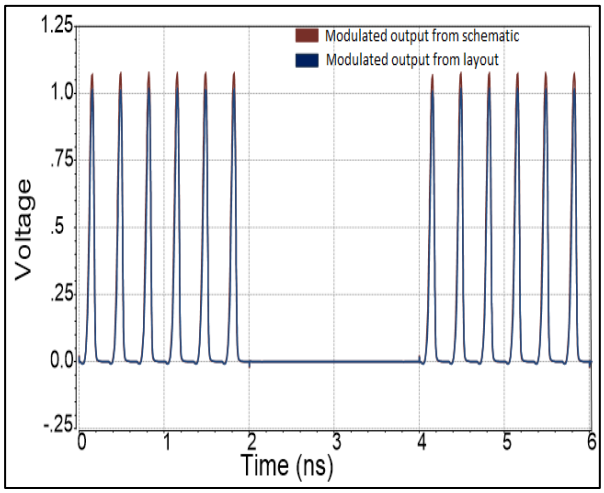

Figure 14: Layout and schematic output of OOK modulator

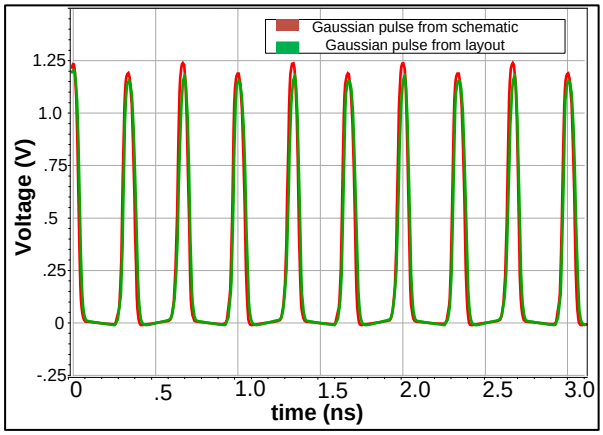

Figure 15: Layout and schematic output of GP generator

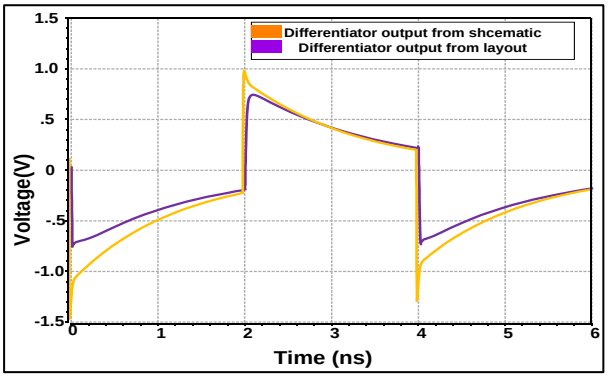

Figure 16: Layout and schematic output of differentiator

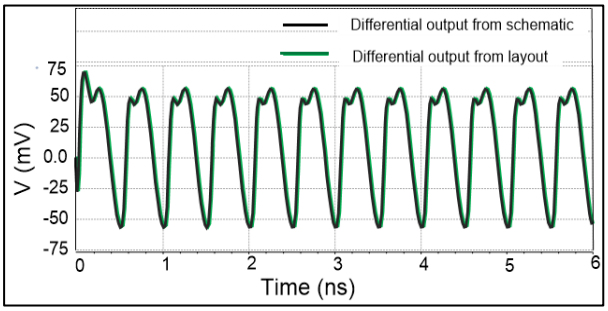

Figure 17: Layout and schematic output of Differential Amplifier

C. Process Corner Analysis of Designed Ultra-Wideband Transmitter

Any circuit based on devices generated at some of these process corners can function at high or low temperatures and voltages than needed, as well as slower or quicker than required (Osipov & Paul, 2017). As a result, an assessment of the suggested transmitter's process corners is also carried out to ensure that the designed transmitter functions properly at various process corners and temperatures.

The Simulated output for the NN, SS, SF, FS, and FF situations differs (Figure 16). Even, when the process or temperature change, the transmitter offers adequate pulse duration and bandwidth and pulse amplitude (Figure 19).

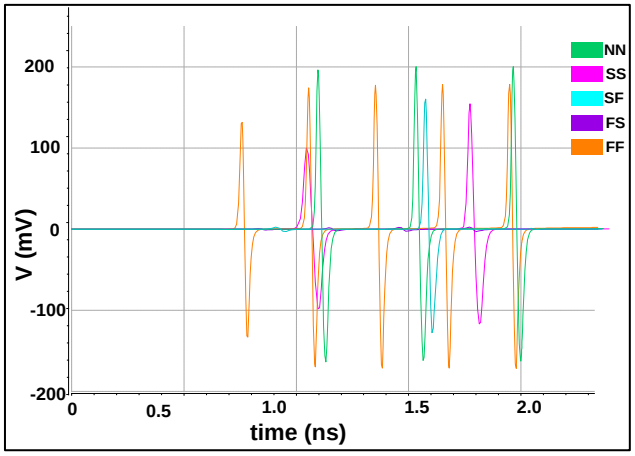

Figure 18: Output Gaussian pulse at (a) different process corner

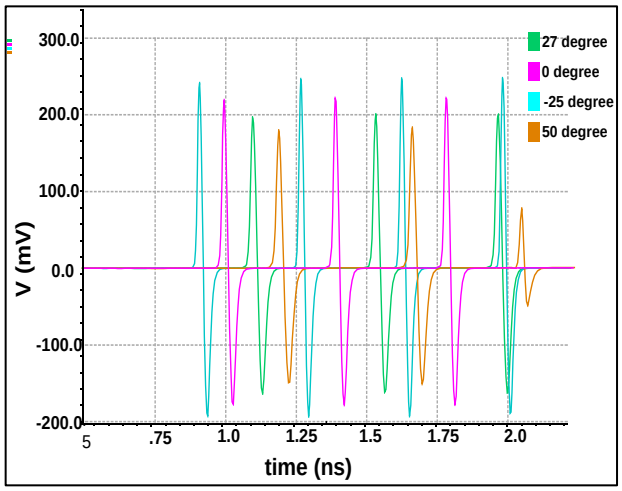

Figure 19: Output Gaussian pulse at different temperature

D. Simulated Outputs of transmitter and antenna using ADS software

Figure 20 illustrates the output GMP from proposed UWB transmitter simulated using ADS simulator which is same as the previously generated GMP from Cadence software. The return loss of the CPW fed UWB aperture antenna is shown in Figure 21. The suggested antenna fulfills the $-10\ dB$ return loss $(3.1 - 10.6)$ GHz.

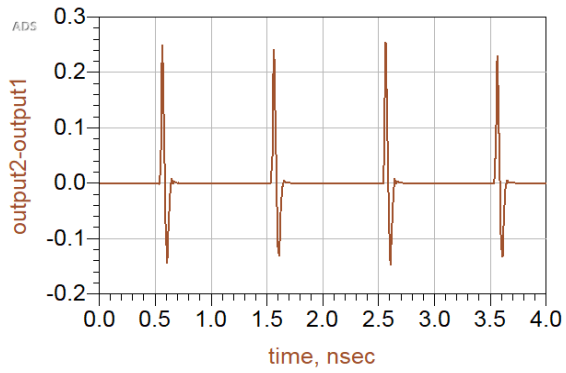

Figure 20: Output GMP from ADS simulator

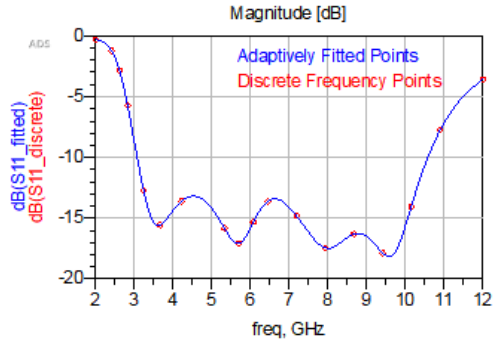

Figure 21: Return Loss of proposed UWB Antenna

The simulation of current distribution on the surface of proposed antenna at specified frequencies of 6 GHz and 10 GHz is shown in Figure 22 (Uwb & Itapu, n.d.). Figure 23 shows the s-parameter obtained from EM/circuit simulation of transmitter circuit and antenna (from circuit set-up of Figure 4).

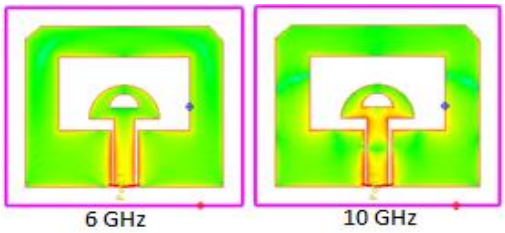

Figure 22: Simulated current distributions on the surface of the proposed antenna

Figure 23 depicts an ADS 3D representation of the proposed antenna's predicted radiation pattern at (6 GHz, 10 GHz). According to simulated result shown in Figure 23, the antenna has steady radiation patterns over the UWB, and the direction of greatest radiation is always around the z-axis (normal to the aperture plane). Figure 24 shows the antenna return loss after connecting the antenna with transmitter circuit which is obtained from EM/circuit co-simulation using ADS software. From this result it is seen that even after being connected with designed transmitter, the antenna fulfills the -10 dB return loss for ultra-wide bandwidth.

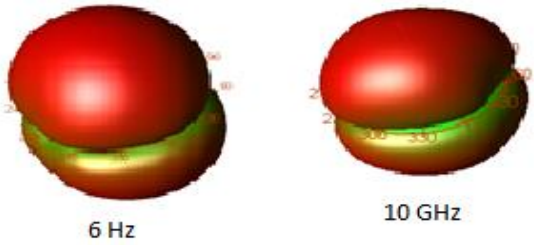

Figure 23: 3D plot of radiation pattern of proposed antenna

Figures 25 and 26 show the proposed antenna's gain, directivity, radiated power and absolute fields. Data was simulated at two different frequencies (**6 *GHz*** and **10 *GHz***). The information is displayed as 2-dimensional slices of a 3-dimensional radiation pattern.

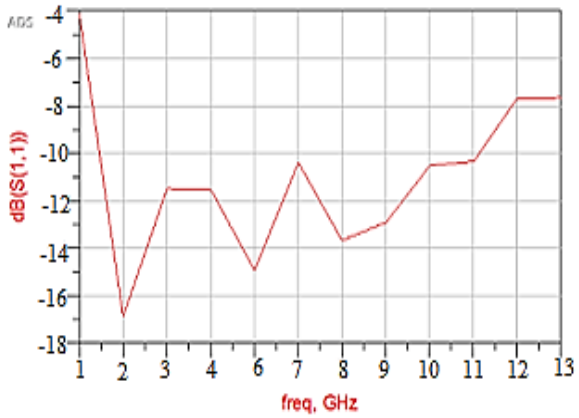

Figure 24: Antenna return loss from EM/circuit co-simulation

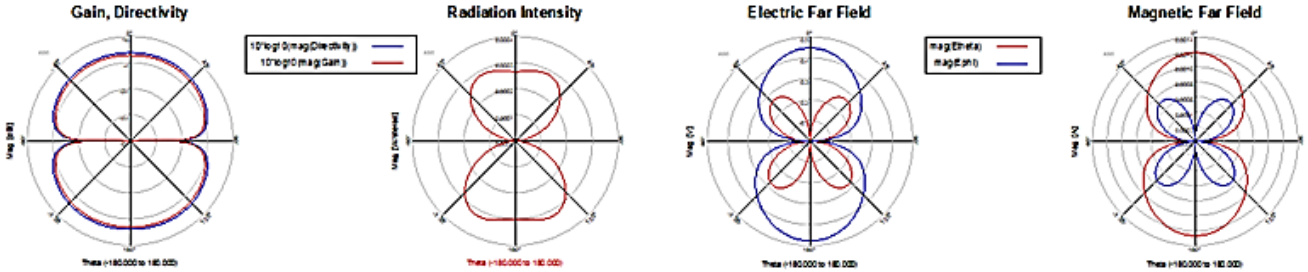

Figure 25: Gain, Directivity, Radiated power and Absolute Fields of the proposed antenna at 6 GHz.

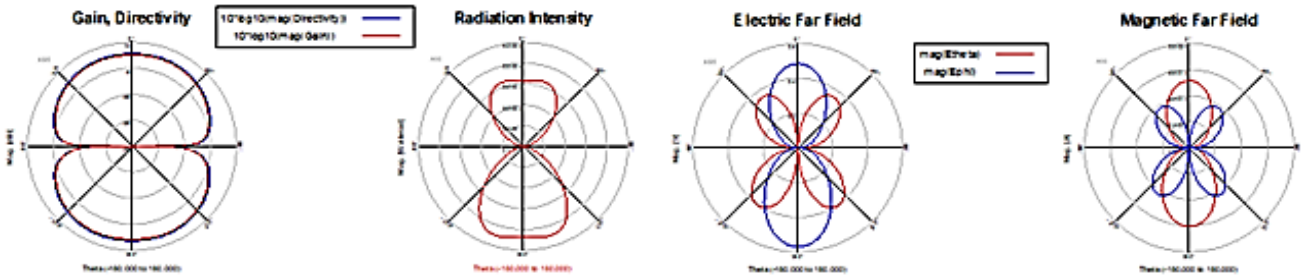

Figure 26: Gain, Directivity, Radiated power and Absolute Fields of the proposed antenna at **10 GHz**

Table 2
Comparison of Presented Transmitter Parameters with Previous Works

Ref	Technology	Si Area (mm^2)	Power Con. (mW)	Energy (pJ/b)	Output Pulse width (ps)	Modulation technique
(Lo *et al.*, 2013)	180nm CMOS	1.37 x 1.37	11.8	98.3	1000	OOK
(Radic *et al.*, 2020)	180nm CMOS	0.63 x 0.63	1	5	600	OOK
(Bahrami *et al.*, 2015)	180nm CMOS	0.10 x 0.10	5.4	10.8	800	OOK
(Notch *et al.*, 2013)	90nm CMOS	1.38 x1.38	26.4	65	2500	BPSK
This work	**90nm CMOS**	**0.065x0.073**	**0.831**	**3.324**	**100**	**OOK**

To illustrate the contribution of this research work in the field of UWB transmitter in medical applications, above table is presented which is showing in the comparison between the important output parameters of the presented transmitter with other reference papers which were followed during this work.

9. CONCLUSIONS

Because of its less complex circuitry and low consumption of power, a UWB transmitter is ideal for medical devices applications, remote patient monitoring wireless networking, intra chip communication and short distance local area networks. The presented structure consumes $0.831\ mW$ power in total. This study proposes a complete impulse radio-based UWB transmitter on $90nm$ CMOS technology along with antenna. The simulated output waveforms obtained demonstrate the transmitter's capability. It is also possible to use a higher-order differentiator circuit. Other Gaussian pulse derivatives can also be constructed with intra chip silicon UWB antenna in the future.

ACKNOWLEDGEMENTS

The authors would like to express their gratitude to the Department of EECE, MIST, Bangladesh. They are also thankful to the editors and reviewers of the MIJST for the suggestions and comments to improvement the contents of the manuscript.

REFERENCES

Aristov, V., Gaigals, G., Supols, G., Lobanovs, E., Riekstins, V., & Zujs, V. (2021). Ultra-Wideband Pulse Radar with Discrete Stroboscopic Receiver for Detection of Small Targets behind Dielectric Obstacles. Transport and Telecommunication, 22(2), 196–206. https://doi.org/10.2478/ttj-2021-0015

Bahrami, H., Mirbozorgi, S. A., Rusch, L. A., & Gosselin, B. (2015). Integrated UWB Transmitter and Antenna Design for Interfacing High-Density Brain Microprobes. 2015 IEEE International Conference on Ubiquitous Wireless Broadband, ICUWB 2015, 0–4. https://doi.org/10.1109/ICUWB.2015.7324465

Belattar, M. (2018). Chapter III : Phase Shift Keying modulation and demodulation. February.

Bian, L., & Che, X. (2008). Application of Equivalent Circuit Method in Designing the Vivaldi UWB Antenna. 2008 4th International Conference on Wireless Communications, Networking and Mobile Computing, 1–3. https://doi.org/10.1109/WiCom.2008.256

Fukuda, M., Saha, P. K., Sasaki, N., Nitta, M., & Kikkawa, T. (2015). A 0.18 μm CMOS Impulse Radio Based UWB Transmitter for Global Wireless Interconnections of 3D Stacked-Chip System. 23(12), 142–143. https://doi.org/10.7567/ssdm.2006.c-2-5

Gopi, D., Raju, A., & Kumar, V. J. R. K. (2021). DGS based monopole circular - shaped patch antenna for UWB applications. SN Applied Sciences, 3(2), 1–12. https://doi.org/10.1007/s42452-020-04123-w

Hamza, H. A. (2016). Design of CMOS IR-UWB Transmitter Design of CMOS IR-UWB Transmitter. December.

He, J., & Zhang, Y. (2010). A CMOS differential fifth-derivative Gaussian pulse generator for UWB applications. Microwave and Optical Technology Letters, 52, 1849–1852. https://doi.org/10.1002/mop.25342

Huo, Y., Dong, X., & Lu, P. (2017a). Ultra-wideband transmitter design based on a new transmitted reference pulse cluster. ICT Express, 3(3), 142–147. https://doi.org/10.1016/j.icte.2017.07.001

Huo, Y., Dong, X., & Lu, P. (2017b). Ultra-wideband transmitter design based on a new transmitted reference pulse cluster. ICT Express, 3(3), 142–147. https://doi.org/10.1016/j.icte.2017.07.001

Krasnov, T. V., Garifullin, V. F., Feoktistov, D. S., Bondarenko, V. N., & Baturin, T. N. (2020). Research of data transmission system based on UWB technology. Journal of Physics: Conference Series, 1515(2). https://doi.org/10.1088/1742-6596/1515/2/022063

Li, Z., Zhang, C. X., Wang, G. M., & Su, W. R. (2008). Designs on CPW-fed aperture antenna for ultra-wideband applications. Progress In Electromagnetics Research C, 2, 1–6. https://doi.org/10.2528/PIERC08030501

Lo, Y. T., Yui, C. C., & Kiang, J. F. (2013). OOK/BPSK-modulated impulse transmitters integrated with leakage-cancelling circuit. IEEE Transactions on Microwave Theory and Techniques, 61(1), 218–224. https://doi.org/10.1109/TMTT.2012.2226746

Neto, J. F., Moreira, L. C., Ferauche, T., Correra, F. S., & Van Noije, W. A. M. (2015). A design of a BPSK transmitter front end for ultra-wideband in 130nm CMOS. SBMO/IEEE MTT-S International Microwave and Optoelectronics Conference Proceedings, 2015-Decem, 5–9. https://doi.org/10.1109/IMOC.2015.7369175

Notch, W. I., Hedayati, H., Member, S., & Entesari, K. (2013). A 90-nm CMOS UWB Impulse Radio Transmitter. 61(12), 4220–4232.

Osipov, D., & Paul, S. (2017). Temperature-Compensated β-Multiplier Current Reference Circuit. IEEE Transactions on Circuits and Systems II: Express Briefs, 64(10), 1162–1166. https://doi.org/10.1109/TCSII.2016.2634779

Ping, L. C. (2017). Equivalent circuit model of octagonal ultra wideband (UWB) antenna. Journal of Engineering Science and Technology, 12(2), 439–450.

Radic, J., Brkic, M., Djugova, A., Videnovic-Misic, M., Goll, B., & Zimmermann, H. (2020). Ultra-low power low-complexity 3-7.5 GHz IRUWB transmitter with spectrum tunability. IET Circuits, Devices and Systems, 14(4), 521–527. https://doi.org/10.1049/iet-cds.2019.0392

Rezaei, M., Bahrami, H., Mirbozorgi, A., Rusch, L. A., & Gosselin, B. (2016). A short-impulse UWB BPSK transmitter for large-scale neural recording implants. Proceedings of the Annual International Conference of the IEEE Engineering in Medicine and Biology Society, EMBS, 2016-Octob, 6315–6318. https://doi.org/10.1109/EMBC.2016.7592172

Uwb, A. G., & Itapu, S. (n.d.). A 3 – 18 GHz UWB Antenna with modi ed feed-line. 1–14.

MIJST
MIST International Journal of Science and Technology

Numerical Analysis of Cavitating Flow on Hydrofoil

Md Nur-E-Mostafa[1*], Eare Md Morshed Alam[2], and Mohammad Monir Uddin[3]

[1,2]Department of Science and Humanities, Military Institute of Science and Technology (MIST), Dhaka, Bangladesh
[3]Department of Mathematics and Physics, North South University (NSU), Dhaka, Bangladesh

emails: *[*1]mostafa@sh.mist.ac.bd; [2]morshed5361@gmail.com; and [3]monir.uddin@northsouth.edu*

ARTICLE INFO

Article History:

Received: 28th March 2022
Revised: 30th May 2022
Accepted: 30th August 2022
Published: 29th December 2022

Keywords:

Cavitation value
Mixure model
RNG k-ε *turbulence model*
Irregular flow

ABSTRACT

Numerical study is presented in this work for turbulent cavitating flow pattern simulation on a hydrofoil, using state equation of cavitation model along with combined turbulence model for mixed fluid based on commercial software FLUENT 6.0. This solver is based on finite volume method. Cavitating study yield irregular behavior with the variation of cavitation values (σ). This study is focused on pressure variation, vapor volume fraction, lift and drag forces on the foil section for various cavitation values at 7° angle of attack. Cavitation initiation begins at the foremost surface and covers towards the end chord with reducing cavitation value. Moreover, the change of vapor region pattern is predicted towards the front of the foil. Finally, transitional flow range is observed for σ values 0.8 to 1.2 with large standard deviation.

1. INTRODUCTION

Cavitation is the specific two-phase flow with the process or a period of changing from vaporization to condensation determined by pressure variation without any producing heat. It may be deduced as the suddenly burst of the liquid owing to excessive pressure. According to ref (Brenne 1955), cavitation can be defined, process of bursting a liquid by reducing pressure at approximately constant liquid temperature. Pressure in the liquid is reduced to its vapour pressure at any point in the flow, then the liquid will be boiled at that point and bubbles of vapour will form (Kothandaraman *et al.* 2007). Since the fluid flows into an area of higher pressure the bubbles of vapour will rapidly condense or collapse. This action yields very high dynamic pressure upon the contiguous material surface and as the action is continual and has a large frequency the solid in that region will be gradually damaged. Turbo machine, pump impellers and airfoil type blade etc. are often occurred cavitation and severely damaged repeatedly. Cavitation causes hydrodynamic problem near the contiguous solid surface like increasing drag force, pressure pulsation and changing kinematics fluid flow.

These obvious problems are strongly related to instantaneous behavior of cavitating flow assembly and causes unsteady fluctuations upon the surface at the cavitation area. Hence, good understanding of the problem, the numerical study of cavitating behavior is important for prediction. Therefore, many numerical studies and investigation were carried out in previous (Kubota *et al* 1992, Kunz *et al*. 2000, Schnerr *et al.* 2001, Stutz *et al.* 2002, and Frobenius *et al. 2003).*

In the past decade several methods were developed for numerical simulation of the physics for cavitating flow pattern. Mixture and VOF model is considered the efficient method for the numerical analysis of cavitating study. Most studies are based on the mixture consideration of homogeneous fluid composed by two phase flow which assumed a single mixture flow of fluid-vapor. Two phase mixture model flow was applied for simulation of the present study and previously done by (Karim *et al* 2010 and Mostafa *et al*. 2016). Roohi *et al.* 2012 studied the cavitating behavior by VOF model. A cavitation model is also used here based on phase change and bubble dynamics equation for calculating of unsteady behavior of cavitating flow. Singhal *et al.* (2002) suggested a comprehensive cavitation model by adding the void ratio with vaporization and condensation source terms in a transport equation to regulate the mass shift between two phases. In this study, full cavitation model is used.

Impact of fine mesh generation and chosen of turbulence model is separately analyzed by comparing numerical values of lift coefficent and drag coefficient for non-cavitating flow previously (Karim *et al.*, 2010; Mostafa *et al*., 2016). To calculate unsteady behavior of cavitation around the hydrofoil, we used RNG k-ε turbulence model with improved wall function. Now, the flow pattern of pressure

distribution, contour of pressure coefficient and vapor volume fraction on the top foil surface is separately analyzed. Peak values of pressure coefficient are found increasing in cavitation zone with the decrease of σ values.

2. NUMERICAL SIMULATION

To capture cavitation zone over the hydrofoil, implicit finite volume scheme allied with multiphase mixture model and bubble dynamic cavitation model are used. We applied RNG k-ε turbulence model including improved wall function to comprehend the boundary layer. Calculation of Reynolds number in this work is 5.9×10^{-5} where foil chord length is considered the characteristics dimension. Amount of y^+ is 5-15 obtained by (Karim *et al.*, 2010). Second order central difference approximation is applied to discretize the pressure, viscosity and source terms. In addition, in the momentum equation, the convective term is discretized by implicit second order approximation. Semi-Implicit Method for Pressure-Linked Equations (SIMPLE) is a pressure based solver which is used to solve the incompressible equation

3. MULTIPHAGE MIXTURE MODEL

To modelled the cavitating flows, a mixture model of multiphase flow is applied. Density (ρ_m) of mixture is linked with vapor mass fraction (f_v). In this study, it is derived from the transport equation and turbulence model equation as well as momentum and mass conservation equations. Density of mixture and mass fraction (f_v) of fluid vapour relation was showed by (Dular *et al.* 2005) as follows.

$$\frac{1}{\rho_m} = \frac{f_v}{\rho_v} + \frac{1-f_v}{\rho_l} \tag{1}$$

The relation between vapour phase volume fraction (α_v) and vapour phase mass fraction (f_v) is obtained as:

$$\alpha_v = f_v \frac{\rho_m}{\rho_v} \tag{2}$$

Mass conservation equation for mixture flow is:

$$\frac{\partial}{\partial t}(\rho_m) + \nabla.(\rho_m \vec{v}_m) = 0 \tag{3}$$

Equation of momentum conservation for the mixture flow is:

$$\frac{\partial}{\partial t}(\rho_m \vec{v}_m) + \nabla.(\rho_m \vec{v}_m \vec{v}_m) = -\nabla p + \nabla.[\mu_m(\nabla \vec{v}_m + \nabla \vec{v}_m^T)] + \rho m \vec{g} + \vec{F} \tag{4}$$

The vapour transport equation is:

$$\frac{\partial}{\partial t}(\rho_m f_v) + \nabla.(\rho_m \vec{v}_m f_v) = M_e - M_c \tag{5}$$

4. CAVITATION MODEL

It is considered that, in cavitating situations, the operating fluid consists of mixture of vapour, non-condensable gas and liquid. The liquid evaporation and vapour condensation expression are defined as M_e and M_c respectively which are added in the vapour transport equation. The comprehensive cavitation model is assumed on focusing the transport equations as:

$$M_e = C_e \frac{\sqrt{k}}{\gamma} \rho_l \rho_v \sqrt{\frac{2}{3}\frac{p_v - p}{\rho_l}} \left(1 - f_v - f_g\right) \; when \; p < p_v \tag{6}$$

$$M_c = C_c \frac{\sqrt{k}}{\gamma} \rho_l \rho_l \sqrt{\frac{2}{3}\frac{p_v - p}{\rho_l}} f_v \; \; when \; \; p > p_v \tag{7}$$

Where the proposed numerical value of empirical constants C_e is 0.02 and C_c is 0.01. In addition, other notation and symbols represents the usual meaning.

5. RNG $k-\varepsilon$ TURBULENCE MODEL

By analyzing the turbulence model in FLUENT, we picked out the RNG $k-\varepsilon$ model for this study. This model is found effective in precisely resolving the near wall zone when the two phase model is used. Choudhury (1993) derived the RNG $k-\varepsilon$ model from the instantaneous Navier-Stockes equation using mathematical procedure called "renormalization group" (RNG). The analytical derivation is almost alike in feature to the standard $k-\varepsilon$ model but includes an extra terms R_ε in its ε equation. The additional term enhances the precision for quickly stained flows significantly. The state equations of the RNG $k-\varepsilon$ model are known by:

$$\frac{\partial}{\partial t}(\rho k) + \frac{\partial}{\partial x_i}(\rho k u_i) = \frac{\partial}{\partial x_j}\left(\alpha_k \mu_{eff} \frac{\partial k}{\partial x_j}\right) + G_k + G_b - \rho\epsilon - Y_m + S_k \tag{8}$$

$$\frac{\partial}{\partial t}(\rho \varepsilon) + \frac{\partial}{\partial x_i}(\rho \varepsilon u_i) = \frac{\partial}{\partial x_j}\left(\alpha_\varepsilon \mu_{eff} \frac{\partial \varepsilon}{\partial x_j}\right) + C_{1\varepsilon}\frac{\varepsilon}{k}(G_k + C_{3\varepsilon}G_b) - C_{2\varepsilon}\rho\frac{\varepsilon^2}{k} - R_\varepsilon + S_\varepsilon \tag{9}$$

where, $C_{1\varepsilon} = 1.42$ and $C_{2\varepsilon} = 1.68$.

The additional term R_ε included in Equation (14) is given as follows:

$$R_\varepsilon = \frac{C_\mu \rho \eta^3 (\eta - \eta/\eta_0)}{1+\beta\eta^3} \frac{\varepsilon^2}{k} \tag{10}$$

where, $\eta \equiv Sk/\varepsilon$, $\eta_0 = 4.38$, $\beta = 0.012$

6. FLOW GEOMETRY AND COMPUTATIONAL AREA

CAV2003 hydrofoil cross section is placed in Figure 1 which demonstrate a diagrammatic view geometry and calculation domain. It is located at attack of angle 7° with nominally two dimensional configuration. The leading surface equation of the axisymmetric foil is shown in equation (11):

$$\bar{y} = 0.11858(\bar{x})^{\frac{1}{2}} - 0.02972(\bar{x}) + 0.00593(\bar{x})^2 + -0.07272(\bar{x})^3 + -0.002207(\bar{x})^4 \tag{11}$$

Where $\bar{x} = x/c$ and $\bar{y} = y/c$ are denoted as dimensionless quantity and c is chord of length 0.1m. The flow field is considered incompressible fluid which moving from left flow field to right flow field along the hydrofoil. The computational flow field domain is chosen of dimension 10c length in the direction of x-axis and height 4c in the direction of y-axis. The hydrofoil is set up at the central of the calculating domain. The proper boundary conditions of all boundaries are also shown in Figure 1. The uniform flow velocity profile is fixed 6 m/s at the entrance boundary

condition. Symmetry boundary type is considered as a slip wall illustrated in Figure 1. The constant pressure boundary outlet condition is presented at the far field of the domain. We apply foil surface as no-slip wall.

In order to select a fine grid lines in mesh for flow domain, a detailed grid analysis was done in past by the published work ref (Karim *et al.* 2010). A particular grid with computational domain is illustrated in Figure 2.

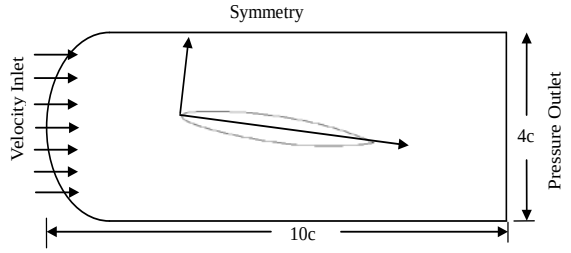

Figure 1: Diagrammatic view of CAV2003 hydrofoil, flow domain and set boundary condition

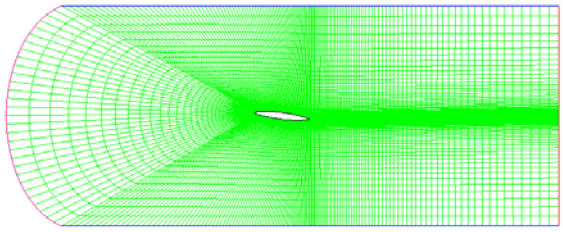

Figure 2: A inclusive view of fine grid lines with computational domain

7. RESULTS AND DISCUSSION

The convergence benchmark is resolved by observing various features of estimation of flow, such as inlet velocity and static pressure at the back of hydrofoil in the flow field. The computational residual value is taken as 10^{-4}. The mass fraction of non-condensable gas is an important parameter of FLUENT. It is observed that results are reasonably sensitive to the value of non-condensable gas. Based on the initial test calculation the convergence criterion value 10^{-6} is found to give rational results and use for the present work. For computation of cavitating flow, the other initial parameters are shown in Table 1.

Table 1
Initial condition for simulation

Parameters	Values
Re	5.9×10^5
Attack angle	7°
Velocity	6.0 m / s
ρ_l	998.0 kg/m^3
ρ_v	0.5542 kg/m^3
μ_l	10^{-3}
P_{ref}	101325 Pa
P_v	98929.32 Pa
Time step	5×10^{-5}
Per time step	30 iteration
μ_v	$1.34 \times 10^{-5} Pa$
Surface tension, γ	0.0717 N/M

For good understanding of the cavitating flow behavior on the hydrofoil, numerical analysis has been done for the various σ values 0.4, 0.8, 0.9, 1.0, 1.1, 1.2, 1.5 and 3.5. We compare the computed result for σ values at 0.8 and 0.4 with published results of different authors for validation purpose and comparative analysis.

The comparison is carried out for the calculating time dependent lift value and drag value with the numerical result of (Pouffary *et al.* 2003; Mortazazadeh *et al.* 2014; Kawamura *et al.* 2003; and Yoshinori *et al.* 2003). As shown in Table 2, the computed time averaged lift values and drag values are seen in well agreement with available result of various researchers. For cavitation number 0.8, the calculated values of lift coefficient and drag coefficient using present method are more consistences and comply with result of (Pouffary *et al.* 2003). Though, there is seen a little inconsistency for the cavitation value 0.4. This phenomenon may be ascribed owing to the fact that many authors used various turbulence models.

The computed pressure variation curve on the suction side of foil top surface at σ values 0.4 & 0.8 is illustrated in Figure 3 and 4 respectively, together with pressure curve of (Kawamura *et al.* 2003). A good consistency trend is observed except in tailing edge. This little discrepancy in magnitude may be happened due to (Kawamura *et al.* 2003) used *k-ω* turbulence model.

Table 2
Lift values and drag values for cavitation numbers at 0.8 & 0.4

	σ value 0.8		*σ value 0.4*	
	lift	**drag**	**lift**	**drag**
Current result	0.442	0.0773	0.214	0.0763
Mortazazadeh	0.413	0.068	-	-
Pouffary	0.4566	0.0783	0.2911	0.0866
Courtier-Delgosha	0.4501	0.0700	0.2001	0.0650
Kawamura	0.3990	0.0470	0.1870	0.0630
Yoshinori	0.4170	0.0638	0.1600	0.0568

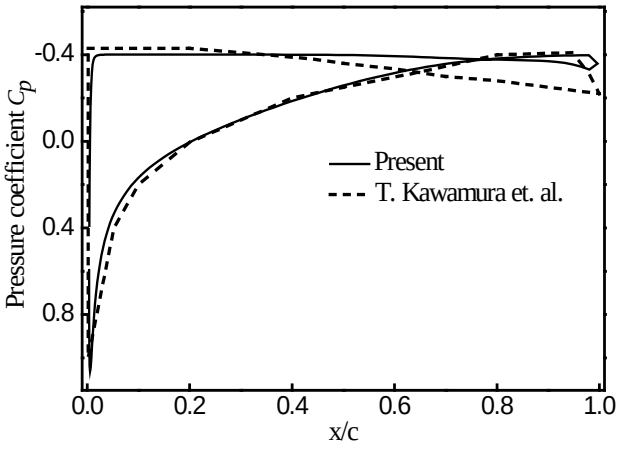

Figure 3: Comparing the variation of pressure coefficient on the top edge of the foil at cavitation values 0.4

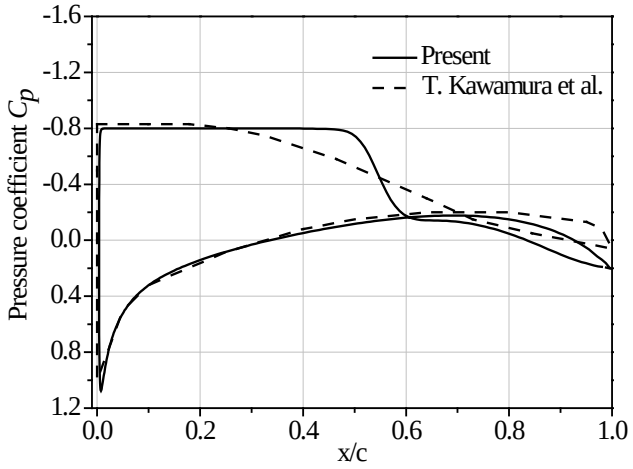

Figure 4: Comparing the variation of pressure coefficient on the top edge of the foil at cavitation values 0.8

The exit pressure distribution on the hydrofoil top surface varied to yield the different cavitation values ($\sigma = 0.4, 0.8, 0.9, 1.0, 1.1, 1.2, 1.5, 3.5$) are presented in Figure 5(a-f). Cavitation initiation starts at the upstream surface of the foil and gradually grows towards the end chord with reducing cavitation value. The maximum values of pressure distribution in area of cavitation is developed with the decreasing of cavitation values.

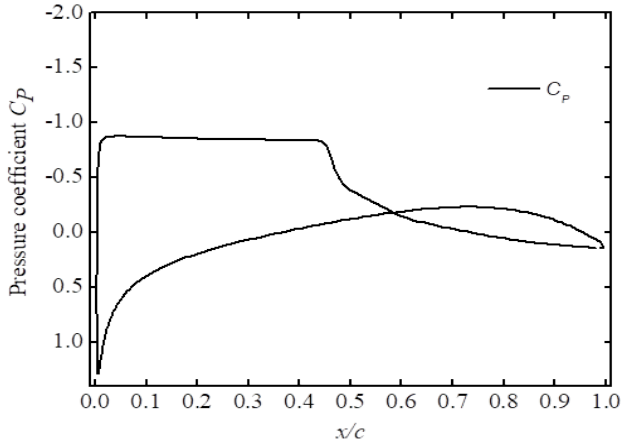

Figure 5 (a): Variation of pressure coefficient on the top edge of the foil at cavitation values 0.9

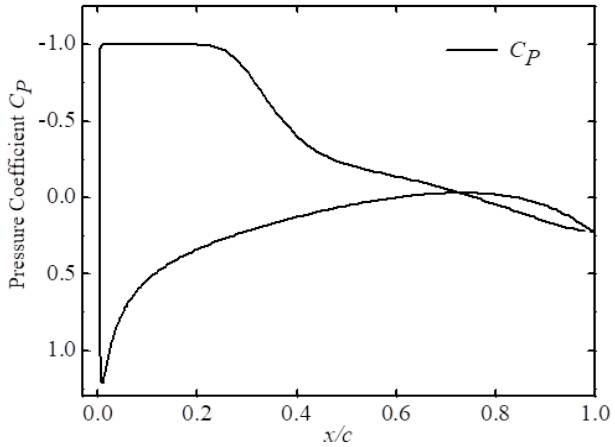

Figure 5 (b): Variation of pressure coefficient on the top edge of the foil at cavitation values 1.0

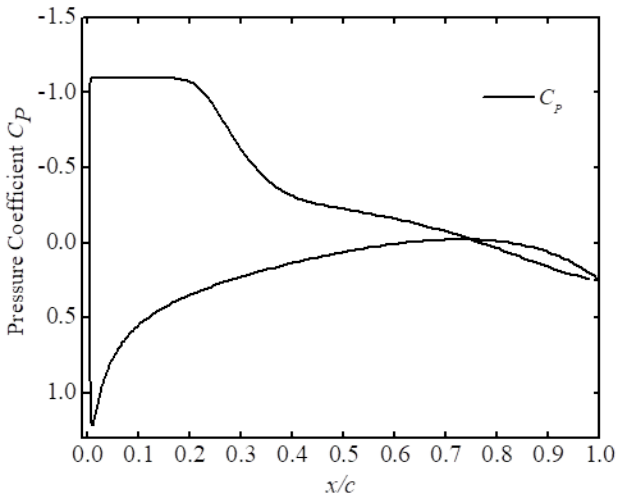

Figure 5 (c): Variation of pressure coefficient on the top edge of the foil at cavitation values 1.1

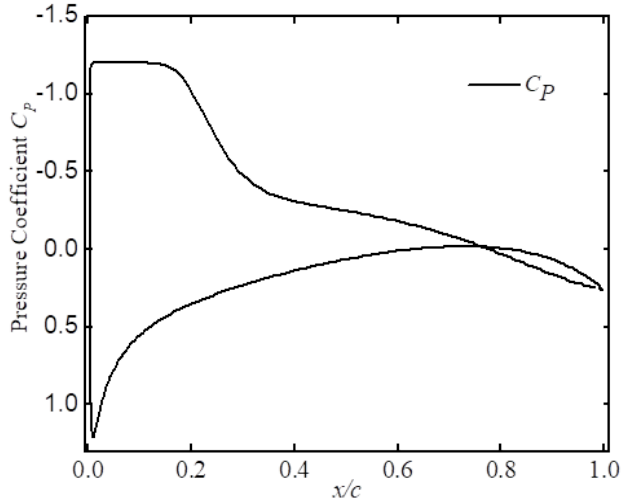

Figure 5 (d): Variation of pressure coefficient on the top edge of the foil at cavitation values 1.2

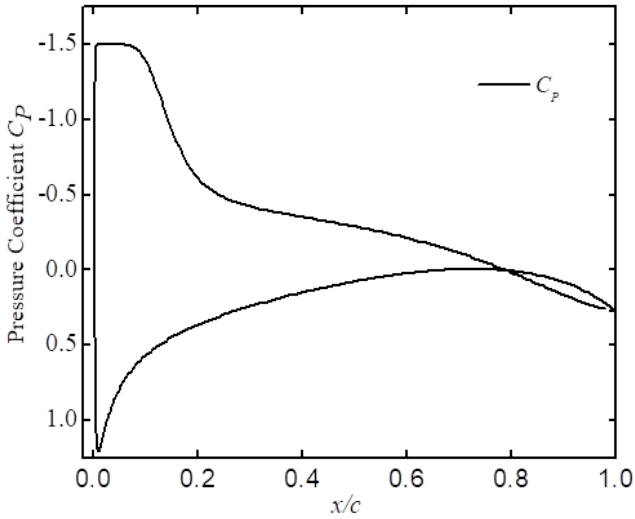

Figure 5 (e): Variation of pressure coefficient on the top edge of the foil at cavitation values 1.5

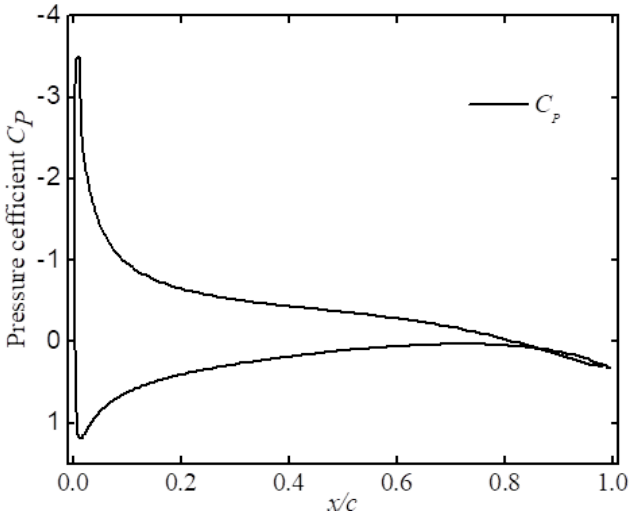

Figure 5 (f): Variation of pressure coefficient on the top edge of the foil at cavitation values 3.5

Lift and drag coefficients time series curves of different σ values 0.8-3.5 are shown in Figure 6 (a-j). It is seen that the time dependent curve is fluctuated around its averaged value because of unsteady nature. The fluctuation gradually decreases with the increasing of cavitation values. The pressure coefficient contours for various cavitation value (0.4-3.5) are shown in Figure 7 (a-f). It is observed that the variation in pressure coefficient relate to the proportion of the volume of voids to volume of solids. These pressure contours show the development of cavity and its magnitude for various cavitation value. The computed result of vapour volume fraction of various σ values appear in Figure 8 (a-f). Very small value of vapour is appeared at σ value 1.5 whereas the full surface is covered with vapour volume at 0.4. As the cavitation values decrease the values of the vapour volume fraction gradually grows to the mid-chord area and vapour region moves to the front of the hydrofoil.

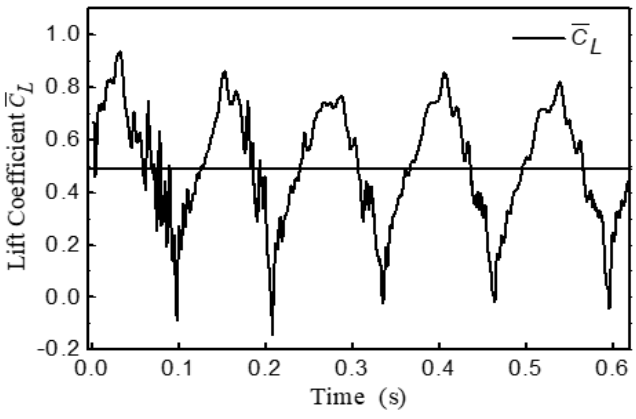

Figure 6(a): Lift coefficient time series for cavitation value 0.8

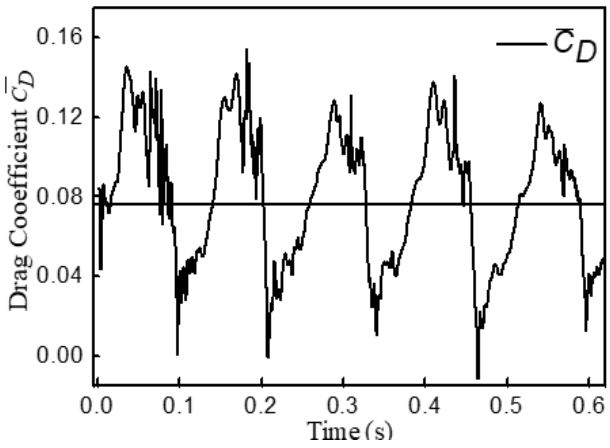

Figure 6(b): Drag coefficient time series for cavitation value 0.8

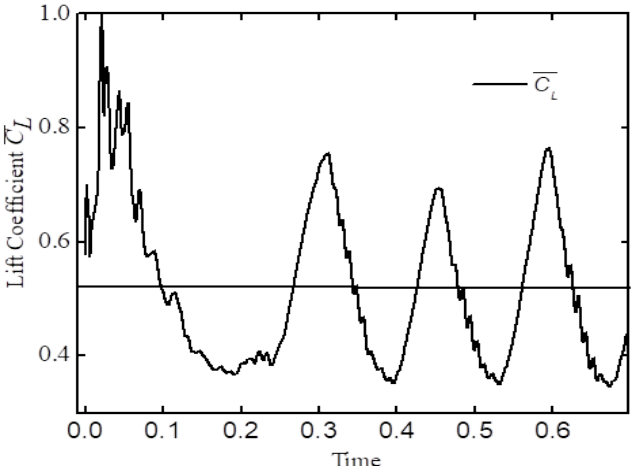

Figure 6(c): Lift coefficient time series for cavitation value 0.9

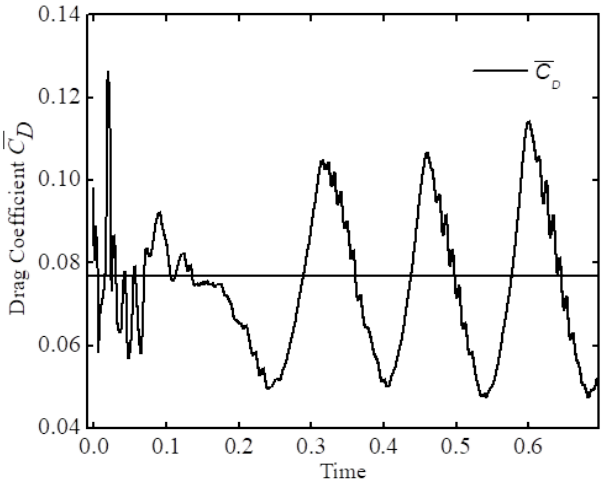

Figure 6(d): Drag coefficient time series for cavitation value 0.9

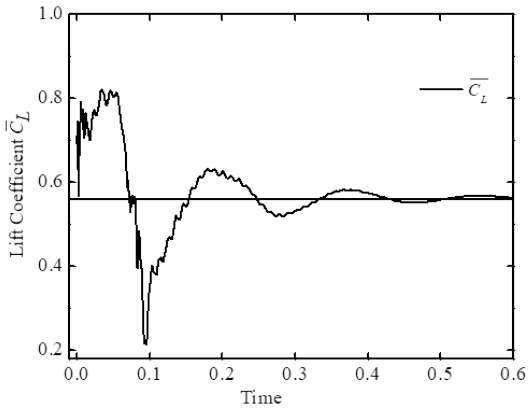

Figure 6(e): Lift coefficient time series for cavitation value 1.0

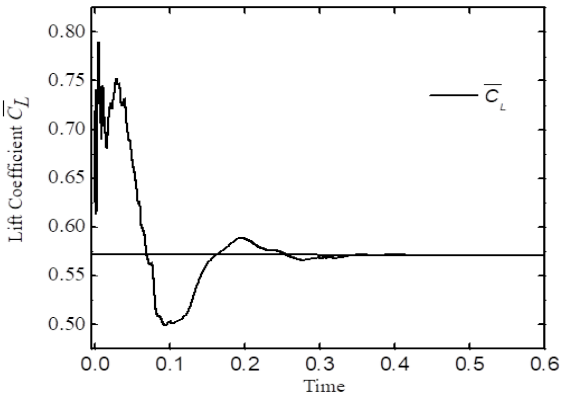

Figure 6(i): Lift coefficient time series for cavitation value 1.5

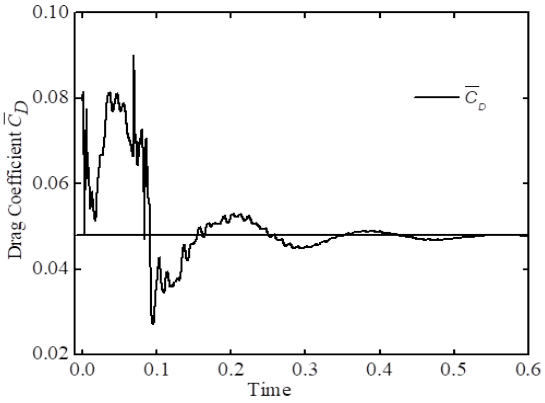

Figure 6(f): Drag coefficient time series for cavitation value 1.0

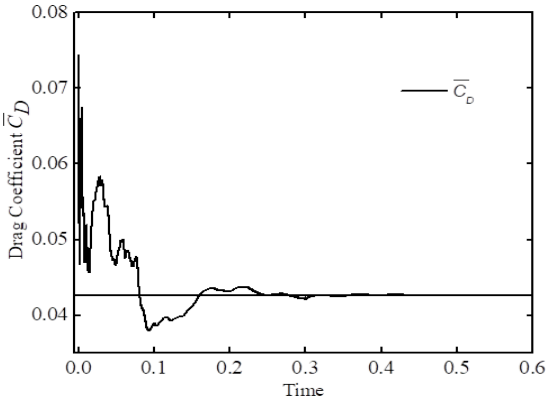

Figure 6(j): Drag coefficient time series for cavitation value 1.5

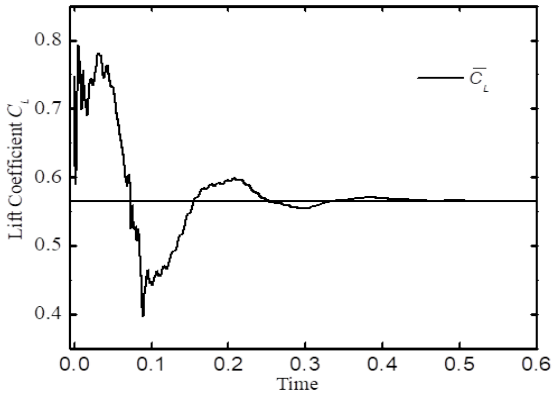

Figure 6(g): Lift coefficient time series for cavitation value 1.1

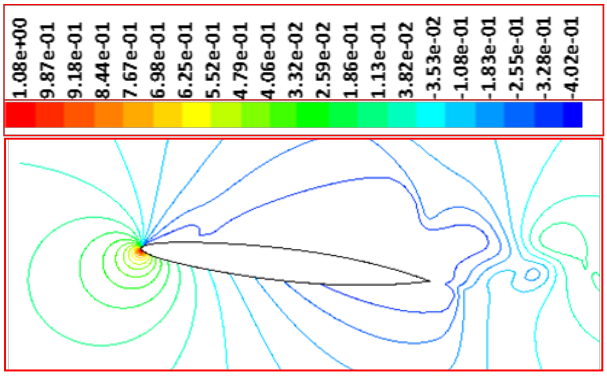

Figure 7(a): Pressure coefficient Contour on foil at cavitation value 0.4

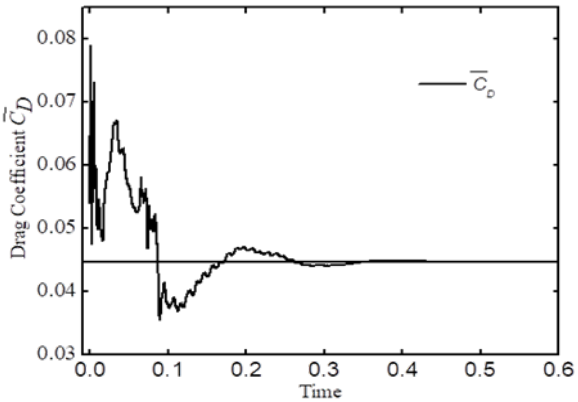

Figure 6(h): Drag coefficient time series for cavitation value 1.1

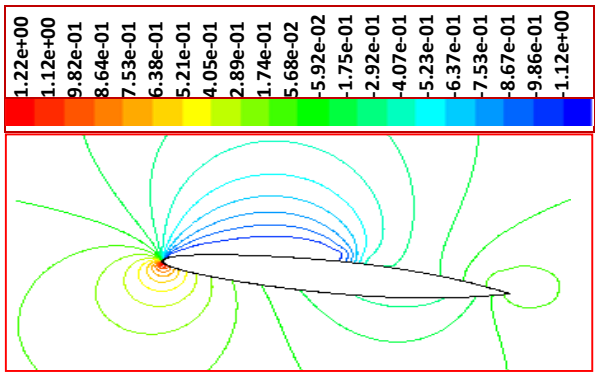

Figure 7(b): Pressure coefficient Contour on foil at cavitation value 0.8

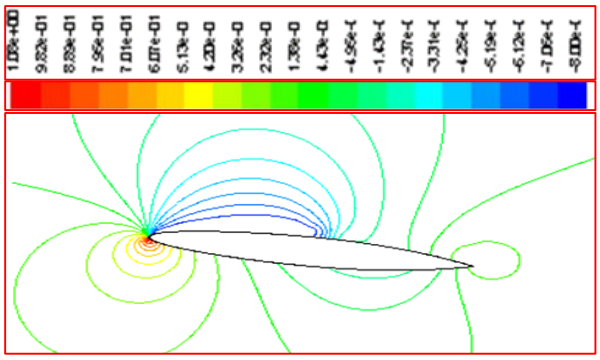

Figure 7(c): Pressure coefficient Contour on foil at cavitation value 0.9

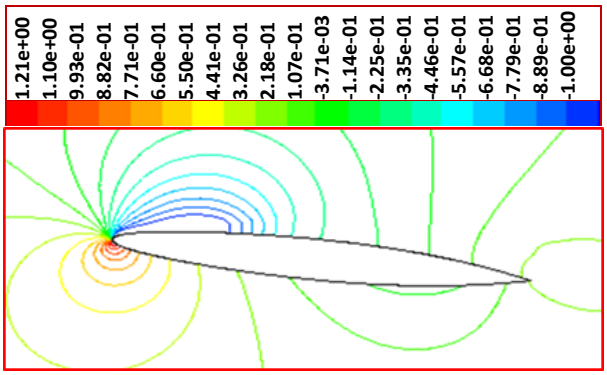

Figure 7(d): Pressure coefficient Contour on foil at cavitation value 1.0

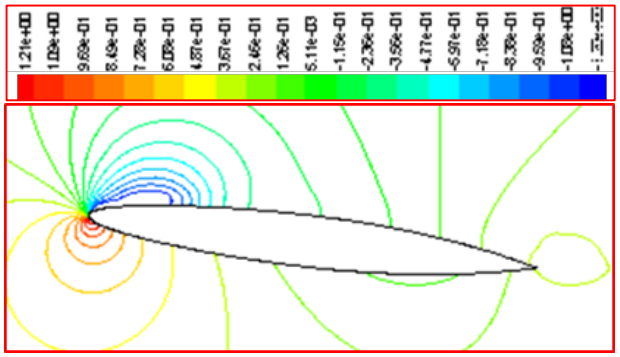

Figure 7(e): Pressure coefficient Contour on foil at cavitation value 1.2

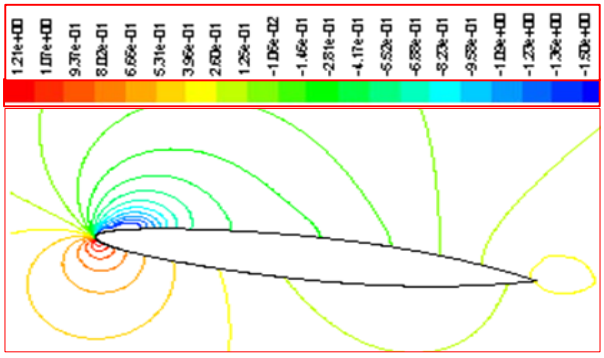

Figure 7(f): Pressure coefficient Contour on foil at cavitation value 1.5

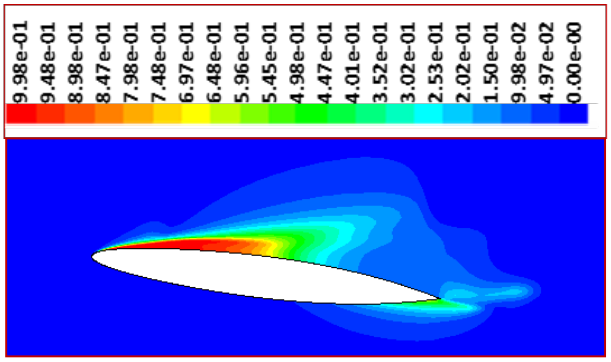

Figure 8(a): Computed vapour volume fraction at cavitation value 0.4

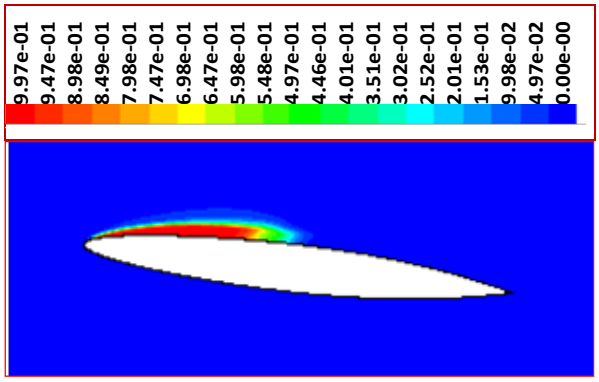

Figure 8(b): Computed vapour volume fraction at cavitation value 0.8

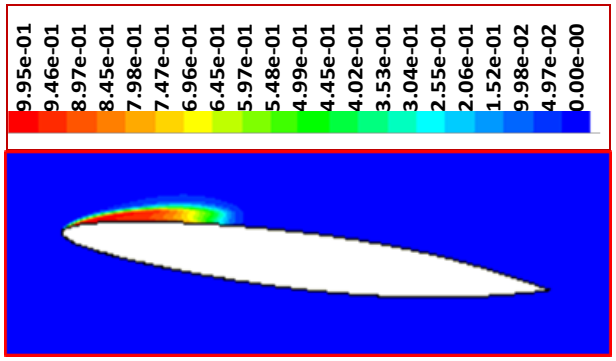

Figure 8(c): Computed vapour volume fraction at cavitation value 0.9

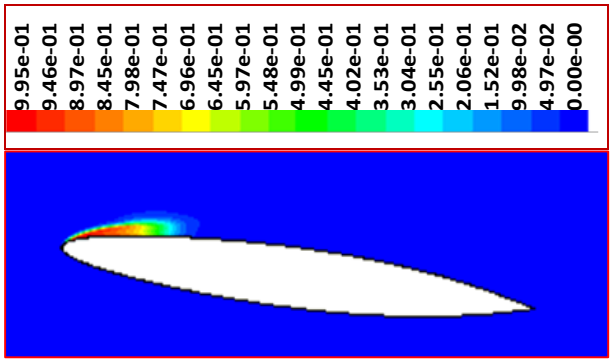

Figure 8(d): Computed vapour volume fraction at cavitation value 1.0

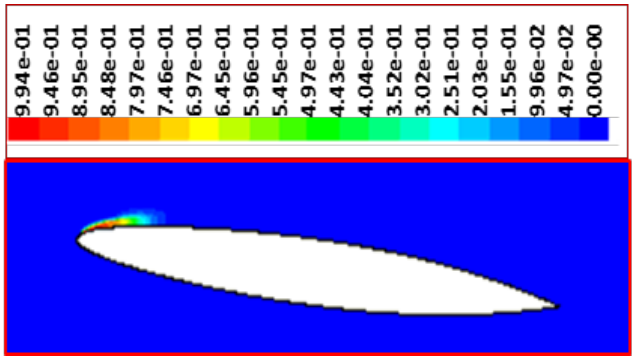

Figure 8(e): Computed vapour volume fraction at cavitation value 1.2

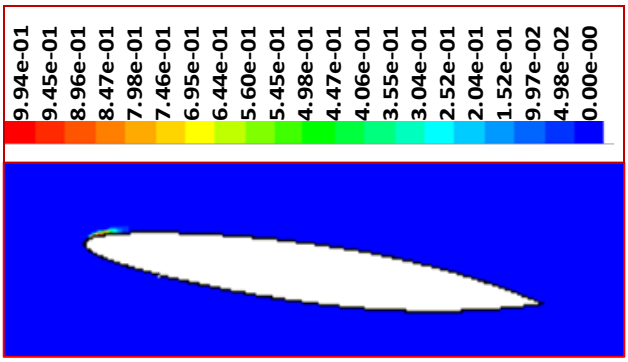

Figure 8(f): Computed vapour volume fraction at cavitation value 1.5

The summary of the time dependent average lift coefficient, drag coefficient, maximum size ($\bar{l}_{max}$) of cavity and maximum width ($\bar{t}_{max}$) of cavity are shown in Table 3 with the various cavitation values respectively. It is seen that the most cavity size and the most cavity width increase with decreasing of cavitation values. A full cavitating flow is developed at σ value 0.4 on the hydrofoil upstream surface.

Table 3
Summary of different cavitation's parameter

Σ	$\bar{l}_{max}$	$\bar{t}_{max}$	$\bar{C}_L$	$\bar{C}_D$
3.5	–	–	0.667	0.0242
1.5	0.098	0.0211	0.582	0.0378
1.2	0.161	0.0329	0.572	0.0425
1.1	0.212	0.0465	0.566	0.0446
1.0	0.251	0.0473	0.560	0.0476
0.9	0.452	0.0772	0.512	0.0783
0.8	0.491	0.0784	0.442	0.0773
0.4	1.001	0.282	0.214	0.0763

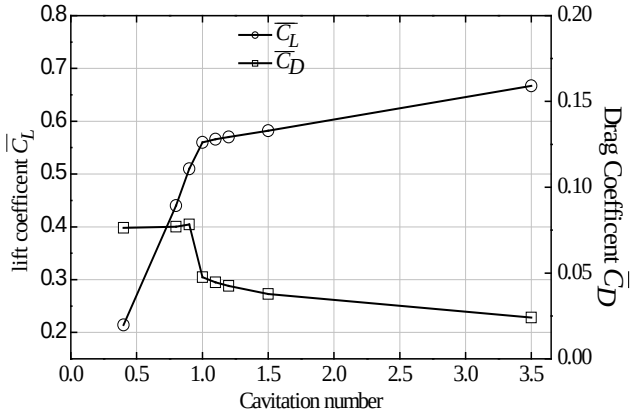

Figure 9: Computed lift and drag coefficient with cavitation values

The computed values of $\bar{C}_L$ and $\bar{C}_D$ together are appeared in Figure 9. It is comprehended that time dependent averaged lift value reduces as decreasing the cavitation number. Moreover, time dependent averaged drag value once almost same at σ value 0.4 to 0.9 and then decline slightly after taking a maximum values at $\sigma = 0.9$ with growing the cavitation number. In addition, it is indicated that the standard deviation become large in a transient range of σ value 0.8 to 1.2.

8. CONCLUTIONS

Finite volume solver associating with implicit RNG k-ε turbulence model and accompanied with two phase flow mixture method is employed to capture irregular cavitating flow all over the CAV2003 hydrofoil. Hydrofoil position angle 7° in flow domain, the maximum values of pressure coefficient in cavitation vicinity increase with the decreasing the σ values, while the cavitation started area retains the unchanged. Cavitation initiation starts at the upstream edge and enlarge along the chord with decreasing the cavitation values. It is observed that at σ value 0.4 the rear surface is entirely covered with fluid vapour and reduce with the increasing the cavitation numbers. Moreover, a transient range of flow is found of σ values from 0.8 to 1.2, where the standard deviation becomes large.

ACKNOWLEDGEMENTS

I would like to expresses my heartfelt thanks and gratitude to MIST authority for giving us the research facilities and all over support throughout this research.

REFERENCES

Brennen C. E. (1995). *Cavitation and bubble dynamics.* Oxford University press, Oxford.

Choudhury D. (1993). *Introduction to the Renormalization Group Method and Turbulence Modeling.* Fluent Inc. Technical Memorandum TM-107.

Dular M., Bacher R., Stoffel B., & Širok B. (2005). Experimental evaluation of numerical simulation of cavitating flow around hydrofoil. *European Journal of Mechanics B/Fluids* 24, 522-538.

Frobenius, M., Schilling, R., Bachert, R., & Stoffel B. (2003, November). Three-dimensional unsteady cavitation effects on a single hydrofoil and in a radial pump – measurements and numerical simulations, Part two: Numerical simulation. Proceedings of the Fifth International Symposium on

Cavitation, Osaka, Japan.

Kawamura T., & Sakuda M. (2003, November). Comparison of bubble and sheet cavitation models for simulation of cavitation flow over a hydrofoil. Fifth International Symposium on Cavitation (Cav2003), Osaka, Japan.

Kothandaraman C. R., & Rudramoorthy R. (2007). *Fluid mechanics and Machinery*. New age international publishers.

Kunz R. F., Boger D. A., Stinebring D. R., Chyczewski T. S., Lindau J. W., Gibeling H. J., Venkateswaran S., Govindan T. R. (2000). *A preconditioned Navier-Stokes method for two-phase flows with application to cavitation prediction*. Computers & Fluids, Vol. 29(8), 850-872.

Karim M., Mostafa N., & Sarker M. M. A. (2010). Numerical study of unsteady flow around a cavitating hydrofoil. *Journal of Naval Architecture and Marine Engineering*, vol. 7, 51-61.

Kubota A., Hiroharu A., & Yamaguchi H. (1992). A new modeling of cavitating flows, a numerical study of unsteady cavitation on a hydrofoil section. *Journal of Fluid Mechanics*, vol, 240, 59–96.

Mortezazadeh M., Katal A., & Javadi K. (2014). Cavitation control on hydrofoil. Proceedings of the International Conference on Heat Transfer and Fluid Flow. Prague, Czech Republic

Mostafa N., Karim M., & Sarker M. M. A. (2016). Numerical Prediction of Unsteady Behavior of Cavitating Flow on Hydrofoils using Bubble Dynamics Cavitation Model. *Journal of Applied fluid Machanic*s, Vol. 9, 1829-1837.

Pouffary B., Fortes-Patela R., & Reboud J. L. (2003, November). Numerical simulation of cavitating flow around a 2D hydrofoil: A barotropic approach. Fifth International Symposium on Cavitation (Cav2003), Osaka, Japan.

Roohi E. & Zahiri A. P. (2012). Numerical simulation of cavitation around a Two-Dimensional Hydrofoil Using VOF Method and LES Turbulence Model. Proceedings of the Eighth International Symposium on Cavitation (CAV 2012). Singapore.

Schnerr G. H. & Sauer J. (2001). Physical and numerical modeling of unsteady cavitation dynamics 4th International Conference on Multiphase Flow, ICMF-2001, New Orleans, USA.

Singhal A. K., Li H., Atahavale M. M., & Jiang Y. (2002). Mathematical basis and validation of the full cavitation model. *Journal of Fluids Engineering*, vol, 124, 617–624.

Stutz B. & Reboud J. L. (2002). Measurements within unsteady cavitation. *Experiments in Fluids*, vol. 29, 545-552.

Yoshinori S., Ichiro N., & Tosshiaki I. (2003). Numerical analysis of unsteady vaporous cavitating flow around a hydrofoil. Fifth International Symposium on Cavitation (Cav2003), Osaka, Japan.

MIJST
MIST International Journal of Science and Technology

Effect of Non-Uniform Soiling on Solar Panel Output and Revenue Analyzed Through a Controlled Experiment by Using a Designed I-V Scanner

Mohammad Didarul Islam[1], Md. Aminul Islam[2], and M. Ryyan Khan[3*]

[1,2]Department of Electrical, Electronic and Communication Engineering, Military Institute of Science and Technology (MIST), Dhaka, Bangladesh
[3]Department of Electrical and Electronic Engineering, East West University (EWU), Dhaka, Bangladesh

emails: *[1]didarulislam357@gmail.com; [2]aminul@eece.mist.ac.bd; and [3]ryyan@ewubd.edu*

ARTICLE INFO

Article History:

Received: 20th March 2022
Revised: 29th June 2022
Accepted: 10th August 2022
Published: 29th December 2022

Keywords:

PV panel
I-V characteristics curve
I-V scanner
bottom edge soiling
non-uniform soiling
performance loss factor
PV power plants

ABSTRACT

Non-uniform soiling drastically decreases the power generation of PV panels. Different events are responsible for the non-uniform soiling on PV panels for example bird droppings, sand storms, or snowfall. In this study, we have achieved multiple-goals for analyzing the effect of non-uniform soiling on a PV module output. We also analyzed the revenue losses due to the non-uniform soiling in a PV power plant. Firstly, for observing the effect of non-uniform soiling an I-V scanner has been designed. Secondly, the designed I-V scanner has been used to observe the changes in the I-V characteristics curve of PV panels due to non-uniform soiling and shading conditions. In this study, we have conducted various controlled experiments by providing different shading conditions on the PV panel and observing the I-V curve changes. A correlation has been done with the various shadowing conditions like the bottom edge soiling condition of PV panels or bird-dropping. In a PV power plant, non-uniform soiling may occur at the edge of PV panels after cleaning intervention. Considering these scenarios, we have done an economic analysis for determining the effect of non-uniform soiling on the revenue of PV power plants. Finally, the relations between the cleaning cycle, performance loss factor, and solar cell area coverage with respect to revenue have been also discussed in this article.

1. INTRODUCTION

When sunlight reaches the glass surface of a solar panel, it passes through the cells that generates electricity. Even if a solar panel is in great condition, its power production will be lowered if sunlight is blocked by any means, such as bird droppings or unevenly accumulated soiling.

Non-uniform soiling on the surface of PV modules affects the I-V characteristics curve of the PV panel and causes hotspots. The temperature of the hotspot is definitely connected to non-uniform soiling, soil band structure, and non-uniform soiling (Lorenzo *et al.*, 2014; Qasem *et al.*, 2014; Sulaiman *et al.*, 2011). As a result, the performance of PV modules varies depending on a variety of conditions, as seen by variations in the I-V characteristics curve. As a result, a transportable I-V scanner can be an important tool for assessing non-uniform shading on solar panels in the field (Pereira *et al.*, 2021).The soil might collect unevenly on the bottom edge of the panels after manual or robotic cleaning. The PV panel's power output will be reduced if the bottom solar cell of any string is covered by non-uniformly collected dirt. The non-uniform soiling effect on a PV module has been shown in previous research to be greater than uniform soiling (Maghami *et al.*, 2016; Molin, 2018; Schill *et al.*, 2015). Soiling accumulates more towards the bottom and, in rare events, at the top of the PV module. Wind and water from dew or rain have a role in this buildup (Lorenzo *et al.*, 2014; Qasem *et al.*, 2014). The collection of dust at the bottom corners of PV modules can cause a significant loss in performance (Pigueiras *et al.*, 2014). The bottom edges of PV modules with lower tilt degrees are more prone to soiling buildup (Gostein *et al.*, 2013; Molin, 2018). The cleaning water flow is frequently insufficient to move these dust particles, resulting in a constant buildup of dust in various forms near the bottom edges of the PV module. The PV module is often installed in portrait or landscape orientation (Cui *et al.*, 2021; Karthick *et al.*, 2020). Rectangular, triangular, and

transverse trapezoidal forms of accumulated soiling band morphologies have been detected at the bottom edge of the PV module (Cui *et al.*, 2021). Partially shading and soiling bands generated at the bottom edges of the PV module restrict incoming sunlight penetration into the solar cells, resulting in a hotspot (AlDowsari *et al.*, 2014). The collection of soiling and bird droppings, which is strongly associated with the soiling accumulating region (Kazmerski *et al.*, 2017), can also cause this localized overheating hotspot of the PV module. Moreover, during the field research, the entire region covered by non-uniformly distributed deposited soiling and bird droppings revealed a high temperature (Cui *et al.*, 2021). These panel hotspots may cause irreversible damage to the PV system. Compared to the non-soiling region, the fixed area covered by accumulated soiling may store some water after cleaning or raining for a long period on the module surface, which can weaken the PV module seal and reduce the PV panel's service life (Cui *et al.*, 2021). Solar farms are planned with row-to-row shadowing panels in mind. Non-uniform shading caused by residual soiling at numerous edges and irregular bird droppings can significantly reduce farm productivity; nevertheless, these factors are not considered in farm designs (Gökdağ *et al.*, 2018; Manganiello *et al.*, 2015). In the PV module, a bypass diode is utilized to reduce the mismatching of the coupled solar cells. Generally, the bypass diode is connected in parallel with a **15** to **20** solar cell series connection to reduce the mismatching due to shadings. PV modules in shade have been the subject of much research since they change the IV shapes (Gallardo-Saavedra & Karlsson, 2018). The majority of economic research analysis in the past has been done with uniform soiling accumulation in consideration. According to an economic study conducted in the Middle East and Africa, the best cleaning cycles for a PV power plant are 5 to 6 days, with a normalized income of **97.5** percent and a loss of **2.5** percent. It shows, that the optimum cleaning cycle in North America is more than 21 days, with revenue losses ranging from **2**% to **5**%. The optimum cleaning cycle in the European region is 17 days, with a revenue loss of more than **2**% (Mithhu et al., 2021). We developed a portable and simple I-V scanner for observing changes in the I-V properties of a PV module under operational conditions in this research. Because all of the components for this I-V scanner is readily accessible on the local market, it will be highly handy, inexpensive, and effective for use in research and rapid system assessment. The goal of this proposed study is to see how partial or non-uniform shade on PV panels owing to soiling on the bottom edge of the modules or random bird droppings affects their performance.

The impact of partial or non-uniform shadowing on various solar cells is investigated in this controlled experiment. Solar cells are chosen at random and covered in various percentages of their surface area to see how shade affects solar panel I-V and power. The relationship between PV module generated power and shade covering the area in (%) is discussed, with soiling and bird-dropping conditions associated. Although this type of partial shade differs from the more well-known row-to-row shading, it should be carefully handled to avoid sub-optimal solar farm operations. However, there seems to be an insufficient study on the relationship between partial shade caused by non-uniformly deposited soiling and bird dropping and PV module power generation efficiency. PV generating output is severely reduced by non-uniform soiling. It has a significant impact on diminishing the income of PV power plants in a PV power plant. Due to the non-uniform soiling of PV panels, even if the cleaning procedure is performed on a regular schedule, power generation may not increase.

In this study, we have done different selective controlled experiments. After the experiments, the evaluation of the economic analysis considering the effect of non-uniform soiling in the different cleaning cycles was also done. The economic analysis of the decreasing factor of the PV panel performance ratio is also addressed at the end of this study.

2. EXPERIMENTAL SETUP

A. *Development* of I-V scanner

We used an n-channel MOSFET (IRF540) as a non-linear variable load in the I-V scanner design. The basic idea is that the I-V curve of the MOSFET will alter depending on the gate-to-source voltage (VGS). The panel now has an electrically adjustable, variable load. The MOSFET's I-V curve will intersect with the PV module's I-V curve at various operating points. As a result, the I-V characteristics curve of the PV module may be captured by measuring a collection of crossing points of MOSFET and PV module I-V curves. When the gate to source voltage (VGS) is increased, When the MOSFET is operated as a non-linear load for the PV panel, the MOSFET's I-V characteristics curve overlaps the PV module's I-V characteristics at particular operating points, as shown in Figure 1, the module I-V characteristics can then be formed automatically by reading these intersecting or operational points.

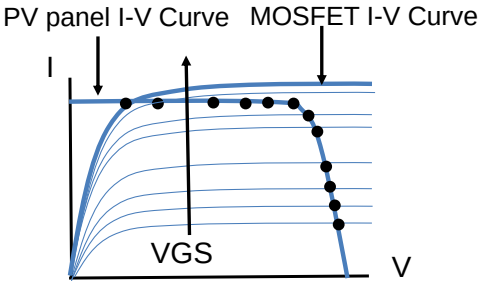

Figure 1: Intersection regions in MOSFET and PV module I-V characteristics curves

B. *Connection of PV Modules*

In our experiment, we used 30 W PV modules from Solarland (model number: SLP030-12). Each PV module is made up of 36 solar cells that are joined in two strings in series. T30-watt PV modules are linked in series to conduct the experiment. Each module has two bypass diodes, helping to make our panel arrangement a four-bypass-diode system. Two PV modules are wired in series in which is shown in Figure 2(a). The system has four strings of solar cells, as shown in Figure 2(b). Partial shadings or non-uniform soiling events such as bird droppings, sand storms, or snowfall events are mitigated with a bypass diode on each string.

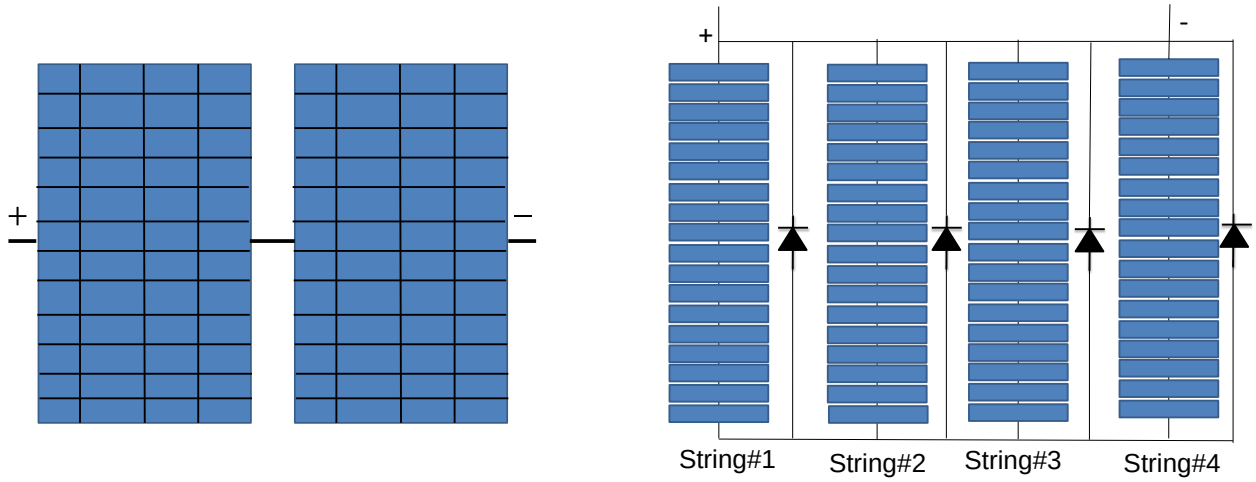

(a) (b)

Figure 2: PV modules, (a) connection, (b) string and bypass diode connections

Table 1
Electrical Parameters of a PV Module

Items	Symbols	Values
Maximum power	P_{max}	30 Watt
Operating voltage	V_{mp}	17.2 Volt
Operating current	I_{mp}	1.74 Ampere
Open circuit voltage	V_{OC}	21.6 Volt
Short circuit current	I_{SC}	1.93 Ampere

C. Schematic Diagram of I-V Scanner

The circuit schematic of the developed I-V scanner is shown in Figure 3. A triangle wave of $5V$ peak is supplied to the MOSFET gate terminal from the triangular wave generator to switch the MOSFET IRF540. The triangle control signal ensures that the panels' I-V are scanned continuously and automatically. The peak voltage of the triangle wave is $5V$, and its period is $2s$. The drain terminal of the MOSFET is linked to the PV module's positive $(+)$ terminal. Between the PV module terminals, a voltage divider with an 8:1 division ratio is utilized. $R2 = 2k$ and $R1 = 16k$ are chosen to ensure this ratio. The main objective of this voltage divider is to keep the data logger input to the Arduino Mega's analog port below 5 volts. Because the series-connected PV module's open-circuit voltage is nearly $40\,V$, using $8{:}1$ voltage divider ratio reduces the PV module's voltage reading to $5\,V$. The center of the divider resistors R1 and R2 is used to measure the voltage of the PV module (V). The obtained value is properly rescaled during the measurement of PV module voltage (V) (multiplied by 9). The MOSFET's source terminal is wired to the grounds through the 1Ω ceramic resistor, which reads the PV module's current (I) through another analog pin on the data logger. To read each operational point, the current (I) and voltage (V) measurements are monitored sequentially.

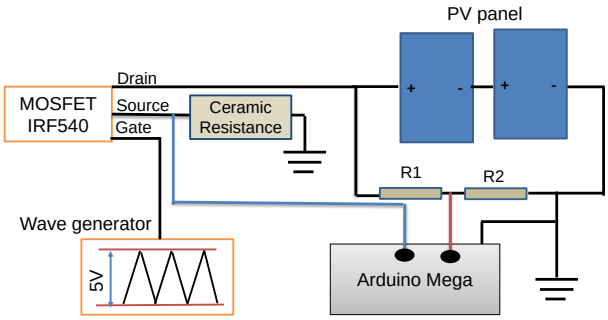

Figure 3: I-V scanner schematic circuit diagram

3. EXPERIMENT RESULTS AND INTERPRETATION

We selectively cover portions of the solar cells in the panel's arrangement to analyze partial shade conditions and measure the I-V and energy outputs. PV module 2 was uncovered, but individual solar cells within PV module 1 were successively covered (partially shaded) in order to study changes in the PV panel setup's I-V characteristics curve. Table II summarizes the results of the trials that were carried out (labeled A, B, C, and D). The solar cell area covers (percent) utilized in the experiment is shown in Figure 4(a). On a cell, a percentage of the area was covered (with black cello tape): 0% (no shade), 25%, 50%, 75%, or 100%. Figure 4(b) depicts experiment B, in which one solar cell is chosen at random (from PV module 1, string 1) to be tested for changes in the I-V curve at 0%, 25%, 50%, 75%, and 100% area-cover circumstances. Experiment C is represented in Figure 4(c), in which one solar cell (from PV module 1, string 1) was randomly covered 25%, 50%, 75%, and 100% and then another random cell (from module 1, string 2) was arbitrarily covered from 25% to 100%. Figure 4(d) depicts experiment D, in which one solar cell is covered to a depth of 25% and another is covered to a depth of 100% both solar cells are inside the same string in experiment D (*i.e.*, in PV module string 1). The experiment of the I-V scanner and a practical illustration of expC2 are described in Table 2. Figure 4(e) and 4(f) represent the experimental setup example which is stated in Table 2.

Table 2
Description of the Conducted Experiments

Experiments	Category	% covered
Experiment A (String1)	expA1	one cell 25% covered
	expA2	another cell 25% covered
Experiment B (String1, One PV Cell selectively)	expB1	Not covered
	expB2	25% covered
	expB3	50% covered
	expB4	75% covered
	expB5	100% covered
Experiment C (String 1, randomly one cell 25% fixed cover, String 2 one cell selectively)	expC1	25% covered
	expC2	50% covered
	expC3	75% covered
	expC4	100% covered
Experiment D (String 1, randomly one cell 25% fixed cover, and another PV cell of string1)	expD1	25% cover
	expD2	50% cover
	expD3	75% cover
	expD4	100% cover

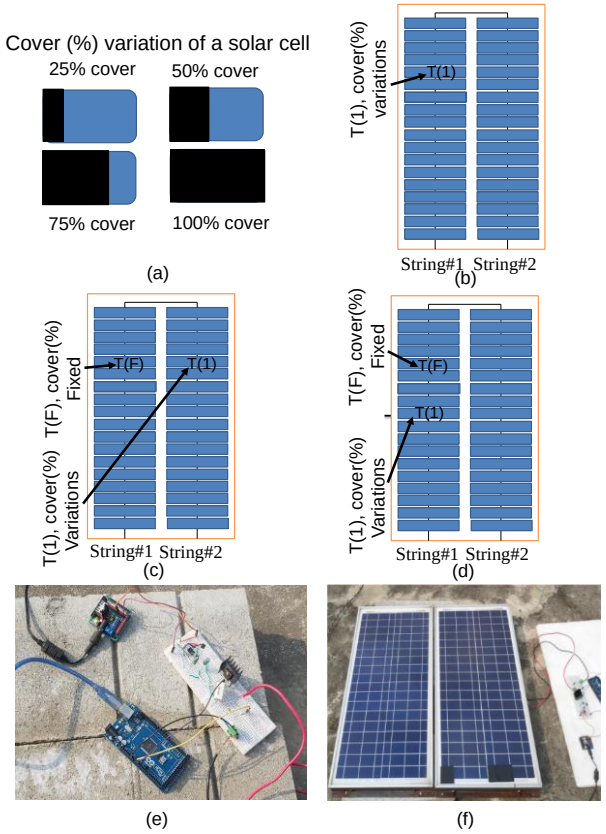

Figure 4: (a) The variance in each solar cell cover (percentage) has been defined. The following are examples of different experiment conditions: (b) experiment B: string 1 solar cell cover (percent) variations, (c) experiment C: string1 fixed **25**% cover, string 2 individual cell cover (percent) variations, (d) experiment D: string1 fixed **25**% cover, string1 another cell cover (percent) variations (e) I-V scanner setup for testing. (f) An example of a conducted experiment, such as table-II's expC2

We controlled shade conditions that were similar to realistic non-uniform shading scenarios (sandstorms, snowfall, bird droppings) during the experiment. The level of non-uniformity in different soiling scenarios are unpredictable. To eliminate this uncertainty, we conducted a controlled experiment in which the area of a certain solar cell was shaded at various percentages. With the use of black cello tape covering, we demonstrated what would happen if non-uniform soiling shaded the panel in various percentages of its area. The variations in power output caused by non-uniform soiling will be similar to those seen in our controlled experiment.

A. Normalized Data Analysis

During the infield experiments, we observed that the irradiance of sunlight varies from one I-V measurement to the next. This made it difficult to compare the I-V characteristics from the various experiments. Therefore, we have introduced the normalization technique, where, the current and voltage readings of an I-V are normalized to its corresponding short circuit current and open circuit voltage. All the I-V curves in Figure 5 discussed in the following have been normalized.

The normalized I-V curves from experiment A are shown in Figure 5(a). The I-V characteristics are overlapping in this case. Similarly, the P-V curves of two trials, expA1 and expA2, overlap in Figure 5(b). The overlapping curves in Figure 5(a) and 5(b) illustrate that, regardless of the position of the cell, we should expect the same relative output reduction because of the same shadow coverage. To retain have same short circuit current, the bypass diode is activated at lower voltages. The I-V characteristics are overlapping in this case. Similarly, the P-V curves of two trials, expA1 and expA2, overlap in Figure 5(b). The normalized I-V curve of experiment B is shown in Figure 5(c), where each solar cell in string1 has a 25%, 50%, 75%, and 100% cover. The overlapping curves in Figure 5(a) and 5(b) illustrate that, regardless of the position of the cell, we should expect the same relative output reduction because of the same shadow coverage. We found the maximum power production under a 0% cover situation as shown in Figure 5(d). The normalized output power for the PV cell shading area covered ranging from 25% to 100% is shown in Figure 5(d). When the coverage is increased from 0% to 25% to 50%, the maximum power (Pmax) is seen to decrease. Because the bypass diode is activated at the maximum power point, the Pmax measurement does not change for 50% to 100% shading.

The I-V curve characteristics for all of the examples of experiment C are shown in Figure 5(e) (string 1 solar cell fixed 25% cover, and another cell coverage varied from 25% to 50%, 75%, and 100%). As a result, string 1 bypass activated at 25% current in all scenarios. It appears that the coverage of the same amount of area of two strings in exp-C1 (25% + 25% coverage) has the same impact as in exp-B with 25% shadow. The string 2 bypass diode activated again for 50 percent, 75 percent, and 100 percent coverage of the solar cell of string 2 in exp-C2, exp-C3, and exp-C4, respectively. Because string 1 is likewise 25% shaded, the bypass diode triggered MPP will have a 25% lower Pmax, as seen in Figure 5(f). The I-V

and P-V characteristics of experiment D are depicted in Figure 5(g) and 5(h). One cell in this experiment is shaded 25%, while shading on another PV cell in the same string is changed. The impact of shading in two cells is dominated by the increased shadow coverage due to the fact that they are both under the same bypass diode. As a result, experiment D exhibits the same patterns as experiment B.

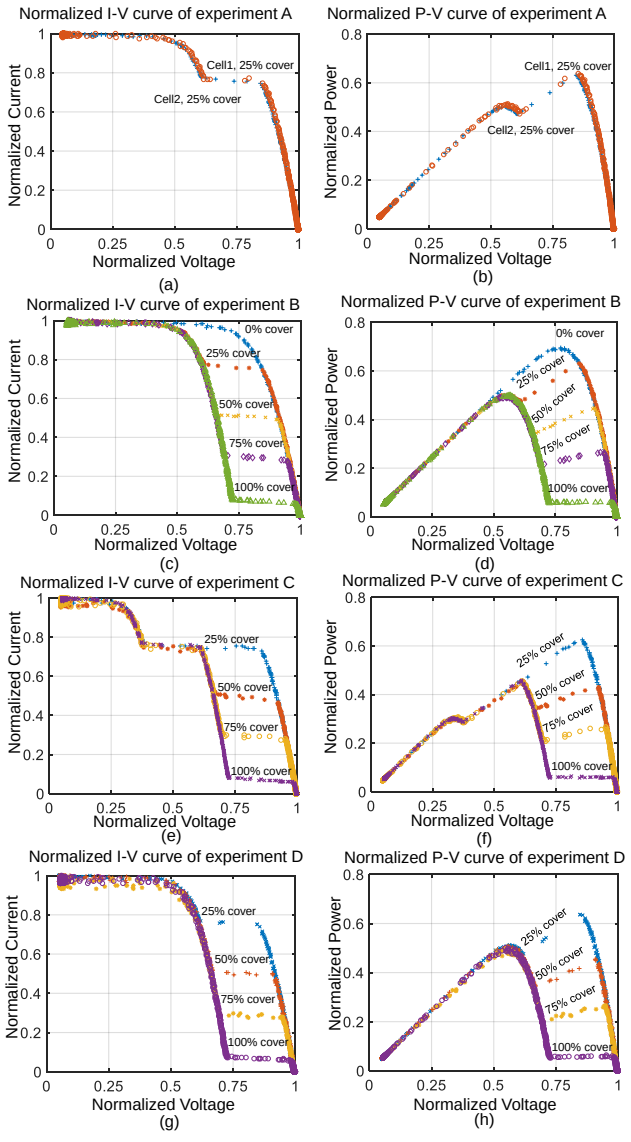

Figure 5: (a) I-V curve of experiment A (a cell of string 1, **25**% cover; another cell of string 1, **25**% cover), (b) P-V curve of experiment A, (c) I-V curve of experiment B (string 1 cell **0**%, **25**%, **50**%, **75**%, and **100**% cover variation), (d) P-V curve of experiment B, (e) I-V curve of experiment C (string 1, a cell with a **25**% fixed cover, string 2 another randomly selected cell, **0**%, **25**%, **50**%, **75**%, and **100**% cover variation), (f) P-V curve of experiment C, (g) I-V curve of experiment D (string 1, a cell with a **25**% fixed cover, string 1 another randomly selected cell, **0**%, **25**%, **50**%, **75**%, and **100**% cover variation), (h) P-V curve of experiment D

B. Experiment B, C, and D MPP Comparison

The maximum power ($P_{\max}$) of studies B, C, and D are compared in Figure 6. Solar cell area coverage changes as follows for experiment B: 0%, 25%, 50%, 75%, and 100% from PV module1 string 1. The PV panel's power is at its greatest when there is no covering. We found that the power decreased monotonically as the proportion of shadowing on the solar cell increased up to 50%.

$P_{\max}$ remains unchanged for cell shading of 50% or more. This is because, in high-shading conditions, the shaded string is discarded due to the bypass diode activation. The MPP peak changes to a lower voltage owing to the activation of bypass diodes, as seen in Figure 5 (P-V plots).

Because of shading on a single string, experiments B and D are nearly identical, as discussed in the preceding subsection.

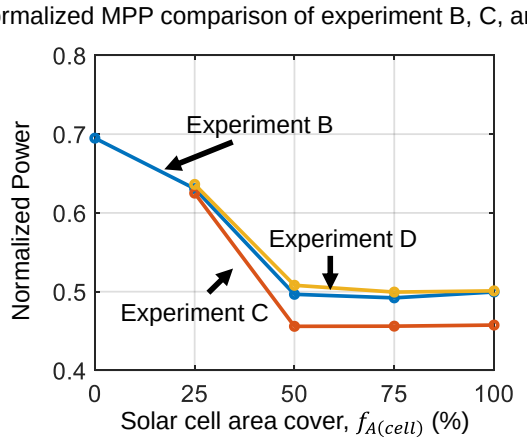

Figure 6: Maximum power (P_{max}) comparison of experiments B, C, and D

However, we can observe that its $P_{\max}$ saturates at a lower value (for shading 50%) in the figure for experiment C. After the MPP is limited by the bypass diode in this scenario (i.e., exp-C), the current at the second string is also reduced by 25% shading. As a result, the normalized power for the shade of 50% or more in experiment C is lower than in experiments B or D.

C. Multiple Soiling Band Condition

There are three types of soiling bands along the bottom border of a solar panel, according to the literature: triangular, rectangular, and transverse trapezoid. The triangular soiling band shape seen in Figure 7(a) mostly covers a cell from string 1 and partially covers a cell from string 2.

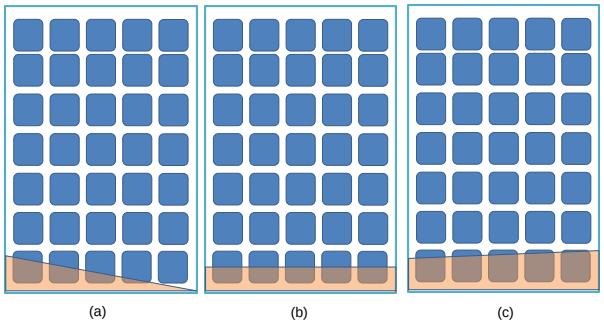

Figure 7: Soiling band schematic diagram (a) triangular, (b) rectangular, (c) transverse trapezoidal schematic diagram on PV panel.

The rectangular soiling band form is shown in Figure 7(b) covers the bottom border of both cells of the two strings. A transverse trapezoidal soiling band is seen in Figure 7(c). Even after cleaning, such soiling bands can linger on panels, especially if machine-cleaning is utilized. All three options are applicable to our experiment C. As previously stated, even partial shading of a few cells can drastically reduce the system's output, therefore the success of cleaning should be regularly reevaluated if such soiling bands remain.

Bird-dropping has the potential to shade various cells on the panel at random (Sisodia & Mathur, 2019). The bird-dropping in PV panels in distinct strings in different regions of a PV panel. All of our experimental results can be linked to the effects of low to high bird dropping rates on panel output. A cumulative soiling and bird-dropping scenario significantly reduce production; the appropriate operational output will then be lost unless a thorough cleaning intervention is performed.

4. REVENUE ANALYSIS FOR NON-UNIFORM SOILING

In case of uniform soiling on modules, the performance ratio, PR (unclean to clean panel output ratio) decreases daily due to dust accumulation. After a cleaning intervention, PR immediately resets to unity. The temporal characteristics of PR is saw-tooth-like with periodic cleaning-this is shown in Figure 8(a). Clearly, PR is not always equal to 1, this indicates unavoidable energy loss for any cleaning cycle t_C (> 1). The cleaning cycle and its costs are chosen to maximize revenue. The revenue under uniform soiling with a cleaning cycle of t_C can be written as shown in Equation (1).

$$\text{Rev}_\text{U} = RE_0\left[1 - \frac{1}{2}at_C - \frac{C}{RE_0}\frac{1}{t_C}\right] \quad (1)$$

Here, R is the tariff rate, a is the soiling rate, E_0 is the mean daily rated (*i.e.*, clean panel) energy output, C is the cleaning cost, and t_C is the cleaning cycle.

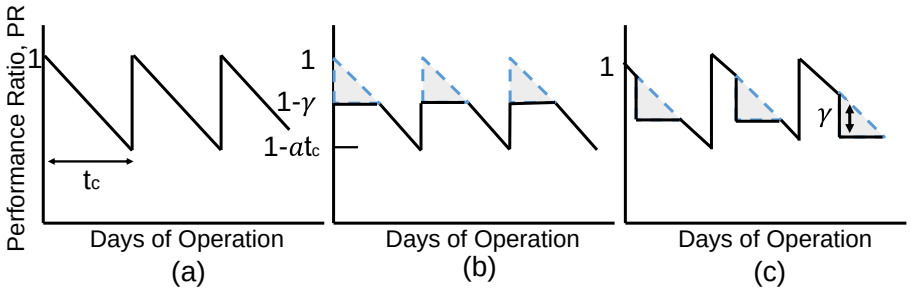

Figure 8: Performance ratio versus cleaning cycle (a) without non-uniform soiling, (b) with non-uniform soiling conditions (edge soiling due to machine or manual cleaning), and (c) with non-uniform soiling conditions (bird-droppings, snowfall, sand storm)

Consider a scenario where there is always some accumulated dust (*e.g.*, as shown in Figure 7(b)) at the edges. In this case, after inefficient machine cleaning, the PR does not return to unity, see Figure 8(b). We define this residual loss through the "Performance Loss (PL) Factor", γ. With time, the module will continuously accumulate uniform dust with no reduction in PR until the rest of the module area reaches soiling-loss comparable to that at the edges. Therefore, after each inefficient cleaning cycle, the PR reaches $(1-\gamma)$. The additional loss per cycle is marked are the shaded triangular area. The corresponding mean daily loss in PR related to this triangular area is $(\gamma^2/2a)$. A similar loss may occur due to a sudden soiling band formation due to wind, or bird dropping (see Figure 8(c)).

For the uniform soiling, the PR can decrease by $\sim at_C$ at the end of a cleaning cycle. Therefore, if $\gamma > at_C$, the uniform soiling on the panel area never reaches the edge-soiling loss of γ. In such a case, the performance ratio always remains at $PR = \gamma$ showing no effect or signature of cleaning. Finally, the revenue under combined uniform and non-uniform soiling with the cleaning cycle of t_C can be written as:

$$\text{Rev}_\text{NU} = \begin{cases} RE_0\left[1 - \frac{1}{2}at_C - \frac{C}{RE_0}\frac{1}{t_C} - \frac{\gamma^2}{2a}\right]; & \gamma < at_C \\ RE_0\left(1 - \gamma - \frac{C}{RE_0}\frac{1}{t_C}\right) & ;\gamma \geq at_C \end{cases} \quad (2)$$

The term (C/RE_0t_C) accounts for the loss in revenue due to panel cleaning at each cleaning cycle.

Finally, the performance loss factor γ can be related to the solar cell area cover fraction ($f_{A(cell)}$) from Figure 6. The fractional loss in 'Normalized power' with increasing $f_{A(cell)}$ is equivalent to γ. Therefore, a second-order polynomial fit gives:

$$f_{A(cell)} = -5\gamma^2 + 3.2\gamma \quad (3)$$

Equations (2) and (3) relate the revenue (Rev_NU) to the solar cell area cover fraction ($f_{A(cell)}$) due to non-uniform soiling in presence of constant uniform soiling (rate: a).

Figure 9 and 10 show the normalized revenue and the revenue is the presence of uniform non-uniform soiling. Normalized revenue is the dust-affected revenue normalized to the soiling-free revenue of a solar farm. The revenue, of course, considers the reduction in cash-inflow due to costs incurred by periodic panel cleaning. In our calculations, we assume values relevant to South Asia: $R = 0.0895$ USD/kWh , $E_0 = 0.1123$ kWh/day , $C = 0.03$ USD/kWh/Wp , $a = 0.8\%/day$ (Jahangir *et al.*, 2020; Mithhu *et al.*, 2021).

With, $f_{A(cell)} = 0$ (i.e., $\gamma = 0$), there is no non-uniform soiling. However, as shown in Figure 9, due to natural

uniform soil accumulation the normalized revenue f_R is 97%, 94%, and 88% for cleaning cycles of $t_C = 7$, 15, and 30 days, respectively. This means we will lose 3%, 6%, and 12% of the rated clean-panel revenue during these cleaning cycles, it is impossible to reduce the revenue loss to zero in presence of soiling. The corresponding revenue values are shown in Figure 10. With increased non-uniform soiling (*e.g.*, due to inefficient cleaning), $f_{A(cell)} > 0$ and the revenue decreases further (as explained in Equation (2)).

The non-uniform soiling, i.e., $f_{A(cell)} > 0$ can have a strong reduction in revenue. Interestingly, for $f_{A(cell)} > 25\%$ cleaning cycles of 7 and 15 days result in similarly reduced revenues, the loss is $> 10\%$. This extraordinarily high loss will persist unless the panels and their edges are appropriately cleaned. In the unlikely case when $f_{A(cell)} > 45\%$, $t_C = 7$, 15, or 30 days result in the same $> 20\%$ loss in revenue.

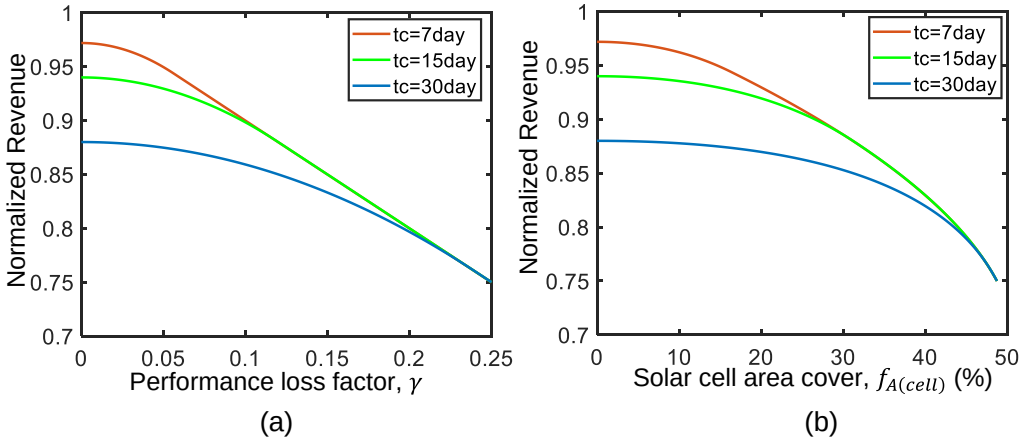

Figure 9: Relationship between (a) normalized revenue and decreasing factor of performance ratio (γ) (b) normalized revenue and covered area (%) due to non-uniform soiling

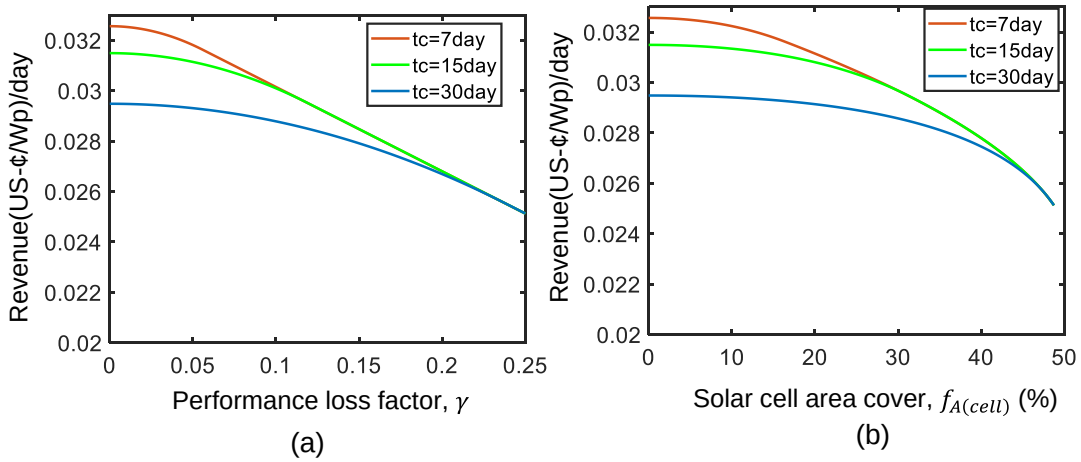

Figure 10: Relationship between (a) revenue and decreasing factor of performance ratio (γ) (b) normalized revenue and covered area (%) due to non-uniform soiling.

5. CONCLUSION

In this work, we have designed an I-V scanner for observing the I-V changes. Various experiment has been done by providing various shadowing conditions. These shading conditions correlated with different real-life scenarios like bird-dropping. After that, we modelled a numerical analysis for evaluating economic analysis where the non-uniform soiling conditions are considered. The relationship of revenue between performance loss factor and area cover (%) due to non-uniform soiling is also shown in this study.

During the experiment, we have found the I-V characteristics curve of a PV panel changes abruptly with respect to the different shadowing conditions. In a string of a PV panel when around 50% shadow occurred then the bypass diode of that string is triggered therefore then the output power does not change even if the area coverage increases. We have found that the cleaning cycle has a significant influence on the non-uniform soiling effect. In non-uniform soiling conditions for 7 days cleaning cycle, the normalized revenue becomes 97%, and for the cleaning cycle of 15 and 30 days, the revenue becomes 94% and 88% respectively. Surprisingly for cleaning cycles 7 and 15 days, if the area of non-uniform soiling on a solar cell is greater than 25% then the decrease of revenue for both cleaning cycle become the same. Therefore, in these rated cleaning cycles it is impossible to avoid the effect of non-uniform soiling on the PV panels. From the study, we found the lower the cleaning cycle the lower the loss due to non-uniform soiling. Non-uniform soiling on PV panels can reduce the power generation of a PV panel drastically. The effect of non-uniform soiling cannot be mitigated until the

cleaning intervention is performed. To ensure maximum revenue, engineers designing PV power plants should take into account the condition of non-uniform soiling in PV panels on different cleaning cycles.

ACKNOWLEDGEMENTS

Authors would like to express their gratitude to the department of EECE, MIST, Dhaka, Bangladesh; and department of EEE, EWU, Dhaka, Bangladesh. They are also grateful to the Editors and Reviewers of MIJST for valuable suggestions and comments in improving the contents of the article.

REFERENCES

AlDowsari, A., Bkayrat, R., AlZain, H., & Shahin, T. (2014). Best practices for mitigating soiling risk on PV power plants. *2014 Saudi Arabia Smart Grid Conference (SASG)*, 1–6. https://doi.org/10.1109/SASG.2014.7274291

Cui, Y.-Q., Xiao, J.-H., Xiang, J.-L., & Sun, J.-H. (2021). Characterization of Soiling Bands on the Bottom Edges of PV Modules. *Frontiers in Energy Research*, *9*, 145. https://doi.org/10.3389/fenrg.2021.665411

Gallardo-Saavedra, S., & Karlsson, B. (2018). Simulation, validation and analysis of shading effects on a PV system. *Solar Energy*, *170*, 828–839. https://doi.org/10.1016/j.solener.2018.06.035

Gökdağ, M., Akbaba, M., & Gulbudak, O. (2018). Switched-capacitor converter for PV modules under partial shading and mismatch conditions. *Solar Energy*, *170*, 723–731. https://doi.org/10.1016/j.solener.2018.06.010

Gostein, M., Littmann, B., Caron, J., & Dunn, L. (2013). *Comparing PV power plant soiling measurements extracted from PV module irradiance and power measurements*. 3004–3009. https://doi.org/10.1109/PVSC.2013.6745094

Jahangir, J. B., Al-Mahmud, Md., Sarker Shakir, Md. S., Hasan Mithhu, Md. M., Rima, T. A., Sajjad, R. N., & Khan, M. R. (2020). Prediction of Yield, Soiling Loss, and Cleaning Cycle: A Case Study in South Asian Highly Construction-Active Urban Zone. *2020 47th IEEE Photovoltaic Specialists Conference (PVSC)*, 1371–1374. https://doi.org/10.1109/PVSC45281.2020.9300606

Karthick, A., Manokar Athikesavan, M., Pasupathi, M. K., Manoj Kumar, N., Chopra, S. S., & Ghosh, A. (2020). Investigation of Inorganic Phase Change Material for a Semi-Transparent Photovoltaic (STPV) Module. *Energies*, *13*(14), 3582. https://doi.org/10.3390/en13143582

Kazmerski, L. L., Diniz, A. S. A. C., Braga, D. S., Maia, C. B., Viana, M. M., Costa, S. C., Brito, P. P., Campos, C. D., de Morais Hanriot, S., & de Oliveira Cruz, L. R. (2017). Interrelationships Among Non-Uniform Soiling Distributions and PV Module Performance Parameters, Climate Conditions, and Soiling Particle and Module Surface Properties. *2017 IEEE 44th Photovoltaic Specialist Conference (PVSC)*, 2307–2311. https://doi.org/10.1109/PVSC.2017.8366584

Lorenzo, E., Moretón, R., & Luque, I. (2014). Dust effects on PV array performance: In-field observations with non-uniform patterns: Dust effects on PV array performance. *Progress in Photovoltaics: Research and Applications*, *22*(6), 666–670. https://doi.org/10.1002/pip.2348

Maghami, M. R., Hizam, H., Gomes, C., Radzi, M. A., Rezadad, M. I., & Hajighorbani, S. (2016). Power loss due to soiling on solar panel: A review. *Renewable and Sustainable Energy Reviews*, *59*, 1307–1316. https://doi.org/10.1016/j.rser.2016.01.044

Manganiello, P., Balato, M., & Vitelli, M. (2015). A Survey on Mismatching and Aging of PV Modules: The Closed Loop. *IEEE Transactions on Industrial Electronics*, *62*(11), 7276–7286. https://doi.org/10.1109/TIE.2015.2418731

Mithhu, Md. M. H., Rima, T. A., & Khan, M. R. (2021). Global analysis of optimal cleaning cycle and profit of soiling affected solar panels. *Applied Energy*, *285*, 116436. https://doi.org/10.1016/j.apenergy.2021.116436

Molin, M. D. (2018). Experimental Analysis of the Impact of Soiling on Photovoltaic Modules Performance. *Master's Thesis. Milan: Politecnico Di Milano*.

Pereira, T. A., Schmitz, L., dos Santos, W. M., Martins, D. C., & Coelho, R. F. (2021). Design of a Portable Photovoltaic I–V Curve Tracer Based on the DC–DC Converter Method. *IEEE Journal of Photovoltaics*, *11*(2), 552–560. https://doi.org/10.1109/JPHOTOV.2021.3049903

Pigueiras, E., Moretón, R., & Luque, I. (2014). Dust effects on PV array performance: In-field observations with non-uniform patterns. *Progress in Photovoltaics: Research and Applications*, *22*. https://doi.org/10.1002/pip.2348

Qasem, H., Betts, T., Müllejans, H., Albusairi, H., & Gottschalg, R. (2014). *Dust-induced shading on photovoltaic modules*. https://doi.org/10.1002/PIP.2230

Schill, C., Brachmann, S., & Koehl, M. (2015). Impact of soiling on IV-curves and efficiency of PV-modules. *Solar Energy*, *112*, 259–262. https://doi.org/10.1016/j.solener.2014.12.003

Sisodia, A., & Mathur, R. (2019). Impact of bird dropping deposition on solar photovoltaic module performance: A systematic study in Western Rajasthan. *Environmental Science and Pollution Research*, *26*. https://doi.org/10.1007/s11356-019-06100-2

Sulaiman, S. A., Hussain, H. H., Leh, N. S. H. N., & Razali, M. S. I. (2011). Effects of Dust on the Performance of PV Panels. *International Journal of Mechanical and Mechatronics Engineering*, *5*(10), 2021–2026. https://publications.waset.org/10305/effects-of-dust-on-the-performance-of-pv-panels

MIJST
MIST International Journal of Science and Technology

Cost and Reliability Analysis of a Hybrid Renewable Energy System - A Case Study on an Administration Building

Wenyuan Sun[1*], Cong Tian[2], and Yingai Jin[3]

State Key Laboratory of Automotive Simulation and Control, Jilin University, Changchun 130022, China

emails: *[*1]sunwy20@mails.jlu.edu.cn; [2]1452370936@qq.com; and [3]jinya@jlu.edu.cn*

ARTICLE INFO

Article History:

Received: 12th September 2022
Revised: 20th November 2022
Accepted: 24th November 2022
Published: 29th Decemebr 2022

Keywords:

Hybrid renewable energy systems
Wind
Solar
Hydrogen

ABSTRACT

Renewable energy generation systems have been developing rapidly in recent years. However, renewable energy systems have the problem of large power abandonment. In this paper, two different hybrid renewable energy systems (HRESs) have been designed for satisfying the electrical demand of a large office building in Changchun. A comparative analysis between two strategies is also presented to find out the best capacity for the proposed HRESs. The first HRES consists of solar PV, wind turbine, battery storage system (PV-WT-BATT) and load demand of 5,000 kWh/d. The second consists of solar PV, wind turbine, battery storage system, electrolyzer, hydrogen tank (PV-WT-BATT-EL-HT) and load demand of 5,000 kWh/d. The two HRESs are optimized for Net Present Cost (NPC), Levelized Cost of Energy (COE), Operating Cost and the rate of excess electricity minimization. The techno-economic analysis of the two HRESs is conducted using the HOMER Pro software platform. This study provides a complete guideline for determining the optimum component capacity to ensure costing estimation for the optimized performance of the two HRESs.

1. INTRODUCTION

Adequate energy supply has always been a crucial issue and is considered one of the prerequisites for a country's economic growth and development. Reducing fossil fuel consumption through utilizing renewable energy sources can offer an effective mitigation option to enhance energy security and reduce fossil fuel dependance (Byrne *et al.*, 1998; Heidari *et al.*, 2019; Shirmohammadi *et al.*, 2018). Taking this reality into account, the use of renewable energy sources, can be considered as an alternative solution to overcome energy deficiency for achieving sustainable development and economic prosperity (Armin *et al.*, 2019; Aslani *et al.*, 2018; Khatibi *et al.*, 2018; Khatibi *et al.*, 2018; Razmjoo *et al.*, 2019).

There is no doubt that solar and wind power are most suitable clean energy sources, and according to published statistics, the impact on energy services is growing (Bakhtiar *et al.*, 2020; Hosseini *et al.*, 2017; Mohammadi *et al.*, 2018). In addition, solar and wind have considerable potential to supply a significant portion of the world's energy demand. Furthermore, latest breakthroughs in solar and wind technology and related areas have increased the efficiency of power generation (Lotfi *et al.*, 2013; Soltani *et al.*, 2017). However, due to the intermittency and design constraints, the design and application of hybrid renewable energy systems are still challenging (Das *et al.*, 2019).

Hydrogen energy also has great development potential, proton exchange membrane (PEM) hydrogen production technology has a small footprint, low energy consumption, high flexibility, and good compatibility with wind power and photovoltaic, which are volatile and stochastic, so it has more application advantages and cost reduction potential in many scenarios. At present, this technology has not been commercialized on a large scale in China, but there are already many megawatt-scale applications in Europe. Cummins company has many large-scale commercial projects in Canada, the U.S. and Europe, including the 20 *MW* PEM electrolytic water project under construction in Canada.

With the continuous development, the price of equipment will drop as the proportion of localization becomes higher in the future. From the perspective of future trends, the cost of renewable energy will continue to decline. With the policy support of the government and the continuous exploration of enterprises in the hydrogen energy industry chain, the green hydrogen energy business model will become mature and more large-scale, which will bring significant room for equipment cost reduction. According to the research of major international energy institutions, green hydrogen energy will be economical and equal to the

cost of fossil energy hydrogen production by around 2030.

In recent years, there has been a great deal of research into the design, the reliability and optimization of independent HRESs including the wind turbine-diesel generator (WT-DG), PV-DG, WT-PV-DG, and PV-Fuel cell (PV-F) and these systems with battery storages. A single energy independent system, i.e., wind system, solar system, or DG system cannot provide continuous power supply due to their intermittency (Yang *et al.*, 2008). Therefore, Energy Storage Systems (ESS) are considered crucial for the full adoption of HRESs. The integration of the solar and wind generations with storage resources can thus effectively lead to a flexible and reliable design for an HRES. As a result, it is necessary to develop a well-designed model for cost-effective and reliable operation of an HRESs.

The wind power generation had been compared in South Asian countries (Khan *et al.*, 2012). The analysis includes current generation capacity by fuel type, government initiatives and wind energy policies. The study shows that India has a clear lead in wind energy utilization compared to the other two countries, Bangladesh, and Pakistan. The main obstacle to wind power is the lack of clear policy and government initiatives. The combination of independent solar PV with DG was studied (Kolhe *et al.*, 2002), They reported that solar PV was more technically and economically efficient and gave an output of 68 kWh/day, making the solar PV market competitive. The performance of a hybrid PV-WT had been optimized on the HOMER software platform to replace DG used in a mobile phone base station in Bhopal, India (Nema *et al.*, 2010).

Hybrid performance of solar PV/wind turbine/Proton exchange membrane fuel cell (PEMFC) had been studied for remote applications (Agbossou *et al.*, 2001). The study shows that the performance of an independent solar PV/wind turbine/fuel cell/electrolytic cell/battery hybrid system could generate enough electricity to meet peak loads (Eroglu *et al.*, 2011). However, they did not discuss the economics of the system.

The report showed that adding an auxiliary power source from battery packs or fuel cells, or a utility grid, to this would ensure the reliability of the system without requiring excessive hardware (Luna-Rubio *et al.*, 2012). A renewable energy system had been developed based on HOMER platform to identify different cost components (Rajanna *et al.*, 2014). Three different configurations of HRES were developed in six geographic zones of Nigeria (Olatomiwa *et al.*, 2015), and it can be determined economic feasibility solution using HOMER software with sensitivity cases of $1.1–$1.3 based NPC and COE. Based on the availability of meteorological data, a statistical analysis of the wind and solar potential had been studied in rural Nigeria (Olatomiwa *et al.*, 2018). It used HOMER software platform to design and tune technologically and economically optimal hybrid energy system components. An off-grid hybrid microgrid consisting of solar PV, diesel generator, wind turbine, and battery storage devices had been built on the HOMER software platform (Hossen *et al.*, 2022). The proposed load following (LF) strategy performs as the best dispatch strategy with the lowest CO_2 emissions (0.3 kt/year), LCOE (0.03 $/kW), and NPC (15.7 M$). LF also performed the best in terms of system stability and reliability having stable voltage, frequency, active power and reactive power responses.

A framework composed of wind turbines, diesel generators and batteries, and output the optimal combination of 10 wind turbines, 4 diesel engines and 2 battery modules had been built on the HOMER software platform (Shezan *et al.*, 2022). The proposed framework is financially and ecologically feasible, and that the NPC and CO_2 outflow are diminished by around 74% and 92% separately every year contrasted with customary power plants. An island hybrid microgrid with solar PV, wind turbine, diesel enerator and battery storage system had been built, and four scheduling strategies, load following, cycle charging, generator order and combination dispatch had been evaluated (Shezan *et al.*, 2021). The stability of the method is verified by voltage, frequency, active power, and reactive power. Results show that the generator order scheduling strategy is the best in terms of minimum operating costs, net current costs, and CO_2 emissions.

Two hybrid off-grid renewable energy system is designed on the HOMER software platform, and a comparative analysis on the technical economy and system stability of five scheduling strategies had been studied, which had guiding significance for the energy management of Dhaka and Khulna region in Bangladesh (Shezan *et al.*, 2022). The optimal size and technical economics of hybrid microgrid systems consisting of solar PV, diesel generators, battery storage and wind turbines had been evaluated (Shezan *et al.*, 2022). They described the voltage, frequency, power performance and reliability indicators of the simulated microgrid. The results show that LF is considered to be the best in terms of system reliability and stability.

A technical and economic analysis of a cluster hybrid renewable energy system in Three villages in India had been studied (Vendoti *et al.*, 2018). For transient use, most use batteries, while for continuous use, hydrogen storage is profitable. According to the report, the use of PEM fuel cells stabilized the power supply of the communication station in severe weather conditions, and its hydrogen to electricity conversion efficiency exceeded 42%.

The core target of this study is to develop and assess a PV-WT-BATT-EL-HT stand-alone HRES for satisfying the electrical demand of a large office building in Changchun. The main contribution of this paper can be summarized as below:

1) Using HOMER Pro HRES platform, to determine the optimum sizes for its optimal operation which secures minimum NPC, COE, and operating cost.
2) Compared with the grid connected system, the output of this system is directly supplied to the load, and the discarded power is consumed internally. On the premise of ensuring its normal operation, it will not affect the external power grid, thus the system performs with higher stability and reliability.

2. METHODOLOGY

A. Study Area

Changchun is an industrial city of Jilin province, located in the north of China. The latitude and Longitude of Changchun is 43°75'N and 125°25'E. According to data from Changchun meteorological monitoring station, the highest wind speed is occurred in April with 7.84 m/s, and the lowest wind speed is occurred in August with 5.29 m/s. In addition, the lowest daily radiation is allocated to December with 1.73 kWh/m^2/day, while the highest daily radiation corresponds to May with 6.069 kWh/m^2/day. Thus, the abundance of wind and solar resources in Jilin province especially Changchun offers a suitable environment for the inclusion of hybrid renewable energy systems.

B. Load and Resources Assessment

The case study selected in this paper is an office building of Jilin University, covering an area of 5220 square meters, with a total office area of 165,635 square meters and a total of 10 floors high, the office building is shown in Figure 1. Table 1 Average and peak load of the study case. The total yearly power demand based on hourly and monthly loads has been determined using HOMER Pro software as shown in Figure 2.

Figure 1: The study case in Jilin University

Table 1
Average and peak load

Particulars	Details
Average (kWh/d)	5,000.00
Average (kW)	208.33
Peak (kW)	494.69

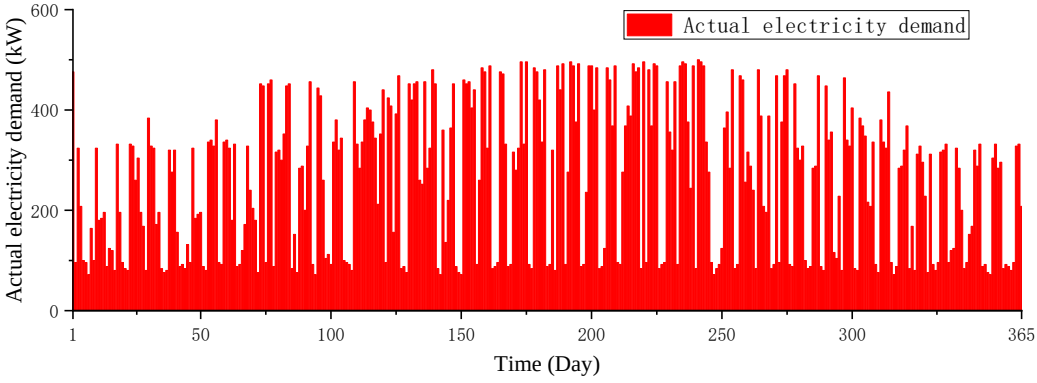

Figure 2: The load profile of a year

C. Optimization based on HOMER Software

As stated earlier, the primary purpose of the study is to determine the size and cost optimization of an off-grid hybrid energy system. Based on the database available, the proposed configuration is simulated using HOMER Pro software, developed by National Renewable Energy Laboratory (NREL), USA.

The design of the system under consideration comprises seven components: Wind Turbine Generator, Solar Photovoltaic, direct current (DC) to alternating current (AC) converter, battery, electrolyzer, hydrogen tank and primary load as presented in Figures 3 and 4. The time period of the project is 20 years with yearly unmet load of zero. The time period of the project is 20 years with yearly

unmet load of zero. For the reactive power in the system, the reactive capacitor compensator is set to ensure the supply voltage and frequency. The total compensation capacity is as follows:

$$Q_c = \beta_{av} q_c P_c \quad (1)$$

Here, P_c is monthly maximum active calculated load supplied by the substation (kW). β_{av} is monthly average load rate, generally $0.7 - 0.8$. q_c is capacitor compensation rate ($kvar/kW$), reactive power to be compensated for each kilowatt of active load. Parameters of hybrid renewable energy systems are shown in Table 2.

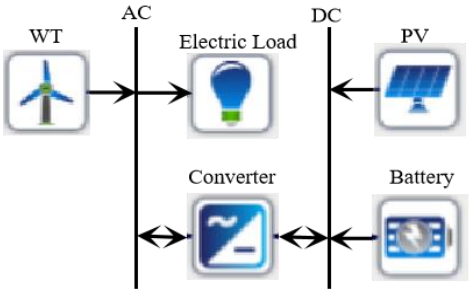

Figure 3: Solar PV, wind turbine and battery storage system (PV-WT-BATT)

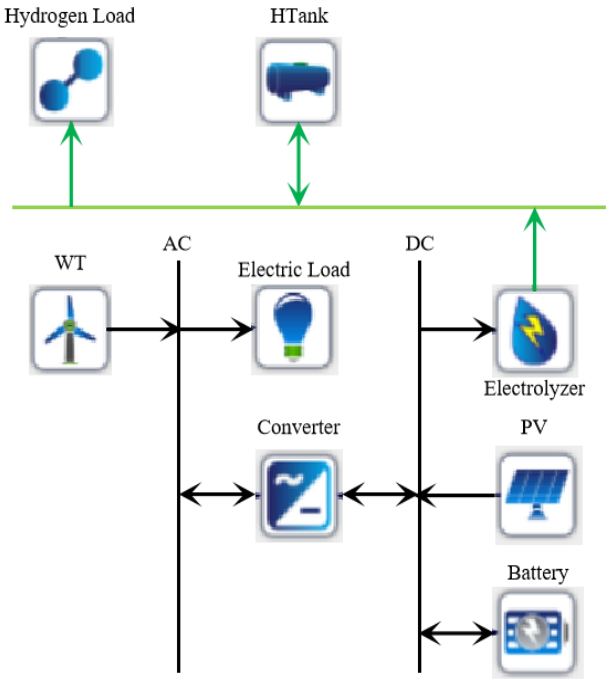

Figure 4: Solar PV, wind turbine, battery storage system, electrolyzer, hydrogen tank (PV-WT-BATT-EL-HT)

Table 2
Parameters of hybrid renewable energy systems

Quantity	Wind Turbine (kW)	PV (kW)	Battery (kWh)	Converter (kW)	Electrolyzer (kW)	Hydrogen tank (kg)
Size	1,000	1	100	1	5	1
Capital (¥)	500,000	2,500	70,000	300	5,000	6,000
Replacement (¥)	500,000	2,500	70,000	300	4,000	5,000
O&M (¥/yr)	5,000	10	1,000	0	300	4,380
Lifetime (year)	20	25	15	15	20	25

Here, as a financial measure, the total net present cost is considered for assessing of the proposed hybrid system. It includes net present capital cost (NPC), operation & maintenance cost, and replacement cost of components. The levelized cost of energy (COE) is defined as the average cost per kWh of useful electrical energy produced by the system. HOMER determines the system operation combinations based on capital cost, net present cost, and levelized cost of energy (COE).

Cost of Energy (COE): To compute the optimal COE for a hybrid system in HOMER, the following equation has been used:

$$COE = \frac{C_{ann,tot}}{E_{prim} + E_{def} + E_{grid,sales}} \quad (2)$$

Here, $C_{ann,tot}$ is total annualized cost, E_{prim} is total amounts of primary load, E_{def} is total amounts of deferrable load, and $E_{grid,sales}$ is amount of energy sold to the grid per year.

Net Present Cost (NPC): To calculate the total net present cost, the following equation has been used:

$$NPC = \frac{C_{ann,tot}}{CRF(i, R_{proj})} \quad (3)$$

Here, $C_{ann,tot}$ is total annualized cost, i is annual real interest rate, R_{proj} is Project lifetime, and $CRF(.)$ is Capital recovery factor.

3. RESUITS AND DISCUSSION

Once all input parameters are completed, the lowest cost is selected as the optimization target. Thereafter, the simulation calculation has been undertaken. Among many combinations, only two combinations are selected and the results of each of these two are discussed below:

A. Combination 1: PV-WT-BATT

In Combination 1, as shown in Figure 3, excess power generated by PV and wind turbine is stored in the battery. The size of PV, WT and battery are 778 kW, 6,000 kW and 2,300 kWh respectively.

The lowest COE of Combination 1 is 0.433 CNY/kWh and total NPC is 9.70M CNY. Among all components, the wind turbine shows the highest cost as 3,805,242.38 CNY. The power generation of each component is shown in Table 3.

As Figure 2 shows that the off-grid hybrid energy system needs a large amount of unit capacity to meet the load demand, which not only increases the total cost of the

system, but also generates a large amount of excess electricity, as shown in Figure 5.

B. Combination 2: PV-WT-BATT-EL-HT

In order to reduce the excess power, the wind turbine generator, electrolyzer and battery system are considered in the system of Combination 2, as shown in Figure 4. In this combination, the excess electricity is further used by the electrolyzer to produce hydrogen and stored in the hydrogen tank, where the fuel cell uses the hydrogen to generate electricity to meet load requirements when wind and solar power are insufficient. To find the most optimal solution for the proposed hybrid energy system and evaluate the effect of uncertainty and/or changes within the variables, the sensitivity analysis has been undertaken. HOMER software is used to simulate each configuration and determine the effects on changing factors. The system has two sensitivity variables electrolyzer and hydrogen tank and size are considered during this study.

From Table 4, it is noted that the difference in the absorption of excess electricity is only 0.2% between configuration 2 and 4, whereas the NPC of configuration 2 increases by ¥2,200,000, while the NPC of configuration 4 increases by only ¥1,100,000, so configuration 4 is considered superior to configuration 2. The absorption of excess electricity in configuration 2 and 4 is 17.8% and 18.9% respectively, with corresponding NPC increases by ¥2,300,000 and ¥2,400,000. Through comparative analysis of configuration 4, which absorbs 16% excess electricity with NPC increased by ¥1,100,000, we conclude that configuration 4 utilizes a relatively large amount of excess electricity, with the least cost price increase. The final optimization result is shown in Figure 5.

Table 3
Comparison of NPC, COE and operating cost of different hybrid renewable energy systems

PV (kW)	WT (kW)	Battery (kWh)	Converter (kW)	Dispatch	NPC (CNY)	COE (CNY)	Operating cost (CNY/yr)
778	6×1000	23×100	550	CC	9.70M	0.433	140,366
	10×1000	43×100	426	CC	11.1M	0.505	230,415
1931		51×100	541	CC	13.7M	0.618	169,448
4916	49×1000		631	CC	51.6M	2.3	562,897

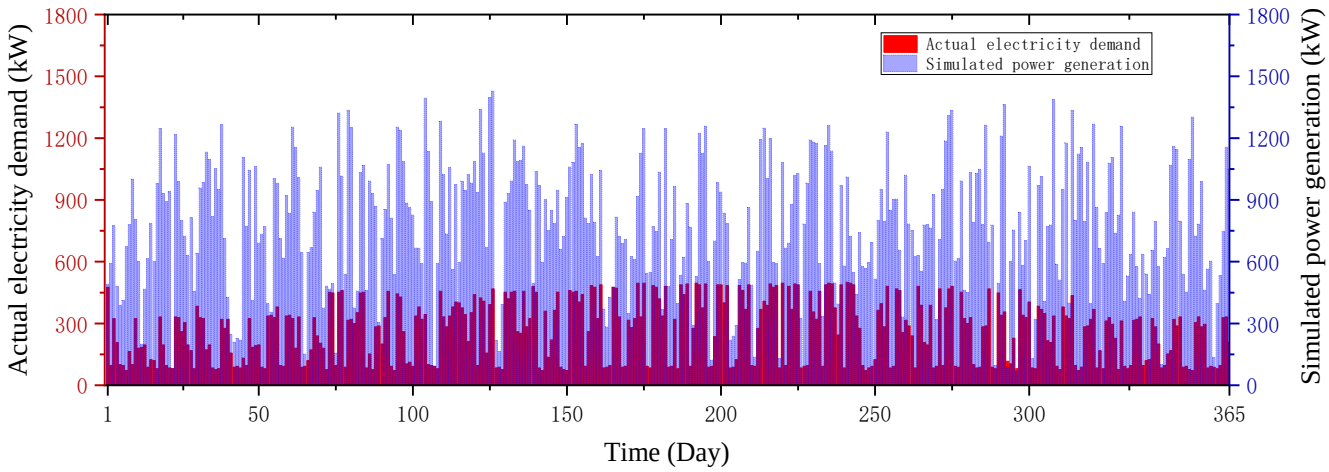

Figure 5: Excess electricity production

Table 4
Sensitivity analysis

Configurations	Electrolyzer (kW)	Hydrogen tank	NPC (¥)	COE (¥)	Excess Electricity
1	0	0	9.7M	0.433	45.4%
2	150	30	11.9M	0.530	29.6%
3	200	30	12.0M	0.534	27.5%
4	250	10	10.8M	0.483	29.4%
5	250	30	12.1M	0.539	26.5%

Table 5
The result of NPC, COE and operating cost of PV-WT-BATT-EL-HT

PV (kW)	WT (kW)	Battery (kWh)	Electrolyzer (kW)	HTank (kg)	Converter (kW)	Dispatch	NPC (CNY)	COE (CNY)	Operating cost (CNY/yr)
778	6×1000	23×100	250	10	499	CC	10.8M	0.483	204,082

This paper selects a relatively small electrolytic cell with a capacity of 250kW, which can reduce the annual discarded electricity by 19.7%. However, it increases the cost by 1.1 million CNY.

C. System Comparison

The comparative analysis between the Combination 1 and the Combination 2 have been articulated in Figure 5 and 6. For Combination 2, NPC, COE, and operating cost are higher (10.8M yuan, 0.483 yuan/kWh, and 204,082 yuan; respectively). On the other hand, it is found to be lower in excess electricity (29.4%). In general, it is critical to balance production and consumption in the case of renewable source-based microgrids with hydrogen as backup load. This is of great significance to improve system stability.

4. CONCLUSIONS

In this work, two hybrid renewable energy systems (HRES) have been optimized and evaluated using different sizes of the system. Simulation analysis shows that the optimal combination of HRES components for this study is 778 kW PV array, 6,000 kW wind turbine, 250 kW electrolyzer, 2,300 kWh battery and 10 kg hydrogen tank. The cost of energy (COE) is 0.483 CNY/kWh, and the total net present cost (NPC) is 10.5M CNY. As can be seen from the analysis in this paper, the cost of PV-WT-BATT is lower than PV-WT-BATT-EL-HT, but the reliability of the former cannot be guaranteed unless other technical options are considered. The summary of these results is listed as follows:

a) The combination of multiple energy systems improves the reliability of energy supply and therefore makes more business sense.

b) Unless properly supported by the government sector, the cost of electricity supply based entirely on renewable energy may not always be a cost-benefit option.

ACKNOWLEDGEMENT

The authors express their sincere gratitude and thanks to Royal Academy of Engineering of United Kingdom (UK) for the financial support under the UK-China Industry Academia Partnership Program scheme (UK-CIAPP\201).

REFERENCES

Byrne J, Shen B, & Wallace W. (1998). The economics of sustainable energy for rural development: A study of renewable energy in rural China. Energy Policy. 26(1):45-54.

Heidari A, Hajinezhad A, & Aslani A. (2019). A Sustainable Power Supply System, Iran's Opportunities via Bioenergy. Environmental Progress & Sustainable Energy. 38(1):171-88.

Shirmohammadi R, Soltanieh M, & Romeo LM. (2018). Thermoeconomic analysis and optimization of post-combustion CO_2recovery unit utilizing absorption refrigeration system for a natural-gas-fired power plant. Environmental Progress & Sustainable Energy. 37(3):1075-84.

Armin R. A, Sumper A, & Davarpanah A. (2019). Development of sustainable energy indexes by the utilization of new indicators: A comparative study. Energy Reports. 5:375-83.

Aslani A, Mazzuca-Sobczuk T, Eivazi S, & Bekhrad K. (2018). Analysis of bioenergy technologies development based on life cycle and adaptation trends. Renew Energy. 127:1076-86.

Khatibi A, Pourebrahim S, & Bin Mokhtar M. (2018). Simulating carbon sequestration using cellular automata and land use assessment for Karaj, Iran. Solid Earth. 9(3):735-44.

Khatibi A, Pourebrahim S, & Danehkar A. (2018). A Cellular Automata Model for Monitoring and Simulating Urban Land Use/Cover Changes toward Sustainability. Journal of Environmental Engineering and Landscape Management. 26(1):1-7.

Razmjoo A, Sumper A, Marzband M, Davarpanah A, Shahhoseini A, & Sarlak S. (2019). Energy sustainability analyses using feasible indicators for urban areas. International Journal of Energy and Water Resources. 3(2): 127-40.

Bakhtiar A, Aslani A, & Hosseini SM. (2020). Challenges of diffusion and commercialization of bioenergy in developing countries. Renew Energy. 145: 1780-98.

Hosseini S.M, Aslani A, Naaranoja M, & Hafeznia H. (2017). Analysis of Energy System in Sweden based on Time series Forecasting and Regression Analysis. International Journal of Energy Optimization and Engineering. 6(3): 97-113.

Mohammadi M, Ghasempour R, Razi Astaraei F, Ahmadi E, Aligholian A, & Toopshekan A. (2018). Optimal planning of renewable energy resource for a residential house considering economic and reliability criteria. International Journal of Electrical Power & Energy Systems. 96: 261-73.

Lotfi B, & Wang Q. (2013). Robust multi-objective optimization of state feedback controllers for heat exchanger system with probabilistic uncertainty. 796-809.

Soltani S, Kasaeian A, Sarrafha H, & Wen D. (2017). An experimental investigation of a hybrid photovoltaic/thermoelectric system with nanofluid application. Solar Energy. 155: 1033-43.

Das M, Singh MAK, & Biswas A. (2019). Techno-economic optimization of an off-grid hybrid renewable energy system using metaheuristic optimization approaches – Case of a radio transmitter station in India. Energy Conversion and Management. 185: 339-52.

Yang H, Zhou W, Lu L, & Fang Z. (2008). Optimal sizing method for stand-alone hybrid solar–wind system with LPSP technology by using genetic algorithm. Solar Energy. 82(4): 354-67.

Khan, Iftekhar, Chowdhury, H., Rasjidin, R., Alam, F., Islam, T. & Islam, S. (2012). Review of Wind Energy Utilization in South Asia. 2012. doi: 10.1016/j.proeng. 10.130.

Kolhe M, Kolhe S, & Joshi JC. (2002). Economic viability of stand-alone solar photovoltaic system in comparison with diesel-powered system for India. Energy Economics. 24(2): 155-65.

Nema P, Rangnekar S, & Nema RK, (2010). Pre-feasibility Study of PV-Solar / Wind Hybrid Energy System for GSM Type Mobile Telephony Base Station in Central India. 2nd International Conference on Computer and Automation Engineering (ICCAE); 2010 Feb 26-28; Singapore, SINGAPORE2010.

Agbossou K, Chahine R, Hamelin J, Laurencelle F, Anouar A, & St-Arnaud JM, *et al.* (2001). Renewable energy systems based on hydrogen for remote applications. Journal of Power Sources. 96(1): 168-72.

Eroglu M, Dursun E, Sevencan S, Song J, Yazici S, & Kilic O. A (2011). Mobile renewable house using PV/wind/fuel cell hybrid power system. International Journal of Hydrogen Energy. 36(13): 7985-92.

Luna-Rubio R, Trejo-Perea M, Vargas-Vázquez D, & Ríos-Moreno GJ. (2012). Optimal sizing of renewable hybrids energy systems: A review of methodologies. Solar Energy. 86(4):1077-88.

Rajanna S, Saini RP, (2014). Optimal Modeling of Solar/Biogas/Biomass based IRE System for a Remote Area Electrification. 6th IEEE Power India International Conference (PIICON); Dec 05-07; New Delhi, INDIA. NEW YORK: Ieee; 2014.

Olatomiwa L, Mekhilef S, Huda ASN, & Ohunakin OS. (2015). Economic evaluation of hybrid energy systems for rural electrification in six geo-political zones of Nigeria. Renew Energy. 83: 435-46.

Olatomiwa L, Blanchard R, Mekhilef S, & Akinyele D. (2018). Hybrid renewable energy supply for rural healthcare facilities: An approach to quality healthcare delivery. Sustainable Energy Technologies and Assessments. 30: 121-38.

Hossen M D, Islam M F, Ishraque M F, *et al.* (2022). Design and Implementation of a Hybrid Solar-Wind-Biomass Renewable Energy System considering Meteorological Conditions with the Power System Performances. International journal of photoenergy, 2022.

Shezan S K A, & Lai C Y, (2017). Optimization of hybrid wind-diesel-battery energy system for remote areas of Malaysia, 1-6.

Shezan S A, Hasan K N, Rahman A, *et al.* (2021). Selection of appropriate dispatch strategies for effective planning and operation of a microgrid[J]. Energies (Basel), 14(21): 7217.

Shezan S A, Ishraque M F, Muyeen S M, *et al.* (2022). Selection of the best dispatch strategy considering techno-economic and system stability analysis with optimal sizing. Energy strategy reviews, 43: 100923.

Shezan S A, Ishraque M F, Muyeen S M, *et al.* (2022). Effective dispatch strategies assortment according to the effect of the operation for an islanded hybrid microgrid[J]. Energy conversion and management. X, 14: 100192.

Vendoti S, Muralidhar M, & Kiranmayi R, (2018). HOMER Based Optimization of Solar-Wind-Diesel Hybrid System for Electrification in a Rural Village. 8th International Conference on Computer Communication and Informatics (ICCCI); Jan 04-06; Coimbatore, INDIA2018.

MIJST
MIST International Journal of Science and Technology

A Novel Approach to Detect Cardiac Arrhythmia Based on Continuous Wavelet Transform and Convolutional Neural Network

Shadhon Chandra Mohonta[1*], and Md. Firoj Ali[2]

[1]Department of Electrical & Electronic Engineering, Rajshahi University of Engineering & Technology, Rajshahi, Bangladesh
[2]Department of Mechatronics Engineering, Rajshahi University of Engineering & Technology, Rajshahi, Bangladesh

emails: *[1]shadhonmohonta@gmail.com; and [2]eeemfa07@gmail.com*

ARTICLE INFO

Article History:

Received: 19th March 2022
Revised: 29th June 2022
Accepted: 16th August 2022
Published: 29th December 2022

Keywords:

Electrocardiogram
Continuous Wavelet Transform
Arrhythmia
Convolutional Neural Network

ABSTRACT

Electrocardiogram (ECG) signal is informative as well as non-invasive clinical tool to diagnose cardiac diseases of human heart. However, the diagnosis requires professionals' clarification and is also time-consuming. To make the diagnosis proficient, a novel convolutional neural network (CNN) has been proposed for automatic arrhythmia detection. In this work, the ECG data collected from the MIT-BIH database have been preprocessed, and segmented in short ECG segments of 60 s. Then, all these segments have been transformed into scalogram images obtained from time-frequency analysis using continuous wavelet transform (CWT). Finally, these scalogram images have been exploited as an input for our designed CNN classifier to classify cardiac arrhythmia. In this approach, the overall accuracy, sensitivity, and specificity are 99.39%, 98.79%, and 100% respectively. Proposed CNN model has significant advantages, and it can be used to differentiate the healthy and arrhythmic patients effectively.

1. INTRODUCTION

The amount of cardiovascular diseases upsurges incredibly and 17.3 million people decease every year conveyed by World Health Organization (WHO) (Mendis, Puska, Norrving, & Organization, 2011). The arrhythmias are most serious among them, and may cause sudden cardiac arrest or stroke (Huikuri, Castellanos, & Myerburg, 2001). Indeed, proper diagnosis of arrhythmias can considerably preclude such sudden cardiac death. ECG comprises complete details about the normality or abnormality of human heart, and various classes of arrhythmias can be diagnosed from it. In (De Bie, Martignani, Massaro, & Diemberger, 2020), short-term samples of 10 s obtained from pediatric and adult patient's ECG signals for atrial fibrillation or other abnormal rhythms detection. Furthermore, various feature extraction approaches such as time-domain and frequency-domain, statistical, and time-frequency analysis have been implemented for arrhythmia detection. Here, the features like heart rate, RR interval, R amplitude, PR interval, QRS duration, P-wave, and T-wave duration (Chen, Wang, & Wang, 2018; De Chazal & Reilly, 2006; Mitra, Mitra, & Chaudhuri, 2006) have been extracted from the time-domain analysis . Moreover, statistical features have been extracted in terms of variance, kurtosis, and skewness (Queiroz, Azoubel, & Barros, 2019; Queiroz, Junior, Lucena, & Barros, 2018). Besides, many literatures implemented wavelet transform to classify ECG arrhythmias in time-frequency analysis (Banerjee & Mitra, 2013; Khorrami & Moavenian, 2010).

In addition, to assist clinicians for detecting and classifying arrhythmias automatically a CNN based approached has been emerged in recent years. The CWT and CNN based approach has been proposed jointly for automatic arrhythmia classification with an overall accuracy of 98.74% (Wang et al., 2021). Here, the 2D-scalograms obtained from CWT while features extraction conducted using CNN from those scalograms. Moreover, different cardiac arrhythmias have been detected after the preprocessing of ECG signals using a 34-layer CNN (Brisk et al., 2019), 1D-CNN of 31-layers (Li, Zhou, Wan, Li, & Mou, 2020), CNN with long short-term memory (LSTM) (Chen et al., 2018), and 11-layer deep CNN (Acharya et al., 2017). Besides, a combination of signal quality index (SQI) algorithm and densed-CNN has been proposed to distinguish atrial fibrillation from short ECG segments (9–60 s) (Rubin, Parvaneh, Rahman, Conroy, & Babaeizadeh, 2018). Additionally, for automatic classification of cardiac arrhythmias various new models such as wavelet transform with 2D-CNN (Mohonta, Motin,

& Kumar, 2022), deep neural network (DNN) models constitutive of residual convolutional modules and bidirectional LSTM (He et al., 2019), and Deep Multi-Scale Convolutional neural network Ensemble (DMSCE) (Prabhakararao & Dandapat, 2021) have been proposed.
In this work, a new CNN model has been proposed to recognize the subjects with arrhythmias, and discriminate them from the healthy one. To expedite this, ECG segments of 60 s have been transformed into RBG scalograms based on CWT method for pattern recognition. Then, these scalograms of ECG segments have been fed into our proposed CNN model for automatic detection of cardiac arrhythmias.
The remainder of the paper is depicted as follows: section 2 describes the materials and methods part. In section 3, a comprehensive results and discussion has been presented based on proposed classifier performance. Finally, the conclusion is in fourth section.

2. MATERIALS AND METHODS

Our proposed method for arrhythmia detection has been divided into six stages containing data acquisition, pre-processing, segmentation, R peak detection, time-frequency transformation, and CNN classifier. The overall layout of our proposed method is shown in Figure 1.

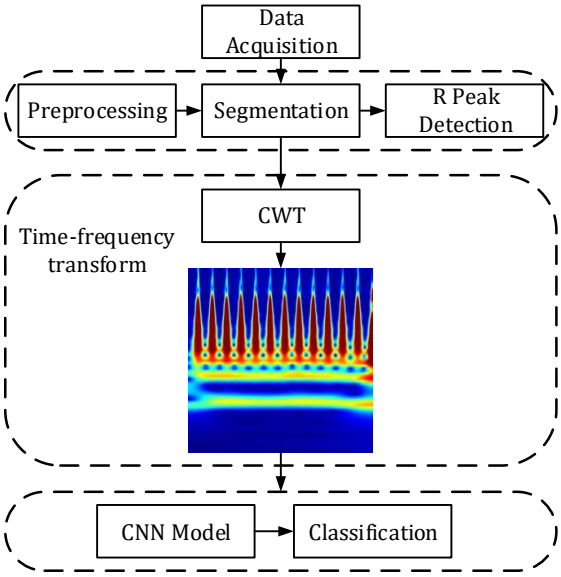

Figure 1: Overall layout for arrhythmia detection

A. Data Acquisition

The ECG data have been separated into two groups: healthy subjects, and the subjects with arrhythmia. The data is considered from the MIT-BIH database, and the duration of ECG recordings of each subject is 30 min. Here, 13 subjects have been grouped as healthy considered from normal sinus rhythm (NSR) database, whether 52 subjects have been considered from arrhythmia (ARR), atrial fibrillation (AFI), supraventricular arrhythmia (SVA) and malignant ventricular ectopy (MVE) database to form arrhythmic group.

B. Pre-processing and Segmentation

In pre-processing, the discrete wavelet transform (DWT) has been considered for eliminating the noise, baseline wander and artefacts from ECG signals. The low and high-frequency components of a signal has been decomposed using DWT, and then the signal has been reconstructed. Here, the ECG signal has been decomposed considering 'sym4' wavelet where low-frequency and high-frequency information are carried out by the approximation coefficient, and the first and second level detail coefficients respectively. Therefore, the denoised ECG singals have been reconstructed based on inverse wavelet transform only considering the third and fourth level detail coefficients. After that, each ECG recording has been divided into segments with 60 s duration. The segmented raw and filtered ECG signal of 60 s are shown in Figure 2 and Figure 3 respectively. So, the healthy and arrhythmic group have total 390 and 1560 segments respectively.

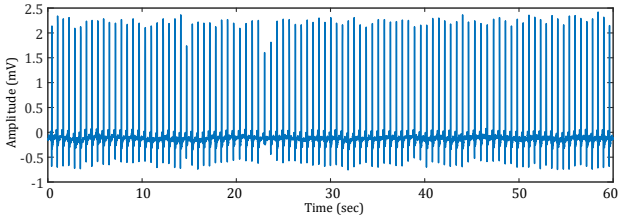

Figure 2: Original ECG signal

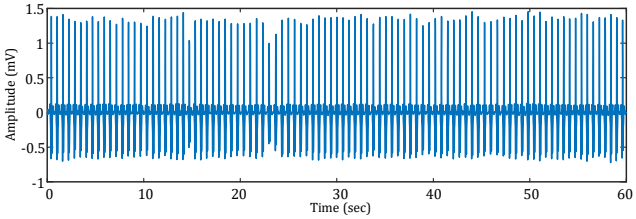

Figure 3: Filtered ECG signal

C. R Peak Detection

In this paper, the R peaks of ECG signal have been detected in three steps: (i) squaring the magnitude of the signal, (ii) finding the average value, and (iii) detecting R peaks. Here, the threshold value for the minimum peak height is the average value, and 0.14 s is considered as minimum peak height. The detected R peaks of a ECG signal is shown in Figure 4.

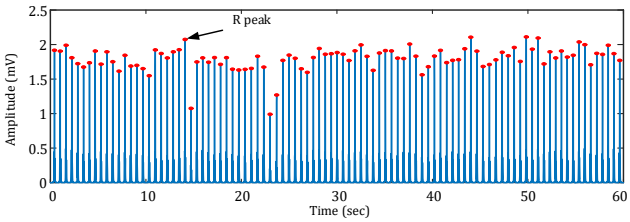

Figure 4: Detection of R peaks

There are a number of segments in healthy, and arrhythmic group which contain abnormal, and normal rhythm respectively. To exclude these undesirable segments, the detected R peaks have been used to compute the average heart rate (AHR) for each segment. After that, the segments which are in normal range ($60\ bpm \leq AHR \leq 100 bpm$), and abnormal range

($60\ bpm > AHR, or\ 100\ bpm < AHR$) have been nominated for the healthy group, and arrhythmic group respectively. In this way, the segment's selection has been conducted, and finally each group contains total 249 ECG segments.

D. Time-Frequency Analysis

In this analysis, ECG signals are represented in time-frequency domain, and has medical importance to diagnose different cardiovascular diseases. Here, all the segments of each group have been converted into scalogram images from using CWT. The CWT Scalograms decompose the information of a signal in spectral patterns.

The CWT for a continuous signal $x(t)$, is defined as follows (Wang et al., 2021)

$$CWT_x(a,b) = \frac{1}{\sqrt{a}} \int_{-\infty}^{\infty} x(at)\, \psi^* \left(\frac{t-b}{a}\right) dt \qquad (1)$$

Where, $\psi^*(t)$, t, a, and b are the complex conjugate of the basic wavelet, time shift, scale factor, and location parameter respectively.

E. CNN Model

In this analysis, a CNN network has been proposed to detect arrhythmia from RGB scalogram. It consists of several common layers: convolutional (Conv), Rectified Linear Unit (ReLU), batch normalization (BN), max pooling (MaxPool), fully connected (FC) and softmax. The basic model of proposed CNN is shown in Figure 5.

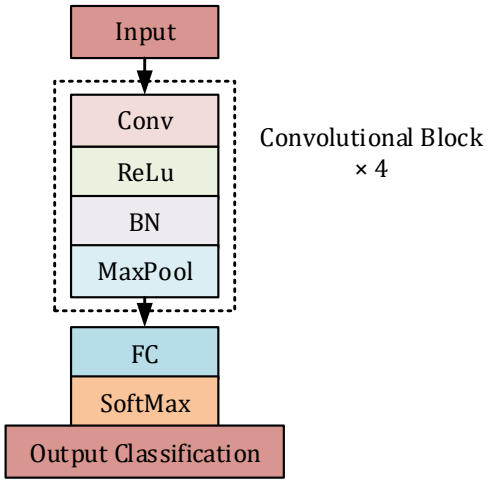

Figure 5: The basic model of proposed CNN

The input of the network is RGB time-frequency scalogram of size 227×227×3. This model has four convolutional block. Every convolutional block contains convolutional layer, batch normalization layer, and a pooling layer. A non-linear activation function, ReLu, is used after the convolutional layer to enhance the approximation ability between each layer of the network. Besides, the function of the batch normalization layer is to batch normalize the activation output of the layer. The parameters of the max pooling layer of every convolutional block are same, and have the Kernel size 3×3 and the stride 2. But, the parameters of convolutional layer in each block are different. Moreover, the fully connected layer shows the classification results and the softmax activation function implies the probability that the input belongs to each class. Finally, 70% of images have been considered to train our model, and rest are used for testing. Table 1 represents the summarization of the proposed CNN model.

Table 1
Summaries the parameters of proposed CNN model

Layer Type	Kernel Size	Stride	Kernel	Padding
Conv_1	11×11	4	64	-
MaxPool_1	3×3	2	-	-
Conv_2	5×5	1	256	2
MaxPool_2	3×3	2	-	-
Conv_3	3×3	1	384	1
MaxPool_3	3×3	2	-	-
Conv_4	3×3	1	256	1
MaxPool_4	3×3	2	-	-
FC	-	-	2	-

3. RESULTS AND DISCUSSION

In this work, our proposed CNN model is a simple one which consists of only four convolutional layers, and one fully connected layers. Here, RGB scalograms of size 227×227×3 of all ECG segments have been obtained from CWT method for arrhythmia detection. After that, the designed CNN model took these scalograms as an input, and differentiate arrhythmic subjects from the healthy ones automatically. Here, total 348 scalograms are used to train the model, while 150 images are considered for testing purpose. In this approach, 6 epochs and 204 iterations have been considered, and it took around 13 min to compete the classification process. The confusion matrix of the proposed CNN model is shown in Figure 6.

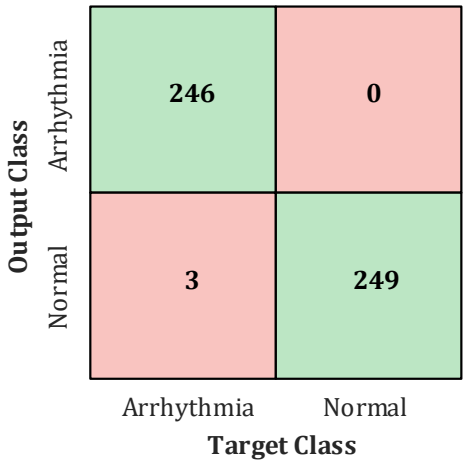

Figure 6: Confusion matrix for proposed CNN model

Here, three statistical parameters have been computed to evaluate the performance of our classifier which are as follows (Queiroz et al., 2019):

$$Se(\%) = \frac{TP}{TP+FN} \times 100 \qquad (2)$$

$$Sp(\%) = \frac{TN}{TN+FP} \times 100 \qquad (3)$$

$$Acc(\%) = \frac{TP+TN}{TP+FP+TN+FN} \times 100 \quad (4)$$

Where, *Se* is the sensitivity which represents how the technique is effective for detecting arrhythmia, *Sp* is the specificity which denotes how the technique is effective for detecting healthy subjects, and *Acc* is the accuracy which measures the effectiveness of the technique regarding diagnosis. Also, *TP* is the true positive, *TN* is the true negative, *FP* is the false positive, and *FN* is the false negative.

The accuracy and loss curves of our proposed model are shown in Figure 7 and Figure 8 respectively. It is obvious that the network has reached its stable position after approximately 30 iterations.

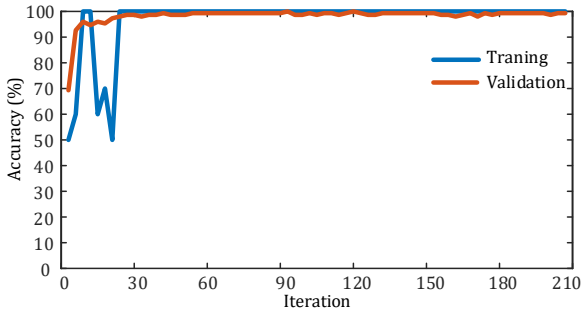

Figure 7: Accuracy of the proposed model

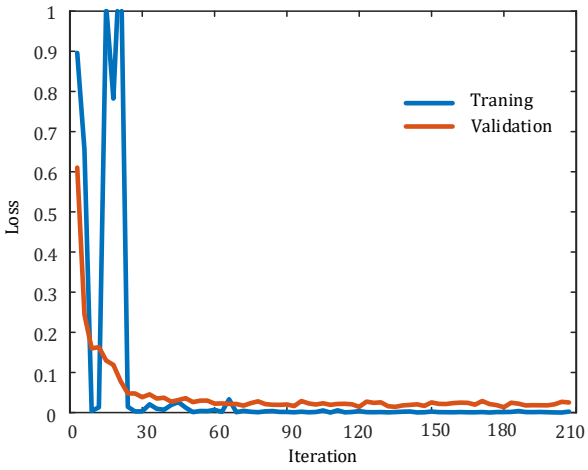

Figure 8: Loss of the proposed model

Table 2
Performance evaluation indicators for proposed CNN model

Sensitivity (*Se*)	Specificity (*Sp*)	Accuracy (*Acc*)
98.79 %	100 %	99.39%

It is apparent from Figure 7 and Figure 8 that the accuracy, and loss are 99.39%, and 0.015 respectively. Besides, the accuracy of the proposed CNN model is better than using a pretrained AlexNet model (Mohonta & Ali, 2021). Besides, the statistical indices such as sensitivity (*Se*), specificity (*Sp*), and accuracy (*Acc*) of this classification are portrayed in Table 2.

The comparison between the performance of our work and other existing methods has been summarized in Table 3. In (Wang et al., 2021), the arrhythmia detection had been performed with a combination of CWT and CNN-based approaches. A deep learning model named ResNet-31 had been used to detect cardiac arrhythmia from single lead ECG signals which showed 99.06% accuracy (Li et al., 2020). Also, a combination of CNN and long short-term memory (LSTM) based model had been proposed for automatic arrhythmia classification, and achieved 98.10% accuracy (Chen et al., 2018). Moreover, accuracy of 94.90% had been achieved for arrhythmia detection using CNN-based approach from ECG segments of 5 s. (Acharya et al., 2017). Arrhythmia has been classified from ECG signal using STFT-based spectrogram and proposed 2D-CNN model, and achieved an overall accuracy of 99.00%.

Table 3
Performance evaluation indicators for proposed CNN model

Reference	Duration of each ECG segment	Notable features	Approach	Overall *Acc*
(Wang et al., 2021)	200 samples (around 0.56 s)	CWT	CNN-18	98.74%
(Li et al., 2020)	300 samples (around 0.83 s)	Deep learning	ResNet-31	99.06%
(Oh, Ng, San Tan, & Acharya, 2018)	1000 samples	Deep learning	CNN and LSTM	98.10%
(Acharya et al., 2017)	5 s	Deep learning	CNN-11	94.90%
(Huang, Chen, Yao, & He, 2019)	10 s	STFT	CNN	99.00%
This study	**60 s**	**CWT**	**CNN**	**99.39%**

In sum, the deep learning model extracts features automatically from CWT scalogram which conveys the time-frequency information of arrhythmia. Actually, the wavelet-based technique decomposes complex information and patterns of an image into elementary forms. Hence, the propounded CNN model has outperformed the other related works, and effectively diagnosed and classified arrhythmic subjects from normal one with an overall accuracy of 99.39%. However, small number of ECG segments has been considered in this analysis. Further analysis could be done with the same approach using large number of segments.

4. CONCLUSIONS

The information of electrical activity of the heart can be epitomized through ECG signal which also helps to diagnose cardiac disorder non-invasively. Here, the

detection of arrhythmia from ECG segments has been conducted based on wavelet transform and CNN classifier. In this diagnosis, a novel CNN model has been incorporated for image recognition that investigates the CWT scalograms, and delivers better performance with an overall accuracy of 99.39%. So, the results demonstrate that the proposed approach automatically extracted features from the ECG signal to distinguish arrhythmic subjects from healthy one successfully. Therefore, this approach can be implemented clinically to guide academicians and medical professionals for efficient arrhythmia diagnosis.

ACKNOWLEDGEMENTS

The authors would like to thank PhysioNet for making the dataset available.

REFERENCES

Acharya, U. R., Fujita, H., Lih, O. S., Hagiwara, Y., Tan, J. H., & Adam, M. (2017). Automated detection of arrhythmias using different intervals of tachycardia ECG segments with convolutional neural network. *Information sciences*, *405*, 81-90.

Banerjee, S., & Mitra, M. (2013). Application of cross wavelet transform for ECG pattern analysis and classification. *IEEE transactions on instrumentation measurement*, *63*(2), 326-333.

Brisk, R., Bond, R., Banks, E., Piadlo, A., Finlay, D., McLaughlin, J., & David, M. (2019). Deep learning to automatically interpret images of the electrocardiogram: Do we need the raw samples? *Journal of electrocardiology*, *57*, S65-S69.

Chen, X., Wang, Y., & Wang, L. (2018). Arrhythmia recognition and classification using ECG morphology and segment feature analysis. *IEEE/ACM transactions on computational biology bioinformatics*, *16*(1), 131-138.

De Bie, J., Martignani, C., Massaro, G., & Diemberger, I. (2020). Performance of seven ECG interpretation programs in identifying arrhythmia and acute cardiovascular syndrome. *Journal of Electrocardiology*, *58*, 143-149.

De Chazal, P., & Reilly, R. B. (2006). A patient-adapting heartbeat classifier using ECG morphology and heartbeat interval features. *IEEE transactions on biomedical engineering*, *53*(12), 2535-2543.

He, R., Liu, Y., Wang, K., Zhao, N., Yuan, Y., Li, Q., & Zhang, H. (2019). Automatic cardiac arrhythmia classification using combination of deep residual network and bidirectional LSTM. *IEEE access*, *7*, 102119-102135.

Huang, J., Chen, B., Yao, B., & He, W. (2019). ECG arrhythmia classification using STFT-based spectrogram and convolutional neural network. *IEEE access*, *7*, 92871-92880.

Huikuri, H. V., Castellanos, A., & Myerburg, R. J. (2001). Sudden death due to cardiac arrhythmias. *New England Journal of Medicine*, *345*(20), 1473-1482.

Khorrami, H., & Moavenian, M. (2010). A comparative study of DWT, CWT and DCT transformations in ECG arrhythmias classification. *Expert systems with Applications*, *37*(8), 5751-5757.

Li, Z., Zhou, D., Wan, L., Li, J., & Mou, W. (2020). Heartbeat classification using deep residual convolutional neural network from 2-lead electrocardiogram. *Journal of electrocardiology*, *58*, 105-112.

Mendis, S., Puska, P., Norrving, B. e., & Organization, W. H. (2011). *Global atlas on cardiovascular disease prevention and control*: World Health Organization.

Mitra, S., Mitra, M., & Chaudhuri, B. B. (2006). A rough-set-based inference engine for ECG classification. *IEEE transactions on instrumentation measurement*, *55*(6), 2198-2206.

Mohonta, S. C., & Ali, M. F. (2021). *Cardiac Arrhythmia Diagnosis based on Features Extraction and Convolutional Neural Network from ECG Signals*. Paper presented at the 2021 5th International Conference on Electrical Engineering and Information & Communication Technology (ICEEICT).

Mohonta, S. C., Motin, M. A., & Kumar, D. K. (2022). Electrocardiogram based arrhythmia classification using wavelet transform with deep learning model. *Sensing Bio-Sensing Research*, 100502.

Oh, S. L., Ng, E. Y., San Tan, R., & Acharya, U. R. (2018). Automated diagnosis of arrhythmia using combination of CNN and LSTM techniques with variable length heart beats. *Computers in biology medicine*, *102*, 278-287.

Prabhakararao, E., & Dandapat, S. (2021). Multi-Scale Convolutional Neural Network Ensemble for Multi-Class Arrhythmia Classification. *IEEE Journal of Biomedical Health Informatics*.

Queiroz, J. A., Azoubel, L. M. A., & Barros, A. K. (2019). Support system for classification of beat-to-beat arrhythmia based on variability and morphology of electrocardiogram. *EURASIP Journal on Advances in Signal Processing*, *2019*(1), 1-9.

Queiroz, J. A., Junior, A., Lucena, F., & Barros, A. K. (2018). Diagnostic decision support systems for atrial fibrillation based on a novel electrocardiogram approach. *Journal of Electrocardiology*, *51*(2), 252-259.

Rubin, J., Parvaneh, S., Rahman, A., Conroy, B., & Babaeizadeh, S. (2018). Densely connected convolutional networks for detection of atrial fibrillation from short single-lead ECG recordings. *Journal of electrocardiology*, *51*(6), S18-S21.

Wang, T., Lu, C., Sun, Y., Yang, M., Liu, C., & Ou, C. (2021). Automatic ECG classification using continuous wavelet transform and convolutional neural network. *Entropy*, *23*(1), 119.

MIJST
MIST International Journal of Science and Technology

Design of an Optimum Massive MIMO FSO System and Analysis of its Performance in Different Weather Conditions

Saif Ahmed[1*], Syed Md. Ahnaf Hasan[2], and A. K. M. Nazrul Islam[3]

Department of Electrical Electronic and Communication Engineering, Military Institute of Science and Technology (MIST), Dhaka, Bangladesh

emails: *[1]saift6700@gmail.com; [2]ahnafhasan@eece.mist.ac.bd; and [3]nazrul@eece.mist.ac.bd*

ARTICLE INFO

Article History:

Received: 15th March 2022
Revised: 17th April 2022
Accepted: 25th August 2022
Published: 29th December 2022

Keywords:

Atmospheric Turbulence
Free Space Optics (FSO)
Gamma-Gamma Fading
Massive MIMO

ABSTRACT

This aim of this work is to propose a massive MIMO FSO system with optimum design parameters and analyze its performance in various turbulent weather conditions by simulating the model in Optisystem 18.0. In recent years, the need for high speed data transfer for real time communication has become a necessity. Implementation of massive MIMO system has already gained remarkable achievement using the conventional RF transmission system. Although it is very much efficient in its application, it has some problems, such as licensing restrictions, bandwidth depletion, fragmentation. In this respect, Free space optics (FSO) is an efficient method for high speed data transfer as it does not have above limitations. Different researches conducted using MIMO FSO models have shown promising results. The use of massive MIMO system (more than 8×8 array of antennas) will enhance data rate further. In this research work, an optimum massive MIMO FSO system has been designed with 16×16 array of antennas. The performance of this system is analyzed in different weather conditions and compared with that of 8×8 system. The analysis of performance is done by power penalty and receiver sensitivity plots. A significant transmission range and an optimum performance is obtained by using this system at a data rate of 40 Gbps. However, data transmission rate can be much more enhanced in this system at the cost of reduced performance and a shorter transmission range.

1. INTRODUCTION

Wireless communication technology has progressed remarkably over the years due to its increasingly high demand. The requirement for higher data rate and bandwidth is also increasing correspondingly with the number of multimedia services (Israr *et al*., 2019). Modern wireless communication system depends on the use of Radio Frequency (RF) signals as the carrier of information. For the time being, the use of RF signals is satisfactory, however, with the rapid increase of internet services, the depletion of bandwidth of RF signals is imminent requiring the need to find a wider band of spectrum. Free Space Optical (FSO) communication can be an optimum solution to this problem. It is being considered as the most promising alternative to RF signals (Chauhan *et al.*, 2021). It has several benefits over RF signals such as license-free spectrum, larger bandwidth, low power consumption, better security and simple and quick installation (Bhatnagar *et al*., 2016). Besides RF communication, FSO can also be considered as an alternative to optical fibre communication as it retains the characteristics of the optical fibre at lower power consumption and easier installation and maintenance (Chatti *et al.*, 2019).

Free Space Optical (FSO) system requires a direct line of sight (LOS) for the communication between transmitter and receiver. Optical wavelengths of 850 nm, 1300 nm and 1550 nm are used for transmitting information (Israr et al., 2019). Because of being a LOS dependent system, the performance of FSO communication is greatly degraded due to the presence of atmospheric turbulence (Badar *et al*., 2017). Various atmospheric processes such as, haze, fog, snow, smoke, clouds, dust, rain etc. can cause signal attenuation due to absorption and scattering of information carrying optical signal (Naboulsi *et al.*, 2004). The refractive index fluctuates due to atmospheric turbulence which in turn creates hindrance to the transmitted light. The received power as a result falls the below the required optimum value. Consequently, the bit error rate (BER) gets increased. This problem may seem to be solved by the use of high-power lasers on the transmitting end, however, the

laser power cannot be increased more than a particular value (10 dBm) by taking practical feasibility and more importantly health safety into considerations.

Recent researches show that the inclusion of the Multiple Input Multiple Output (MIMO) technology can minimize the adverse effects due to atmospheric turbulence to a great extent (Thandapani *et al.*, 2021). MIMO technology enables the transmission of data via multiple redundant paths to achieve very low Bit Error Rate (BER). Besides mitigating the turbulence induced fading MIMO technology can substantially also improve the coverage, better gain in diversity and the total capacity which is proportional to the number of beams used (Zhang, *et al., 2017*). Considering atmospheric turbulence, the FSO channel can be characterized by various statistical models such as Gamma-Gamma distribution model, Kolmogorov spectrum model, Log normal model, K-channel model, etc. The Gamma-Gamma model is the most popular of these models due to its ability to characterize from weak to strong turbulences (Anandkumar, 2021). Analyses conducted under 1 km show very good results by using the MIMO technique in several weather conditions (Sangeetha *et al.*, 2019). The performance can be further improved by addition of more transmitting and receiving antennas.

The objective of this research is to analyse a massive MIMO FSO system in various turbulent weather conditions and to observe its performance in terms of BER, power consumption, transmission distance etc. and to obtain the optimum parameters of the system. The massive MIMO FSO system of diversity order 16 has been selected for the analysis taking practical implementation and cost-effectiveness into consideration. The performance results of this system are further compared to an 8×8 system showing the improvement.

2. BRIEF THEORETICAL BACKGROUND

A. FSO System

FSO communication system transmits light as the carrier of information through free space as the transmission medium (El-Mashade *et al.*, 2015). In this system, a Line of Sight (LOS) linking the transmitter and the receiver is needed for successful data transmission (Dubey, 2020). Since the transmission medium is free space, the atmospheric turbulence becomes a major obstacle causing irradiance fluctuations. With the consideration of atmospheric turbulence, the FSO channel can characterized by several statistical models such as Gamma-Gamma distribution model, Negative exponential model, Kolmogorov spectrum model, Lognormal model. Among these, the Gamma-Gamma model is chosen for this analysis as it gives better results under strong, moderate and weak atmospheric turbulences. Here, the probability density function, $f(I)$ is used to express the Gamma-Gamma model, stated in Equation (1) (Kumar & Khandelwal, 2019):

$$f(I) = \frac{2(\alpha\beta)^{\frac{\alpha+\beta}{2}}}{\Gamma(\alpha)\Gamma(\beta)} I^{\frac{\alpha+\beta}{2}-1} K_{\alpha-\beta}(2\sqrt{\alpha\beta I})\, 2\,, \quad I > 0 \qquad (1)$$

where, 'I' = intensity of the received signal and the parameters 'α' & 'β' are defined small to large scale fading created by atmospheric turbulence, expressed in Equations (2) and (3) (Kumar & Khandelwal, 2019):

$$\alpha = \left(exp\left(\frac{0.49\sigma^2_R}{(1+1.11\sigma_R^{\frac{12}{5}})^{\frac{7}{6}}}\right) - 1\right)^{-1} \qquad (2)$$

$$\beta = \left(exp\left(\frac{0.51\sigma^2_R}{(1+0.69\sigma_R^{\frac{12}{5}})^{\frac{5}{6}}}\right) - 1\right)^{-1} \qquad (3)$$

The Rytov Variance can be expressed as,

$$\sigma^2{}_R = 1.23 C^2{}_n K^{\frac{7}{6}} L^{\frac{11}{6}} \qquad (4)$$

where, L = length of propagation path, K = optical wave number, C_2^n is a measure of the variations of refractive index which indicates the turbulence strength. Values of C_2^n span from $10^{-17}\, m^{-2/3}$ to $10^{-13}\, m^{-2/3}$ for weak to strong turbulences (Jarangal, *et al.*, 2018).

B. Massive MIMO System

In this age of wireless communication, uninterrupted data transfer at a high transmission rate is of great necessity. The massive Multiple Input Multiple Output (mMIMO) system uses large array of antennas in transmitting and receiving sides. Transmission rate of the system increases appreciably by the increased number of antennas. The massive MIMO is an extension of the prevailing MIMO system (Albreem *et al.,* 2019). In MIMO systems, a highest of 8×8 array of antennas can be used (Khwandah *et al.*, 2021). However, in massive MIMO systems, both the transmitting and receiving ends must contain an array of antennas greater than 8. The use of higher number of antennas creates multiple redundant paths for the transmission of data streams. This helps to achieve higher data transmission speed at a low bit error rate. Studies show that data transmission rate as high as 5.5 Gbps can be obtained in conventional radio frequency (RF) systems by using a 20×12 array of antennas (Tsai *et al.*, 2018). A massive MIMO system can have infinite array of antennas from theoretical perspective. However, some problems like low cost- efficiency, and intricacy of the system are encountered during the employment of a large number of antennas (Lu *et al.*, 2014). So, an optimal number of antenna elements needs to be chosen for designing a massive MIMO system. The MIMO channel can be mathematically expressed as (Sangeetha *et al.*, 2019):

$$Y = HX + N \qquad (5)$$

Here, 'X' and 'Y' denote the transmitted and received vectors respectively. 'H' is used to represent the channel matrix and 'N' indicates the noise vector.

3. SIMULATION PARAMETERS

The proposed massive MIMO FSO system was simulated in Optisystem 18.0 and MATLAB R2018a was used to show the graphical outputs. Different parameters used in this simulation of the $16x16$ FSO model are listed in Table 1.

The FSO channel is characterized by the following attenuation coefficients for different weather conditions. The attenuation coefficients are listed in Table 2 (Mansour *et al.*, 2017).

Table 1
Simulation Parameters

Different parameters	Values
FSO Channel	Gamma-Gamma Model
Optical Wavelength	1550 nm
Data Rate	40 Gbps
Distance	1.79 km
M - Z Modulator Extinction Ratio	30 dB
Refractive Index Parameter (C_n^2)	10^{-17}-10^{-13} $m^{-2/3}$
Transmitter Aperture Diameter	2.5 cm
Receiver Aperture Diameter	37.5 cm
Absolute Noise Temperature	298 K
Responsivity (APD)	1 A/W
Dark Current (APD)	10nA
Avalanche Photo Diode Gain	3
Receiver Load Resistance	50 Ω
Beam Divergence	2 mrad
Bessel Filter Cut-off Frequency	7.5 GHz
Loss in Transmitting end	1.8 dB
Loss in Receiving end	1.8 dB
Auxiliary Losses	1 dB

Table 2
Attenuation Values of FSO Channel in Various Turbulent Weather conditions

Weather Condition	Attenuation Coefficients, dB/km
Clear Weather	0.43
Haze	4.2
Moderate Rain	5.8
Heavy Rain	9.2

4. SIMULATION LAYOUT

Simulation block diagram and layout of the 16 × 16 FSO system are shown in Figure 1 and Figure 2. In this model, a CW laser source has been used as the light carrier. At first, the random bit sequence is produced by using a Pseudo-Random Bit Sequence (PRBS) generator. This data stream is then converted to voltage levels by a Non-Return to Zero (NRZ) Pulse Generator. The optical carrier is modulated with the baseband signal by Mach-Zehnder (MZ) modulator. This modulated optical signal is transmitted through the FSO channel by the continuous wave (CW) lasers at the transmitting end. In the receiving end, Avalanche Photo Diode (APD) detector receives this signal and Low Pass Filter (LPF) and 3R Regenerator are used to reconstruct the original data. A Bit Error Rate (BER) analyzer has been used to analyze the received signal.

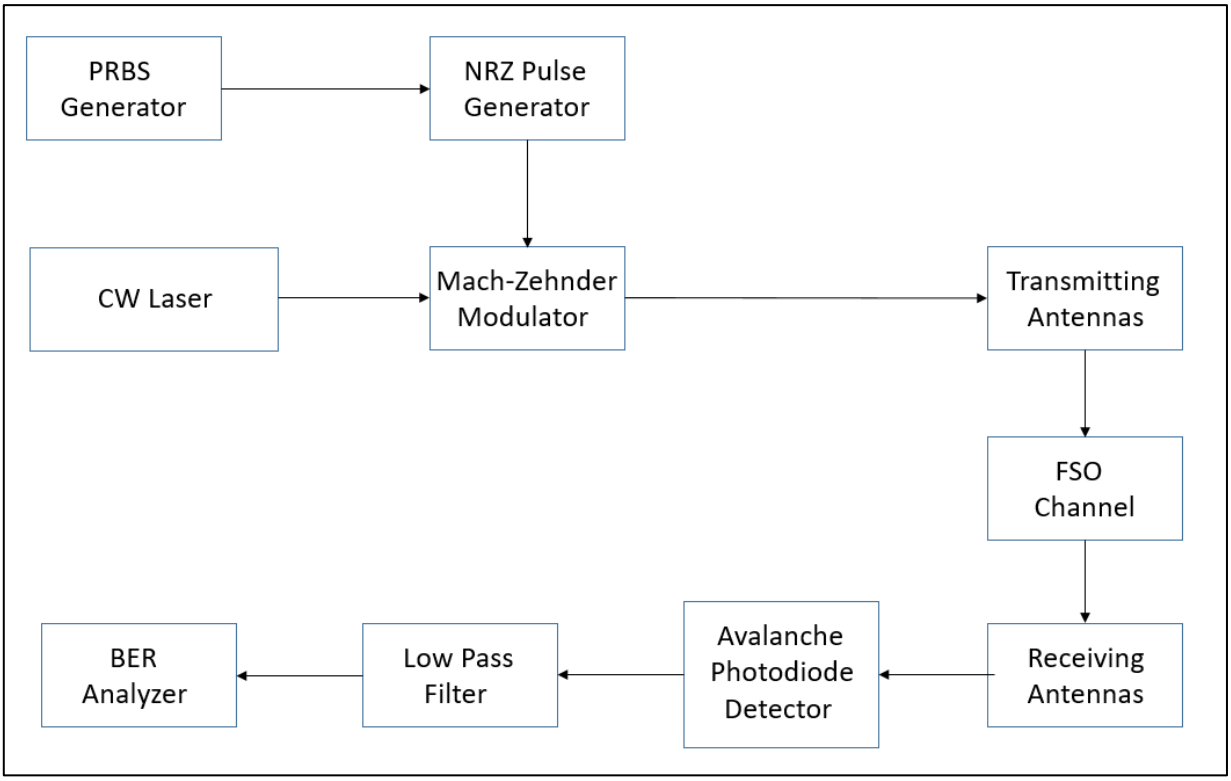

Figure 1: Illustration of a massive MIMO FSO System

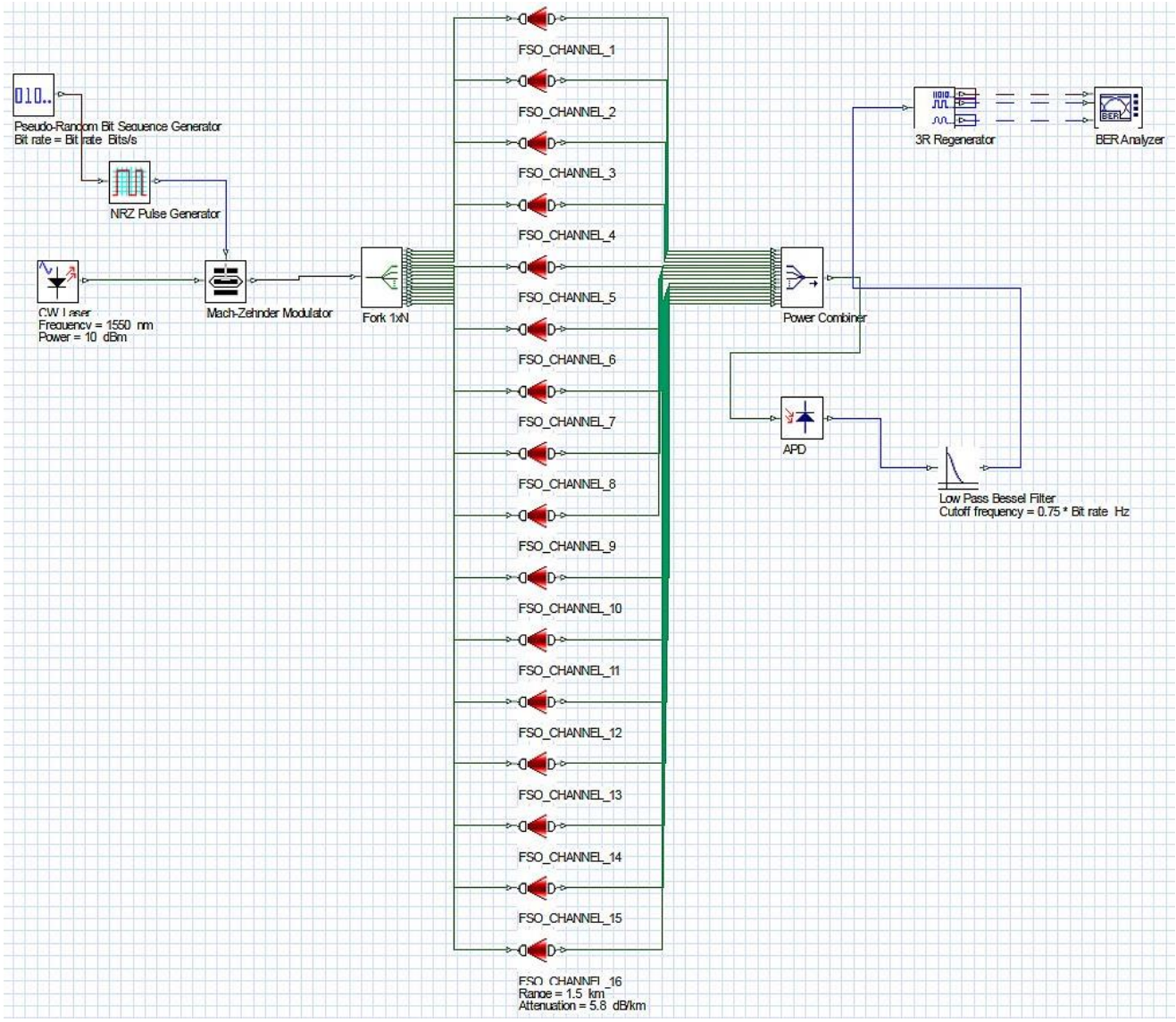

Figure 2: Simulation Layout of 16 × 16 massive MIMO FSO System

5. RESULT ANALYSIS

The proposed system was analyzed in various weather conditions. The diversity order selected for the simulation was 16. A Continuous Wave (CW) Laser is used as the optical source. Four different weather conditions have been used in simulation. These are clear weather, haze, moderate rain and heavy rain. The 16 FSO channels have been implemented with equal attenuation values in each weather condition for this simulation.

The performance of the 16 × 16 FSO system is analyzed at a 10 Gbps transmission rate at first. From the min. Log of BER vs Source Power graph in Figure 3, it is observed that the model yields very good results at this data rate. In case of heavy rain, at 1 km distance, the min. log of BER obtained is 3.19×10^{-119} by applying 0 dBm source power. In case of heavy rain, a BER of 3.19×10^{-119} is obtained at 1 km distance by applying a source power of 0 dBm.

The min. log of BER vs source power graph at 10 Gbps transmission rate in different weather conditions for 2 km distance is shown in Figure 4. The BER at 2 km distance is observed to increase noticeably. It is 3.14×10^{-14} in case of heavy rain by applying a source power of 10 dBm.

The results from Figure 1 and Figure 2 show that the performance of the 16×16 system under all weather conditions at 10 Gbps is quite satisfactory. Hence, it is possible to achieve higher data rate with this system for a significant transmission range. So, further analysis was conducted to obtain optimum parameters of the proposed massive MIMO FSO system.

For this purpose, simulation was conducted to obtain the highest data rate for an optimum distance for a 16×16 system by considering a constant bit error rate (BER) of $10 - 10$. The graphical results can be seen in Figure 5. From the graph, a data rate of 40 Gbps was taken to be optimum. It was observed that under clear weather the optimum distance was found to be much higher compared to other weather conditions. For clear weather the maximum distance was 8.2 km for the optimum data rate of 40 Gbps. The similar analysis was also done for 8 × 8 system. In this case, the distance was 6.32 km for clear weather.

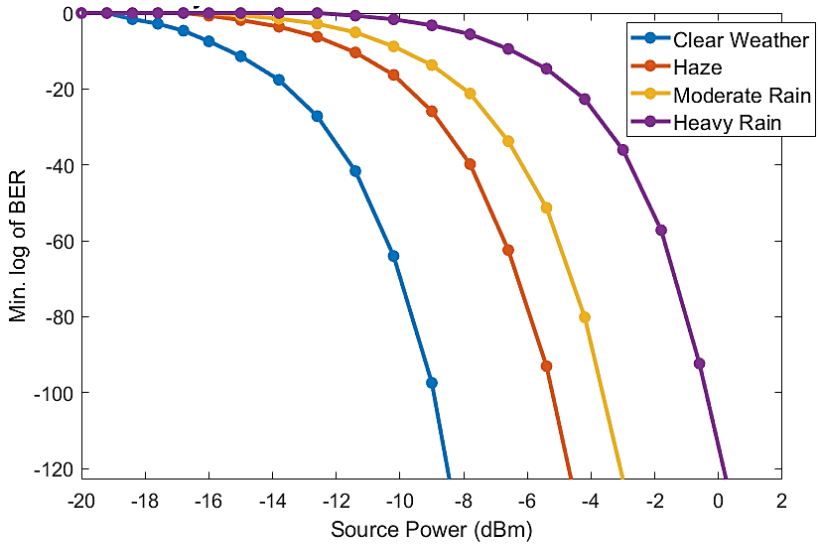

Figure 3: Min. log of Bit Error Rate vs. Source Power (dBm) graph for 16 × 16 system at 1 km in different weather conditions

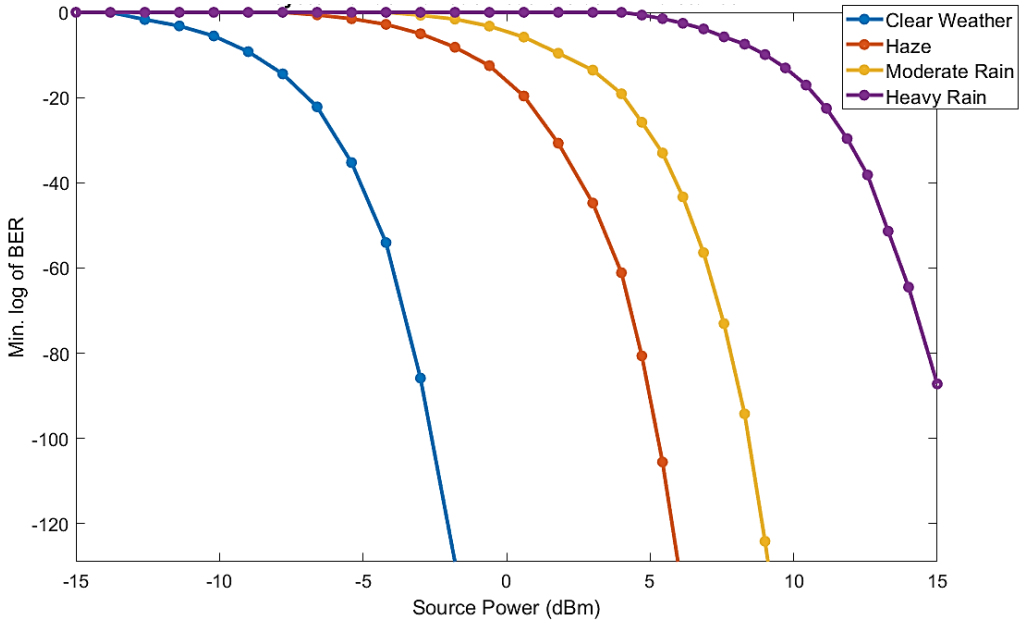

Figure 4: Min. log of Bit Error Rate vs. Source Power (dBm) graph for 16 × 16 massive MIMO FSO system at a distance of 2 km in different weather conditions

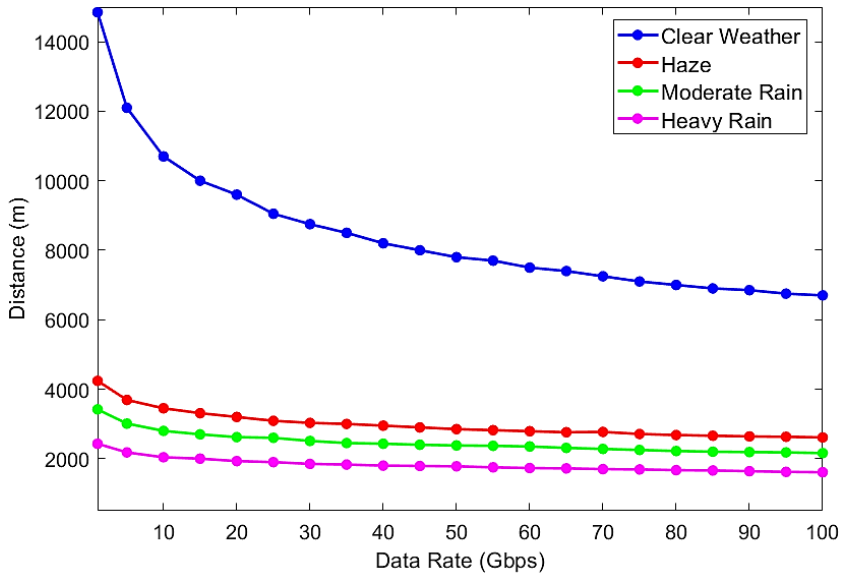

Figure 5: Distance vs data rate graph of 16 × 16 massive MIMO FSO system for a BER of $10e^{-10}$

When turbulent weather conditions were considered, the transmission range reduced significantly. However, the distance was still significant for these weather conditions. The distance was found to be 2.97 km in haze for 16×16 system, whereas it was 2.53 km for 8×8 system. In case of 8×8 system, in moderate rain and heavy rain, the transmission ranges obtained were 2.11 km and 1.6 km, which increased to 2.43 km and 1.79 km for 16×16 system. Thus, for turbulent weather conditions, the transmission range of the 16×16 system gets increased by about $200 - 300$ m on average compared to that of the 8×8 system.

Here, the simulation is carried out at a constant source power of 10 dBm. The optimum system parameters obtained from above analysis are listed in Table 3. The performance analysis of the 16×16 system with these optimum parameters is done with power penalty and receiver sensitivity plots. The plots are compared with that of 8×8 system for same simulation parameters.

Table 3
Optimum System Parameters

Attenuation (dB/km^{-1})	Weather	BER	Data Rate (Gbps)	Optimum Distance (16×16 Massive MIMO FSO System) (km)	Optimum Distance (8×8 Massive MIMO FSO System) (km)
0.43	Clear Weather	10^{-10}	40	8.2	6.32
4.2	Haze			2.97	2.53
5.8	Moderate Rain			2.43	2.11
9.2	Heavy Rain			1.79	1.6

Figure 6 shows the power penalty plot of 8×8 MIMO system in 4 different weather conditions. The values used in this plot are for a distance of 1.79 km and at the optimum data rate of 40 Gbps. From the power penalty plot of 8×8 massive MIMO FSO system we see that, to attain a BER of 10^{-10}, source power of -3.5 dBm is needed for clear weather. For heavy rain, the power requirement becomes 13 dBm.

From the power penalty plot of 16×16 FSO system shown in Figure7, it can be observed that for clear weather the source power needed to obtain a BER of 10^{-10} is -6.5 dBm. For haze it is around 0 dBm and for heavy rain the required source power is 10 dBm. Hence we can see that in case of same weather the power requirement reduces by 3 dBm if the antenna number is doubled. That is, when antenna number is doubled, the requirement of source power becomes half. Now, the analysis is done with received power vs. distance plots. Figure 8 shows the received power vs distance curve for 8×8 MIMO FSO system. From the curve it is seen that the optimum distance for each of 4 weather conditions is obtained when the received power is -25 dBm. As the distance increased, the received power decreased. That is, the performance will degrade for larger distance. From the received power vs. distance curve for 16×16 FSO system shown in Figure 9, it is visible that when the received power is -22 dBm, the optimum distance is obtained for all 4 weather conditions considered here. It is observed that, if the antenna number is doubled, the system will yield similar performance even if the received power becomes half.

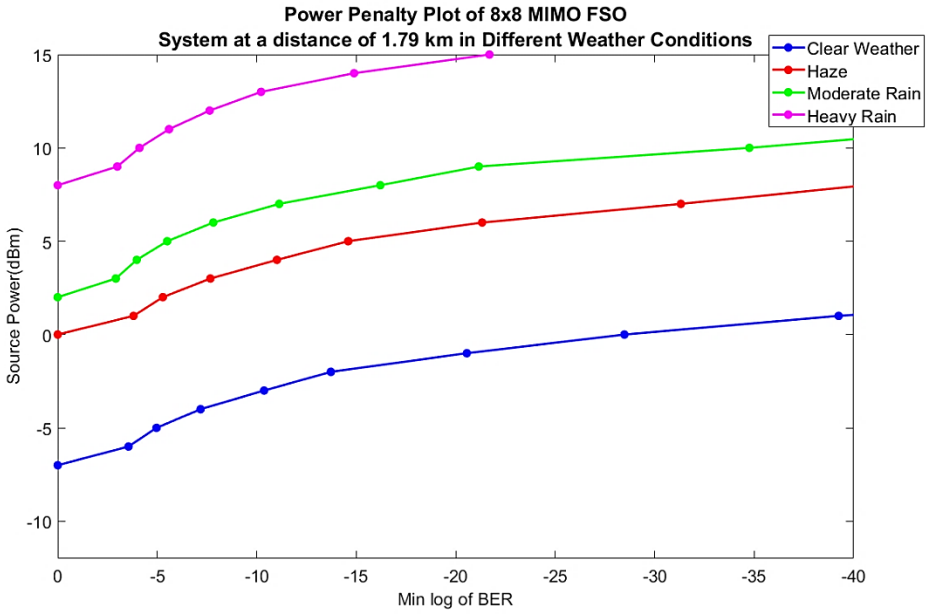

Figure 6: Power penalty plot of $\mathbf{8 \times 8}$ massive MIMO FSO system in different weather conditions at a distance of $\mathbf{1.79}$ km.

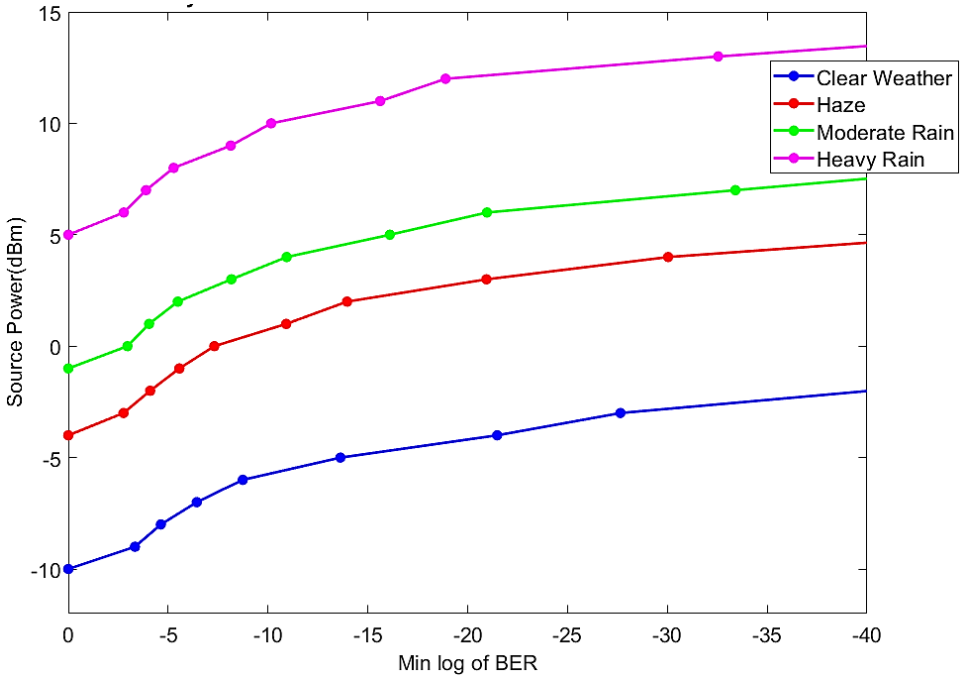

Figure 7: Power penalty plot of $\mathbf{16 \times 16}$ massive MIMO FSO system in different weather conditions at a distance of $\mathbf{1.79}$ km.

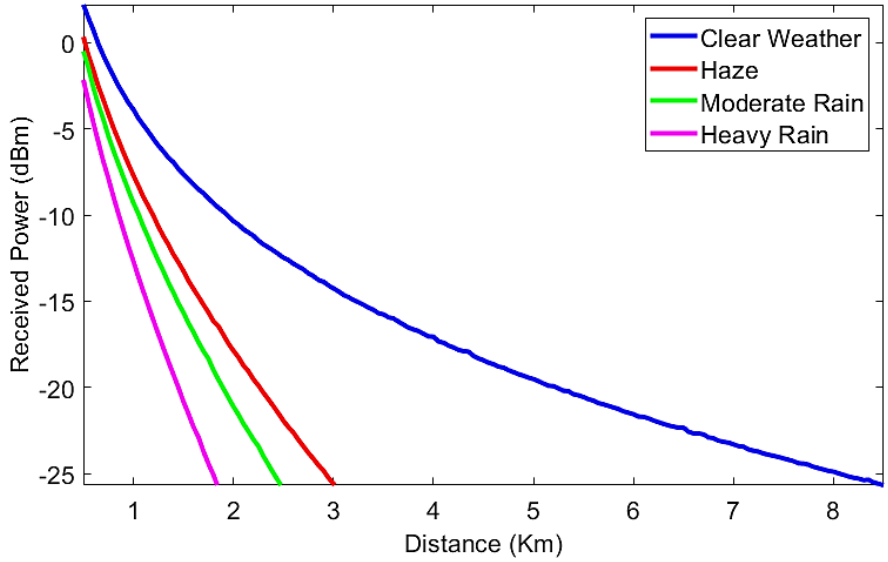

Figure 8: Received power vs distance curve for $\mathbf{8 \times 8}$ MIMO FSO system

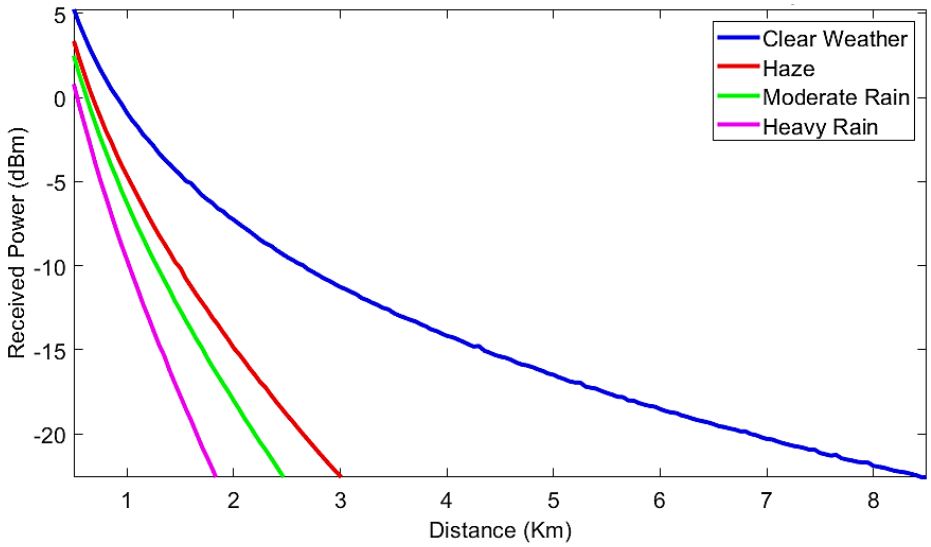

Figure 9: Received power vs distance curve for $\mathbf{16 \times 16}$ massive MIMO FSO system

Now, the presence of noise in the system is analyzed by observing the eye diagram. For 8×8 MIMO system, the performance is poor at a distance of 1.79 km in heavy rain. From the eye diagram in Figure 10, the min BER is seen to be 7.9×10^{-5}. However, the performance significantly improves for 16×16 system. The performance improves for the 16×16 system as it has more redundant paths than that of the 8×8 system. Signal can move through these multiple redundant paths during inclement weather and thus the probability of error in the transmitted bits is reduced.

Figure 11 shows the eye diagram of 16×16 FSO system. From the eye diagram of the 16×16 system the min BER is found to be $1 \times 10 - 11$. The quality factor also becomes double in 16×16 system compared to that of 8×8 system.

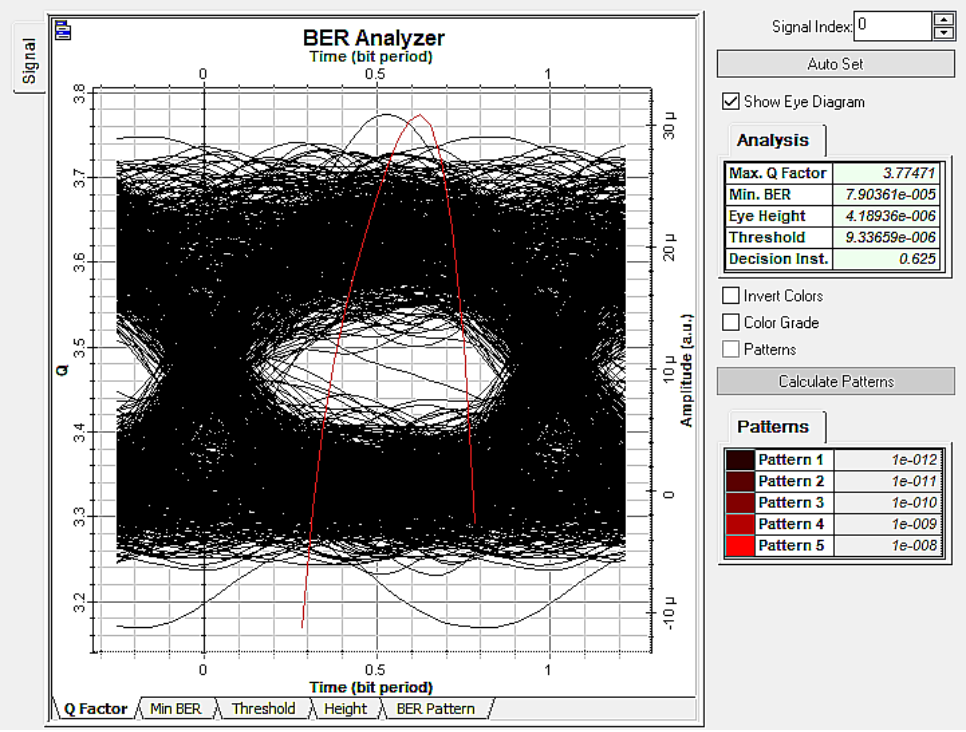

Figure 10: Eye Diagram of 8×8 MIMO FSO system in heavy rain at a distance of 1.79 km

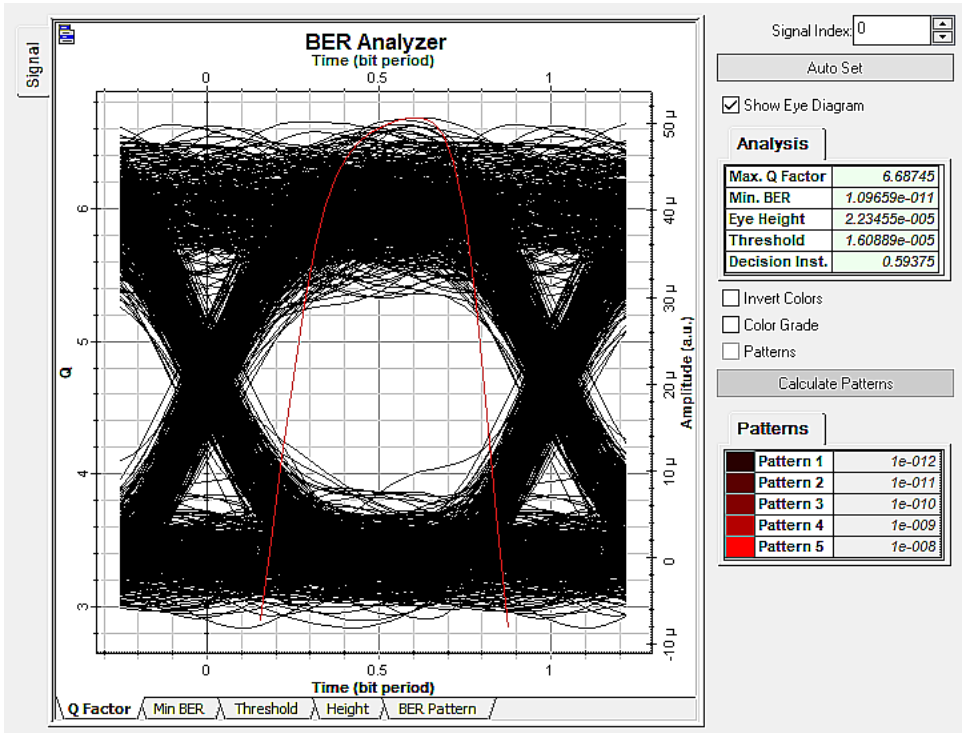

Figure 11: Eye Diagram of 16×16 massive MIMO FSO system in heavy rain at a distance of 1.79 km

6. CONCLUSIONS

In this work, the performance of a massive MIMO FSO system in various turbulent weather conditions is analysed and the optimum parameters in these conditions are obtained. The optimum transmission rate for the system is found to be 40 Gbps. The simulation is done with a $16x16$ array of antennas. More number of antennas could have been used which could give better results. However, the antenna number is selected to be 16 for both transmitter and receiver by considering cost-efficiency. In this proposed system, the Gamma- Gamma distribution model is used to characterize the atmospheric turbulence.

The performance of the system was analyzed in terms of BER, quality factor, source power, and receiver sensitivity. The performance has been graphically shown by power penalty and receiver sensitivity plots. In case of haze, a date rate of 40 Gbps is obtained with 16×16 antennas at a min BER of 10^{-10} for a transmission range of 2.97 km. For 8×8 it has been reduced to 2.53 km.

In case of moderate rain and heavy rain, similar performance is obtained at a transmission range of 2.43 km and 1.79 km, whereas the range is found to be 2.11 km and 1.6 km for 8×8 array of antennas. The proposed 16×16 system gives a satisfactory performance in turbulent weather conditions. It can serve the purpose of achieving a good transmission range at a higher data rate by overcoming the hindrance of atmospheric turbulence quite well. A noteworthy observation from the power penalty graph is that to maintain a constant BER, the source power requirement reduces to half when the number of antennas is made twice.

The receiver sensitivity also gets enhanced for the 16×16 system. In heavy rain, the receiver sensitivity is around 1 dBm for 16×16 system, while it is 2.5 dBm for 8×8 system. Another important point is that the source in this model is used in the infrared region. The performance might be enhanced by using a visible light source as the frequency range is higher in this case. However, due to issues related to health safety, it is permitted to use very low source power (up to 1 mW only) when visible light source is employed.

With such low source power, it is not possible to transmit data up to a considerable distance. So, further research is needed to devise a massive MIMO FSO system using a visible light source that may provide significant transmission performance. In addition to this, different modulation schemes and higher order modulation techniques might be employed to design a more robust massive MIMO FSO system.

ACKNOWLEDGEMENTS

Authors would like to express their gratitude to the Ministry of Education (MOE), Bangladesh; Ministry of Defence (MOD), Bangladesh; Department of Electrical Electronic and Communication Engineering, Military Institute of Science and Technology (MIST), Dhaka, Bangladesh. They also would like to thank the Editors and anonymous reviewers of MIJST for the insightful suggestions and comments to improve the contents of the manuscript.

REFERENCES

Albreem, M. A., Juntti, M., & Shahabuddin, S. (2019). Massive MIMO detection techniques: A survey. *IEEE Communications Surveys & Tutorials*, 21(4), 3109-3132. DOI: 10.1109/comst.2019.2935810

Anandkumar, D., & Sangeetha, R. G. (2020). A survey on performance enhancement in free space optical communication system through channel models and modulation techniques. *Optical and Quantum Electronics*, 53(1). DOI: 10.1007/s11082-020-02629-6

Badar, N., & Jha, R. K. (2017). Performance comparison of various modulation schemes over free space optical (FSO) link employing Gamma–Gamma fading model. *Optical and Quantum Electronics*, 49(5). DOI: 10.1007/s11082-017-1025-4

Naboulsi, M. A., Sizun, H., & Fornel, F.D. (2004). Fog attenuation prediction for optical and infrared waves. *Optical Engineering*, 43, 319-329.

Bhatnagar, M. R., & Ghassemlooy, Z. (2015, June). Performance evaluation of FSO MIMO links in Gamma-Gamma fading with pointing errors. In *2015 IEEE International Conference on Communications (ICC)*. (pp. 5084-5090).

Chatti, I., Baklouti, F., Chekir, F., & Attia, R. (2019). Comparative analysis of MIMO-based FSO and MIMO-based MGDM communications. *Optical Review*, 26(6), 631-643. DOI: 10.1007/s10043-019-00537-z

Chauhan, A., Kumari, A., Meena, P., & Meena, S. K. (2021, June). Performance Analysis of Optical Communication System for Various Filtering Operations Using MIMO FSO System under Fog Condition. In *2021 International Conference on Intelligent Technologies (CONIT)*. (pp. 1-5).

Dubey, A., & Singh, H. (2020, July). Performance Analysis of MIMO-FSO communication link with Hybrid Modulation. In *2020 7th International Conference on Smart Structures and Systems (ICSSS)*. (pp. 1-6).

El-Mashade, M., Aly, M., & Toeima, A. (2015). Performance evaluation of FSO system with MIMO technique in different operating environments. *Physical Science International Journal*, 7(1), 33-48. DOI:10.9734/PSIJ/2015/17212

Israr, A., Israr, A., Khan, F., & Khan, F. (2019). Optimal modulation technique for MIMO FSO link. *Wireless Personal Communications*, 109(2), 695-714. DOI:10.1007/s11277-019-06586-6

Jarangal, E., & Dhawan, D. (2018). Comparison of channel models based on Atmospheric turbulences of FSO system-A Review. *International Journal of Research in Electronics and Computer Engineering*, 6(1), 282-286.

Khwandah, S. A., Cosmas, J. P., Lazaridis, P. I., Zaharis, Z. D., & Chochliouros, I. P. (2021). Massive MIMO Systems for 5G Communications. *Wireless Personal Communications*, 1-15. DOI: 10.1007/s11277-021-08550-9

Kumar, N., & Khandelwal, V. (2019, March). Simulation of MIMO-FSO System with Gamma-Gamma Fading under Different Atmospheric Turbulence Conditions. In *2019 International Conference on Signal Processing and Communication (ICSC)*. (pp. 117-124).

Lu, L., Li, G. Y., Swindlehurst, A. L., Ashikhmin, A., & Zhang, R. (2014). An overview of massive MIMO: Benefits and challenges. *IEEE Journal of Selected Topics in Signal Processing*, 8(5), 742-758. DOI: 10.1109/jstsp.2014.2317671

Mansour, A., Mesleh, R., & Abaza, M. (2017). New challenges in wireless and free space optical communications. *Optics and Lasers in Engineering*, 89, 95-108. DOI: 10.1016/j.optlaseng.2016.03.027

Sangeetha, A., Sharma, N., & Deb, I. (2019). Feasibility evaluation of MIMO based FSO links. *Journal of Communications*, 14(3), 187-193. DOI: 10.12720/jcm.14.3.187-193

Thandapani, K., Gopalswamy, M., Jagarlamudi, S., & Sriram, N. B. (2021). Performance analysis of WDM free space optics transmission system using MIMO technique under various atmospheric conditions. *Journal of Optical Communications*. DOI:10.1515/joc-2021-0038

Tsai, C., Wong, K., & Li, W. (2018). Experimental results of the multi-Gbps smartphone with 20 multi-input multi-output (MIMO) antennas in the 20x12 MIMO operation. *Microwave and Optical Technology Letters*, 60(8), 2001-2010. DOI:10.1002/mop.31289

Zhang, Y., Wang, P., Guo, L., Wang, W., & Tian, H. (2017). Performance analysis of an OAM multiplexing-based MIMO FSO system over atmospheric turbulence using space-time coding with channel estimation. *Optics express*, 25(17), 19995-20011.

CALL FOR PAPERS

MIJST invites to submit Unpublished, Original, and Innovative research works from any branch of Engineering, applied sciences, and related areas.

Submitted manuscripts will undergo a double-blind peer-review process. For submission of Manuscript template and authors' instructions, please visit journal website at:
https://mijst.mist.ac.bd/mijst/index.php/mijst/

MIJST offers a faster peer-review process. There will be no charges for Registration, Online submission, Publication of manuscripts, and access to the published articles. Best selected papers will also be awarded by MIJST.

ABOUT MIJST

MIST International Journal of Science and Technology (MIJST), published biannually (June and December), is a peer-reviewed open-access journal of the Military Institute of Science and Technology (MIST). This journal is a continuation of the 'MIST Journal of Science and Technology', published by MIST, under ISSN 1999-2009 from 2009 to 2011, ISSN 2224-2007 from 2012 to 2019, & E-ISSN 2707-7365 since 2020.

MIJST publishes original research findings as regular papers, review papers (by invitation). The Journal provides a platform for Engineers, Researchers, Academicians, and Practitioners who are highly motivated in contributing to the Engineering, Science, and Technology and Applied Sciences disciplines. MIJST welcomes contributions that address solutions to the specific challenges of the developing world.

The Journal is now indexed in the "DOI Crossref", "ISSN Portal", "BaglaJOL", "Creative Common", "Microsoft Academic Search", "Publons", "Semantic Scholar", "ScienceGate", "Scilit", "EuroPub" and "Open Journal System" databases and is accessible through the Google Scholar. The journal is also planned to be registered under the Asian Citation Indexing, Directory of Open Access Journals (DOAJ), SCOPUS, and Emerging Source Citation Indexing (ESCI) in course of time. The Journal aims to be one of the leading journals of the Country and the Region for its contributions in the advancement of Science and Technology. Unpublished innovative world-class research papers under the following subject areas are invited. Contributions from other areas of Engineering and Applied Sciences are also welcome.

SUBJECT AREAS:

- **AEROSPACE AND AVIONICS ENGINEERING**
- **APPLIED PHYSICS & SCIENCE**
- **ARCHITECTURE**
- **BIOMEDICAL ENGINEERING**
- **CHEMISTRY**
- **CIVIL ENGINEERING**
- **COMPUTER SCIENCE AND ENGINEERING**
- **ELECTRICAL, ELECTRONIC AND COMMUNICATION ENGINEERING**
- **ENVIRONMENTAL, WATER RESOURCES, AND COASTAL ENGINEERING**
- **INDUSTRIAL AND PRODUCTION ENGINEERING**
- **MATERIALS SCIENCE & ENGINEERING**
- **MECHANICAL ENGINEERING**
- **NAVAL ARCHITECTURE AND MARINE ENGINEERING**
- **NUCLEAR SCIENCE & ENGINEERING**
- **PETROLEUM AND MINING ENGINEERING**

E-ISSN: 2707-7365

Journal URL